

OPTIMIZED AND USER-FRIENDLY WORKFLOW FOR THE
FABRICATION OF 3D PRINTED MAXILLARY HOLLOW CLOSED
SURFACE MODEL OBTURATOR USING CT, INTRAORAL
SCANNING TECHNOLOGY, AND COMPUTER
AIDED/MANUFACTURING

Master Thesis

Anna Ooms

Head and neck oncology surgery
Netherlands Cancer Institute

Graduation Committee:

Dr. F. Siepel

Dr. M.B. Karakullukçu

Dr. L.H.E. Karssemakers

M. Krap

Dr. M.J.A. van Alphen

Drs. A.G. Lovink

Dr. ir. L. Alic

University of Twente

The Netherlands

October 2022

Graduation Committee

Technical supervisor (Chairman)

Dr. F. Siepel

Assistant Professor - Technical Physician
Robotics and Mechatronics group
Faculty of EEMCS
University of Twente
Enschede, The Netherlands

Medical supervisors

Dr. M. B. Karakullukçu

Head and Neck Surgeon
Department of Head and Neck Surgery &
Oncology
Verweilius 3D Lab
Netherlands Cancer Institute
Amsterdam, The Netherlands

Dr. L. H. E Karssemakers

Head and Neck Surgeon
Department of Head and Neck Surgery &
Oncology
Netherlands Cancer Institute
Amsterdam, The Netherlands

Dr. M. Krap

Maxillofacial prosthodontist
Department of Head and Neck Surgery &
Oncology
Netherlands Cancer Institute
Amsterdam, The Netherlands

Technical supervisor

Dr. M.J.A. van Alphen

Postdoctoral researcher - Technical Physician
Department of Head and Neck Surgery &
Oncology
Verweilius 3D lab
Netherlands Cancer Institute
Amsterdam, The Netherlands

Process supervisor

Drs. A.G. Lovink

Faculty Science and Technology
University of Twente
Enschede, The Netherlands

External member

Dr. ir. L. Alic

Faculty Science and Technology
University of Twente
Enschede, The Netherlands

Preface

This thesis is part of my graduation for the Master's study: 'Technical Medicine: Medical Imaging and Interventions'. This finished thesis marks the end of my period at the University of Twente.

I would like to express my sincere appreciation to my committee for their guidance, feedback, support, and enjoyment during my graduation year. You all kept me excited and motivated during this research and clinical journey. In addition, you helped me to improve myself on an academic and professional level.

Furthermore, I would like to thank Cees Kleverlaan and João Tribst for all the help and support for the experiments at the Academic Center for Dentistry Amsterdam. I am also grateful to my fellow students at the 3D lab for helping me during the pleasant research meetings and daily discussions. Finally, I would like to thank my family and friends for their motivation and belief during the process.

Abstract

An oronasal defect created by the surgical resection of the palate and maxilla can be directly obturated by a hand-kneaded maxillofacial prosthesis, the so-called immediate surgical obturator (ISO). The ISO consists of a transparent baseplate and silicon putty obturator. The obturator replaces hard and soft tissue, thereby improving deglutition and mastication, speech enhancement, avoiding contamination, and improving the overall quality of life [1], [2]. Besides the advantages of the maxillary prosthesis, the ISOs are, on the other hand, large, high-weighted, and unstable, especially in large defects. The hand-kneaded silicone putty obturator is also porous and susceptible to fluid and bacterial uptake, which further increases the weight, and results in a foul smell [3]. These disadvantages often reduce the patient's function and comfort. Creating a hollow maxillary obturator could reduce the weight of the prosthesis by 7 – 33 %, depending on the size of the defect [4]. Computer-aided design and manufactured (CAD/CAM) designed obturators may overcome the limitations of the conventional method. This thesis aimed to investigate the shape, volume, clinical fit, weight reduction, and material properties of a novel designed CAD/CAM prosthesis, the so-called closed surface model (CSM) obturator.

In this study, CT and intraoral scanning technology were used for the image acquisition of the novel CAD/CAM ISOs. An existing CAD/CAM workflow was optimized and used to design and print different scaled CSM obturators around the segmented bone and soft tissue, in Clear resin. The clinical fit of the prostheses was evaluated in a clinical trial study with four included maxillectomy patients in the Netherlands Cancer Institute—Antoni van Leeuwenhoek Hospital (NKI-AVL). In addition, the CSM obturators were evaluated with a retrospective study of maxillectomy patients from 2010 to 2020 in the NKI-AVL (n = 17). The criteria included patients with a pre-and postoperative CT scan, in which the conventional obturator could be segmented from the postoperative scan based on greyscale thresholding. The skulls of both scans were also segmented and registered to obtain the resection margins, which were classified according to the novel Ooms' classification system. The CSM obturators were then designed according to this classification system and compared with the conventional and theoretical reference obturators by weight reduction and Hausdorff Distances (HD). Furthermore, this study investigated whether the material of the CAD/CAM ISOs was stable in a simulated oral cavity environment of 37°C heated water. In addition, the fracture mechanic performance during the removal of the prosthesis in the patient's mouth was researched by a compressive resistance test. The outcome of the maximal fracture load was used for a digital Finite Element Analysis to study the tensile stress and deformation in Ansys.

Our clinical results showed that the shape and volume of the conventional obturator depend on the height of the resection and whether the canine was resected. This resulted in different CSM design choices per Ooms' class. The 0.8 scaled CSM around segmented resection margins showed the overall best clinical fit with a clinical weight reduction between 36 – 39%. In the retrospective study, the average weight reduction of the CSM obturator was about 47%, which was similar to the theoretical clinical reference. In the material property study, the prosthesis had a water absorption of 2%, and material deformation occurred at the thinnest, lateral side of the baseplate. The fracture load during the prosthesis removal was 25 N which indicated that the prosthesis was safe for usage.

Future studies should focus on the improvement of the final workflow and prosthesis design to enable the clinical implementation of the CAD/CAM obturators. The improvements should include a more automated workflow, integrated into a user interface, and adjustments in the baseplate design to gain retention to the remaining bone structures and teeth. Furthermore, the finalized designs should be evaluated within a large cohort clinical-trial study, comparing the conventional obturator with the novel CSM obturators. The clinical-trial findings will gain insight into the impact of the amount of weight reduction on the patient's comfort improvement.

Contents

1. General introduction.....	10
1.1 Clinical background	10
1.1.1 Anatomy maxillae	10
1.1.2 Musculature.....	11
1.1.3 Blood supply & innervation.....	11
1.1.4 Epidemiology	12
1.1.5 Maxillectomy approaches.....	12
1.1.6 Maxillectomy classifications.....	13
1.1.7 Reconstruction of the maxillary defect.....	14
1.2 Problem statement.....	16
1.2.1 Conventional obturators.....	16
1.2.2 Concept CAD/CAM workflow.....	16
1.3 Objectives.....	17
1.4 Thesis outline	18
1.5 Technical background.....	18
1.5.1 CAD/CAM obturators	18
2. Clinical evaluation of the CSM obturator	22
2.1 Introduction	22
2.1.1 Previous work: the hollow bulb obturator.....	22
2.1.2 Hollow closed surface model	23
2.1.3 Study aim	24
2.2 Method.....	24
2.2.1. Patients.....	24
2.2.2 CT analyses	25
2.2.3 Pre-operative virtual surgical planning.....	25
2.2.4 Baseplate design & merge	27
2.2.5 3D printing and final polishing.....	28
2.2.6 Patient-specific obturator design.....	28
2.2.7 Navigation	30
2.2.8 Post-operative analysis.....	31
2.3 Results	33
2.3.1 Patients.....	33
2.3.2 Registration error	33
2.3.3 Clinical evaluation.....	34
2.3.4 Post-operative analysis.....	38

2.3.5 Weight reductions	39
2.4 Discussion	40
2.4.1. Interpretation of results.....	40
2.4.2 Strength and weaknesses	41
2.4.3. Future recommendations.....	42
2.5 Conclusion	42
3. Retrospective study: verification of the CSM obturator	44
3.1. Introduction.....	44
3.1.1. Horizontal components.....	44
3.1.2. Vertical components.....	46
3.1.3. Classification system	47
3.1.4. Study aim.....	48
3.2. Methods	49
3.2.1. Patients.....	49
3.2.2. CT analyses	49
3.2.3. Technical analysis.....	49
3.2.4. Statistical methods.....	52
3.3. Results	53
3.3.1 Patients.....	53
3.3.2 Weight reduction	53
3.3.3 Shape & volume comparison	58
3.4 Discussion.....	61
3.4.1 Interpretation of results	61
3.4.2 Strength and weaknesses	62
3.4.3 Future recommendations.....	63
3.5 Conclusion	63
4. Material properties of the CSM obturator.....	66
4.1 Introduction	66
4.1.1 Study aim.....	66
4.2 Methods	67
4.2.1 Pre-processing	67
4.2.2 Compressive resistance test.....	68
4.2.3 Digital analysis	68
4.2.4 Finite element analysis.....	68
4.3 Results	70
4.3.1 Compressive resistance test.....	70
4.3.2 Material stability analysis	70
4.4.3 Stress assessment.....	71

4.4 Discussion	73
4.4.1 Interpretations of results.....	73
4.4.2 Strength and weaknesses	74
4.4.3 Future recommendations	74
4.5 Conclusion.....	75
References	77
Appendix	84
A1: Protocol segmentation steps in Slicer	84
A2: Protocol Metronics navigation preparation steps in Slicer	91
B1: Python scripted resection segmentation steps in Slicer	93
B2: Python scripted Metronics navigation steps for 3D Slicer.....	99
C: Protocol baseplate design in Autodesk Meshmixer.....	101
D: Final designs in Autodesk Meshmixer	102
E: Conventional surgical obturators, classified by the Ooms' classification system.....	104
F: Closed surface model obturators based on the Ooms' obturator classification system	105
G: Direct comparison results of the weight reduction, volumes, and Hausdorff Distances	107
H1: Distance maps Bone-CSM designs	109
H2: Distance maps bone & soft tissue CSM	111

List of Figures

Figure 1.1. Anatomy of the maxillae bone.....	10
Figure 1.2. Anatomy of the four paired paranasal sinuses.....	11
Figure 1.3. Schematic overview of the maxillary blood supply and nerve innervation..	11
Figure 1.4. Schematic overview of surgical approaches for a maxillectomy.....	12
Figure 1.5. Brown's classifications for maxillary defects.....	13
Figure 1.6. Two examples of the immediate surgical obturator, three weeks post-surgery.....	15
Figure 1.7. Schematical illustration of circumzygomatic wiring.	15
Figure 1.8. Definitive obturator prosthesis.	16
Figure 1.9. Hollow bulb immediate surgical obturator design.....	17
Figure 1.10. The 3Shape TRIOS intraoral scanner.	18
Figure 1.11. Schematically illustrated differences between the conventional solid putty obturator and the hollow computed-aided and manufactured (CAD/CAM) obturator.....	19
Figure 2.1. Workflow of the computer-aided and manufactured designed hollow bulb immediate surgical obturator in MATLAB.....	21
Figure 2.2. Design steps of the closed surface model (CSM) obturator from segmented maxillary resection margins in the open open-source software application 3D Slicer using the 'Marksup to model' extension.	22
Figure 2.3. Intraoral scan of the upper jaw with segmented CT tissues in the open-source software application 3D Slicer.....	23
Figure 2.4. Segmented skulls of each included patient (P) in 3D Slicer.	24
Figure 2.6. Registration of a segmented CT skull and intraoral scan (IOS) of the upper jaw.	25
Figure 2.5. Schematical overview of the NKI-AVL in-house workflow for fabricating a 3D printed baseplate and closed surface model (CSM) obturator.....	25
Figure 2.7. Schematical workflow of the merge and finish of the obturator and baseplate in Autodesk Meshmixer.	26
Figure 2.8. Workflow of the obturator design of patient nr. 1.	27
Figure 2.9. Workflow of two obturator designs of patient nr. 2.....	28
Figure 2.10. Workflow of the obturator design of patient nr. 3.....	28
Figure 2.11. Workflow of the obturator design of patient nr. 4.....	29
Figure 2.12. Example of virtual surgical planned navigation for a partial maxillectomy.....	29
Figure 2.13. Schematical overview of the inner and outer layer calculations of the closed surface model (CSM) obturator.....	31
Figure 2.14. Distance mapping of the registration error of the intraoral scan of the upper jaw and segmented teeth of a CT scan for four patients (P).....	32
Figure 2.15. Image results of the clinical fitting of the digitally designed prostheses in patient nr. 1, directly after partial resection of the maxilla.	33
Figure 2.16. Image results of the clinical fitting of the digitally designed prostheses in patient nr. 2, directly after partial resection of the maxilla.	34
Figure 2.17. Image results of the clinical fitting of the digitally designed prostheses in patient nr. 3, directly after partial resection of the maxilla.	36
Figure 2.18. Image results of the clinical fitting of the digitally designed prostheses in patient nr. 4, directly after partial resection of the maxilla.	37
Figure 2.19. Color-coded distance maps of the obturator of case 1, directly after surgery, and after 7 weeks post-surgery in four directions.....	38
Figure 2.20. Digital closed surface model (CSM) obturators (yellow) with the registered intraoral scanned conventional putty obturator (transparent overlay) per patient (P).	39

Figure 3.1. The four horizontal direction components of the immediate surgical obturator.....	45
Figure 3.2. Comparison of two intraoral scanned immediate surgical obturators.	45
Figure 3.3. MRI slices of the upper jaw (axial view) with highlighted surrounding soft tissue. .	46
Figure 3.4. The maxillary cephalometric landmarks of the Ooms' classification system in anterior view.....	47
Figure 3.5. Ooms' immediate surgical obturator classification system based on the unilateral maxillary defect.....	48
Figure 3.6. Inclusion criteria for maxillectomy patients in the NKI-AVL.....	50
Figure 3.7. Workflow to obtain the segmented conventional obturator and resection margins..	51
Figure 3.8. Schematic overview of the different obturator designs.....	53
Figure 3.9. Schematic overview of the Hausdorff Distance.	54
Figure 3.10. Correlation between the 2mm Clear resin volume scale of the closed surface model (CSM) obturator and weight reduction of one clinical case.....	56
Figure 3.11. Pearson's correlation scatterplots of the segmented conventional obturator volume and absolute weight reduction..	58
Figure 3.12. Pearson's correlation scatterplots of the segmented conventional obturator volume and weight reduction percentage	59
Figure 3.13. Boxplots of the maximum, average, and maximum 95 th percentile Hausdorff Distances (HD) between the unilateral conventional obturator and the closed surface model (CSM) designs.	61
Figure 3.14. Comparison of the volumes of the unilateral conventional obturators per class of the Ooms' classification system.	61
Figure 3.15. Two cases with their closed surface model (CSM) (yellow), designed from the segmented resection bone, and the conventional obturator with a distance mapping overlay.	63
Figure 4.1. Three-dimensional (3D) printed computer-aided and manufactured designed immediate surgical obturators.....	70
Figure 4.2. Experiment tools.....	70
Figure 4.3. Vertical applied load on the fixated obturators using the Instron 6022 machine.....	71
Figure 4.4. Best-fit alignment of the intraoral scanned prosthesis.....	71
Figure 4.5. 3D models in Ansys.....	72
Figure 4.6. Prostheses after the aging simulation and compressive resistance test.	73
Figure 4.7. Material deformity after the aging simulation.....	74
Figure 4.8. Tensile stress generated in the prosthesis.	74
Figure 4.9. Deformation of the prosthesis during incidence of removal force.....	75

List of Tables

Table 1.1. Brown's classification of maxillary defects [25].....	13
Table 2.1. Densities of the denture reline/ resin materials.....	30
Table 2.2. Baseline parameters of included patients.....	32
Table 2.3. Clinical 0.8 scaled obturator fit in patient nr. 2 scored by prosthodontists.....	34
Table 2.4. Clinical 0.7 scaled obturator fit in patient nr. 2, scored by prosthodontists.....	35
Table 2.5 Clinical obturator fit in patient nr. 3 scored by prosthodontists.....	36
Table 2.6 Clinical obturator fit in patient nr. 4 scored by prosthodontists.....	37
Table 2.7 Volume and weight reduction results of each clinical case.....	39
Table 3.1 List of anatomical landmarks in the maxillofacial region.....	46
Table 3.2. Ooms' immediate surgical obturator classification.....	49
Table 3.3. Baseline parameters of included patients.....	55
Table 3.4. Summary of the number of patients per CSM type.....	55
Table 3.5. Summary of the weight reduction results, presenting minimum (min), maximum (max), mean (μ) values, and standard deviations (σ) for n=17.....	56
Table 3.6. Summary of the weight reduction results, presenting minimum (min), maximum (max), mean (μ) values, and standard deviations (σ) for n=15.....	56
Table 3.7. Summary of the obturator volumes and Hausdorff Distances, presenting minimum (min), maximum (max), mean (μ) values, and standard deviation (σ) for n=15.....	60
Table 3.8. Summary of the obturator volumes and Hausdorff Distances, presenting minimum (min), maximum (max), mean (μ) values, and standard deviation (σ) for n=9.....	60
Table 4.1. Weight and fracturing load results of the compressive resistance test.....	73
Table 4.2. Absolute deviations of the material deformities.....	74

Abbreviations

3D	Three-dimensional
ACC	Adenoid cystic carcinoma
CAD/CAM	Computer-aided design and computer-manufacturing
CSM	Closed surface model
CTDI	CT dose index
FEA	Finite element analysis
FPR	Fiducial point registration
HD	Hausdorff Distance
IOS	Intraoral scan
ICP	Iterative closes point
ISO	Immediate surgical obturator
NKI-AVL	Netherlands Cancer Institute—Antoni van Leeuwenhoek
NRRD	Nearly Raw Raster Data
OR	Operation room
RMS	Root mean square
SCC	Squamous cell carcinoma
STL	Stereolithography
TC	Tissue Conditioner
TCR	Theoretical clinical reference
TNM	Tumor, node, and metastases
TMR	Theoretical maximum reference

1. General introduction

This thesis is about fabricating novel 3D printed maxillofacial (upper jaw) prostheses, the so-called immediate surgical obturators. The prosthesis is used to close and maintain the surgical defect between the oral and nasal cavities after a maxillectomy procedure, to improve talking, chewing, and swallowing. Maxillectomy surgery is most commonly required to treat squamous cell carcinomas that problem statement, and thesis outline.

1.1 Clinical background

1.1.1 Anatomy maxillae

The maxillae, the upper jaw, are a pair of symmetrical bones that unite at their midline, the so-called intermaxillary suture [5], [6]. The bones separate the nasal and oral cavities and play a significant role in mastication, communication, and facial appearance [7]. As seen in Figure 1.1, each maxilla bone consists of a body with four processes: the alveolar-, zygomatic-, frontal-, and palatine process. The alveolar process holds up the maxillary dental arch [7]. The palatine process of the maxilla (Figure 1.1b-c), together with the horizontal plates of the palatine bone, form the hard palate, separating the oral cavity from the nasal cavity. The hard palate is connected posteriorly to the soft palate: a mobile structure consisting of muscle fibers and connective tissue covered by a mucous membrane. The soft palate lifts the nasopharynx to demarcate the oropharynx to the nasopharynx [8].

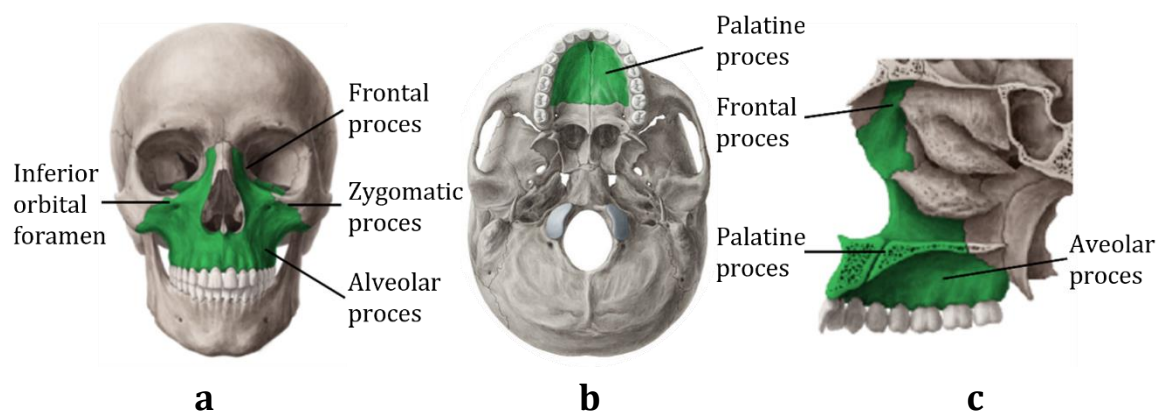


Figure 1.1. Anatomy of the maxillae bone (green). **a)** Anterior view. **b)** Inferior view. **c)** Sagittal view [7].

The maxilla bone consists of a hollow space: the maxillary sinus. The maxillary sinus is one of the four paired paranasal sinuses, each named after the bones that contain them: frontal, maxillary, ethmoid, and sphenoid (see Figure 1.2). The maxillary sinus is shaped like a pyramid and is the largest of the four, producing the nose mucus [9]. The maxillary sinus has its apex towards the zygomatic process and is surrounded by the lateral border of the nose, the alveolar process, and the orbital [10].

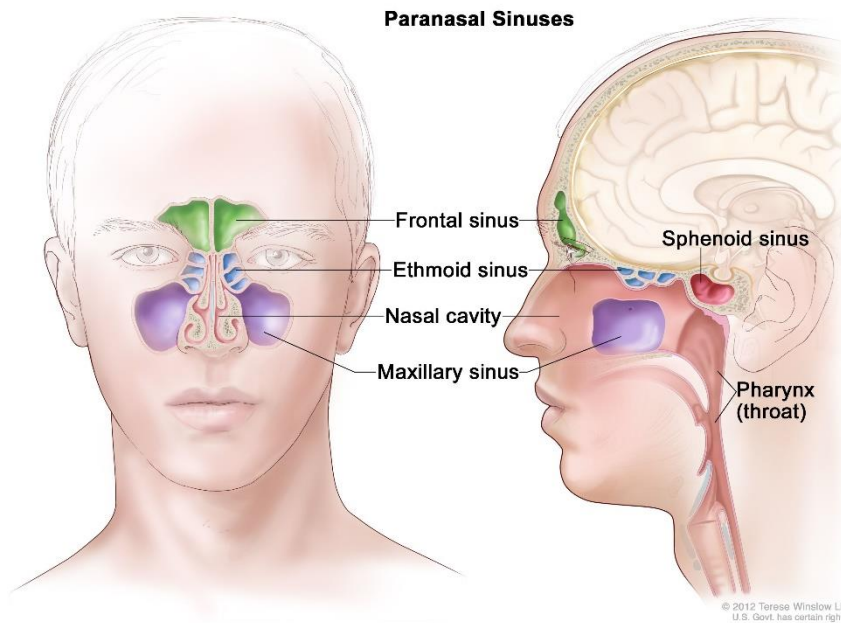


Figure 1.2. Anatomy of the four paired paranasal sinuses [9].

1.1.2 Musculature

The maxillae are surrounded by muscles of mastication and facial expressions. The masseter is the strongest mastication muscle, which derives superficially from the zygomatic process of the maxilla. Several other muscles originate from the maxilla, including the nasalis, levator labii superioris alaeque nasi, levator labii superioris, and levator anguli oris. The orbicularis oris muscle encloses the mouth, in which the intrinsic fibers originate from the alveolar process of the maxilla and mandibular incisors [11], [12].

1.1.3 Blood supply & innervation

The maxillary artery provides most of the blood supply to the maxillae, which derives from the external carotid artery. As seen in Figure 1.3a, the maxillary artery branches into the alveolar- and infraorbital artery, which passes the infraorbital foramen. The additional blood reaches the maxilla through the soft palate, which derives from the facial artery, lingual artery, and the ascending pharyngeal branch of the external carotid artery [11], [13].

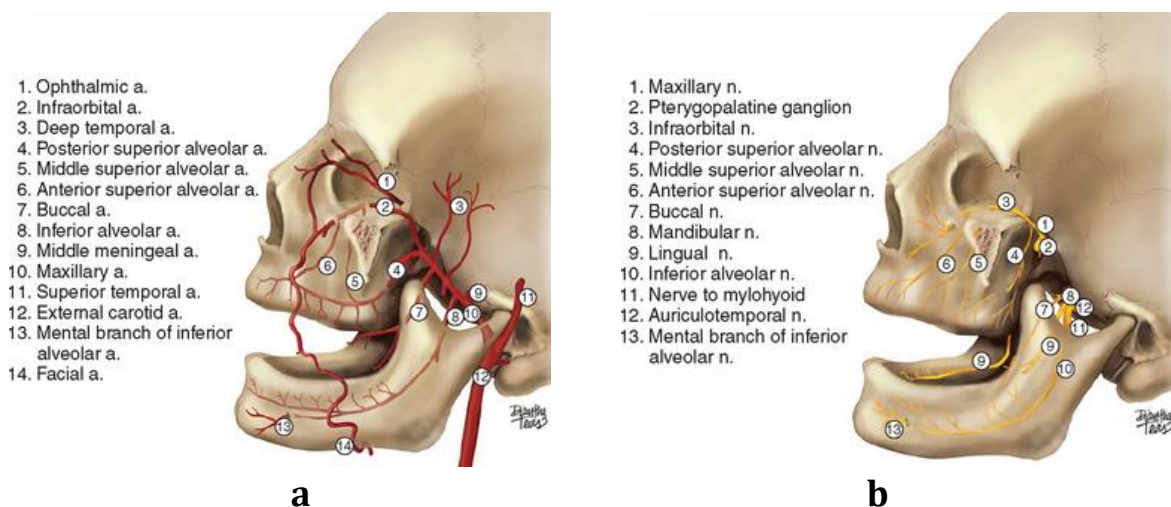


Figure 1.3. Schematic overview of the maxillary blood supply and nerve innervation. a) The maxillary artery and its facial branches derive from the external carotid artery. b) The maxillary nerve derives from one of the three branches of the trigeminal nerve [13].

The maxillae are innervated by the maxillary nerve, as shown in Figure 1.3b. The maxillary nerve derives from one of the three branches of the trigeminal nerve (cranial nerve V) and branches into the infraorbital nerve through the infraorbital foramen. Furthermore, the posterior superior alveolar nerve and the zygomatic branch derive directly from the maxillary nerve [14].

1.1.4 Epidemiology

Cancers of the nasal cavity and paranasal sinuses are rare, with an incidence of <1% of all malignant tumors and including 5% of head and neck cancers. About 90% of head and neck cancers are squamous cell carcinoma (SCC), they develop in the nasal cavity, maxillary sinuses, or the palate. [15]–[17]. Maxillary sinus SCC is a relatively rare and aggressive type of neoplasm and has the highest incidence (60%-70%) compared to the other paranasal sinuses. The disease is often (>80%) discovered late in an advanced stage. Palate SCC has a lower incidence compared to the MSSCCs, they arise from the squamous epithelium of the oral mucosa [18]. Chemicals, viruses, smoking, and alcohol are high-risk factors for this type of tumor, and it mainly affects middle-aged men (55-65 years) from Eastern countries [19], [20].

The most common incidence of SCC is followed by adenoid cystic carcinomas (ACC) which comprise 1% of all malignant neoplasms in the oral cavity and maxillofacial area. The ACC develops in the mucus glands in the maxillary sinuses. Other nasal, paranasal sinuses, and palate tumor types include adenocarcinoma, mucoepidermoid carcinoma, undifferentiated cancer, and occasionally, malignant melanoma [16], [21].

1.1.5 Maxillectomy approaches

The treatment of the maxilla and palate SCC's are based on the tumor size, node, and metastasis (TNM) staging and grading [22]. Except for T1, when there is no bone erosion or destruction, the tumor is usually surgically treated by a maxillectomy, followed by postoperative radiation therapy [23], [24]. A maxillectomy is the removal of all or part of the maxilla bone. The surgical excision is challenging due to the complex anatomy, the surrounding critical structures such as the eyes and cranial nerves, and the advanced stage of the tumor. The tumor often extends to adjacent tissue, such as the (soft) palate, midface, and orbits which will be further described in the following section [19], [25], [26].

There are several approaches for a maxillectomy (see Figure 1.4), depending on the size, type, aggressiveness, and localization of the tumor:

- **Lateral rhinotomy:** an incision lateral to the nose for a medial maxillectomy without extension to the palate or orbit as seen by the red dotted line of Figure 1.4 a.

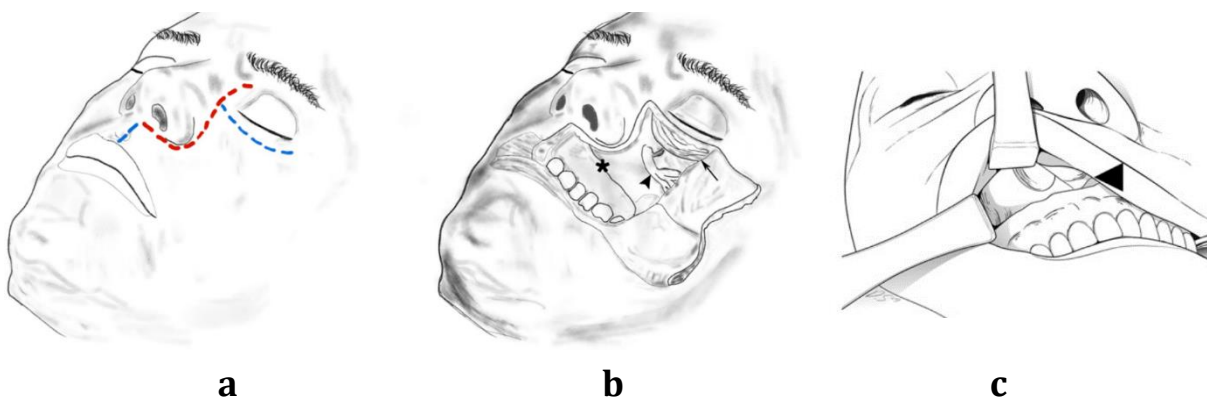


Figure 1.4. Schematic overview of surgical approaches for a maxillectomy. **a)** Lateral rhinotomy (red line) and Weber-Ferguson (blue line) incision. **b)** Elevated myocutaneous flap showing the maxilla (*) orbicularis oris muscle (→) and infraorbital nerve (>). **c)** Facial degloving: transfixion and gingivobuccal incision (black arrow) [27], [86].

- **Weber-Ferguson:** an extended lateral rhinotomy incision to the orbit and lips to reach the palate as seen by the blue dotted line of see Figure 1.4 a.
- **Facial degloving:** Exposure of the midface, alternative to the lateral rhinotomy (see Figure 1.4 c). This is the most minimally invasive procedure because of the major advantage that no external facial incisions are needed [27]–[29].

1.1.6 Maxillectomy classifications

There are several ways to classify maxillary defects. Classification systems can guide the planning of a maxillectomy and reconstruction. Several classification systems exist, like Aramany's (1987), which divided the maxillary defect with the abutment teeth into six categories. Spiro et al. (1997) came up with a simple system that divided the maxillary resection into either limited, subtotal, or total. The Brown et al. (2000) classification, the most commonly used system, classifies both in the horizontal and vertical direction as visualized in Figure 1.5 and described in Table 1.1 [30], [31].

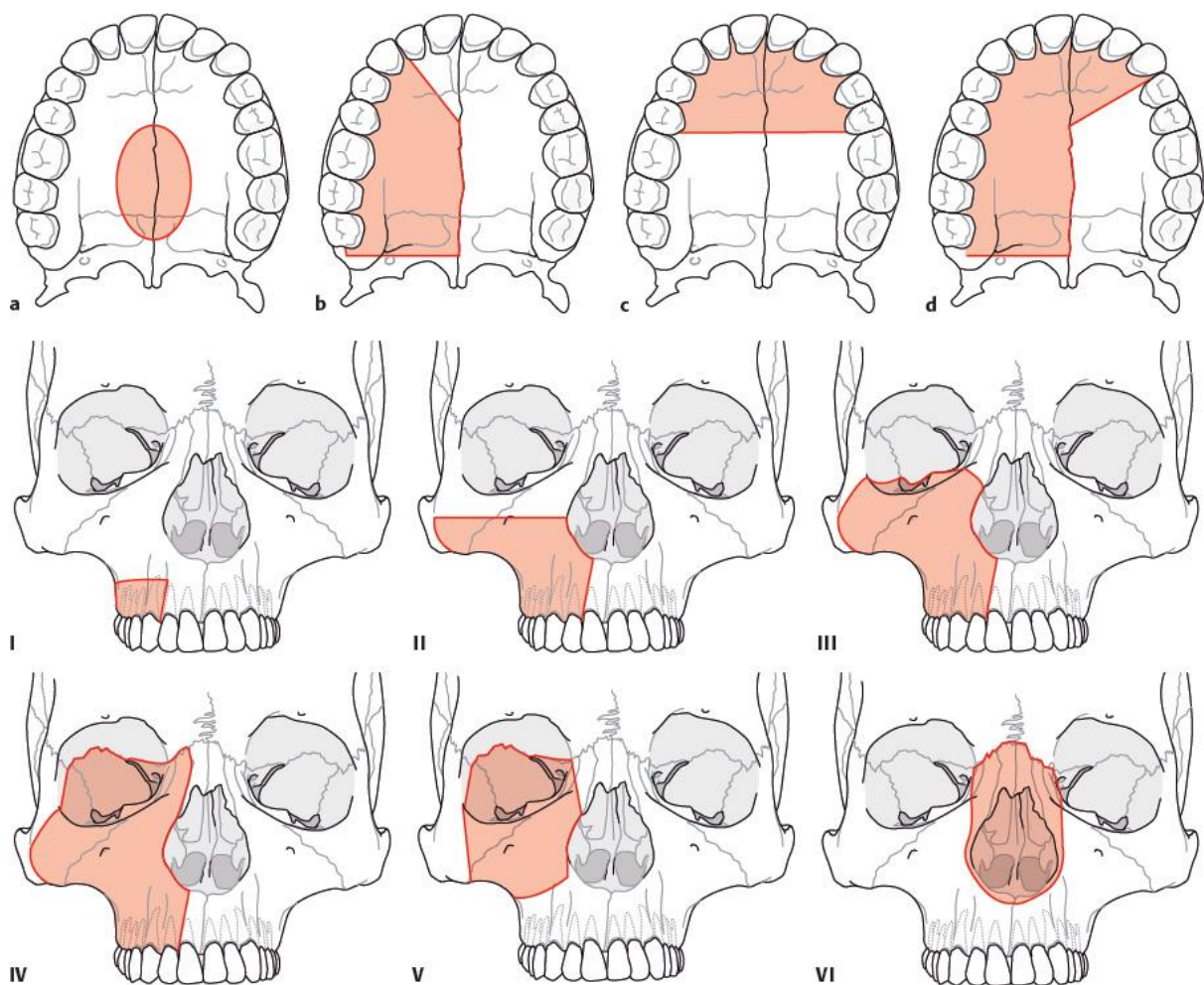


Figure 1.5. Brown's classifications for maxillary defects (red areas), divided into a horizontal (upper panel a-d) and a vertical component (middle and lower panel I-VI) [18].

Table 1.1. Brown's classification of maxillary defects [25].

Vertical	
Class I	Maxillectomy without an oronasal fistula.
Class II	Maxillectomy not involving the orbit.
Class III	Maxillectomy involves the orbital adnexa with orbital retention.
Class IV	Maxillectomy with orbital enucleation (eye removal) or exenteration (entire orbital removal).
Class V	Maxillectomy with an orbitomaxillary defect.
Class VI	Maxillectomy with a nasomaxillary defect.
Horizontal	
a	Only palatal defect without the dental alveolus.
b	The palatal defect is less than or equal to half unilateral.
c	The palatal defect is less than or equal to half bilateral or transverse anterior.
d	The palatal defect is larger than half maxillectomy.

1.1.7 Reconstruction of the maxillary defect

To reconstruct the maxillary defect and therefore improve the deglutition and mastication, speech, and the overall quality of life, several reconstructive options exist. The reconstructive options are still evolving from either using an obturator prosthesis, or surgical reconstruction methods (i.e., regional soft tissue and or bone flaps, free soft tissue and or bone flaps, autogenous implants, and alloplastic implants) [2][32].

This research, however, focuses on the obturator prosthesis as the permanent reconstructive method, which is the most used treatment worldwide due to its safety and has the least operative time [33]. The obturator can replace both hard and soft tissue to close the oral and nasal cavities. Also, the obturator has the advantage that it can immediately restore dentition, and improve the facial appearance [2]. In addition, the obturator allows for a simplified clinical examination of the treated area compared to the other reconstructive approaches, which is important for possible early detection of tumor recurrence after removal [23], [33]. The maxilla obturators are classified into three types:

- Immediate surgical obturator: inserted at the time of surgery.
- Interim obturator: fabricated two-four weeks after surgery.
- Definitive obturator: fabricated three-six months after surgery [32].

Immediate surgical obturator

The immediate surgical obturator (ISO) refers to immediate coverage of the palatal defect. Before surgery, the prosthodontist discusses the planned surgical treatment with the surgeon to determine the incision and amount of resection. Next, the prosthodontist obtains a dental impression of the patient with an irreversible hydrocolloid. The impression is poured into a dental stone to create a dental plaster cast [34][35]. The prosthodontist marks the discussed resection margins on the cast and sends the cast to a dental lab to create a working cast. The alveolar resection margins are removed from the working cast, and the so-called C-claps retention wires are created around the remaining teeth. The C-claps are fabricated from stainless steel orthodontic wires. Next, a 2 mm thick transparent baseplate is fabricated from the working cast using heated polymerizing clear acrylic resin. The transparency of the baseplate allows visible inspection of the clinical fit [1], [34].

The obturator is hand-kneaded by the prosthodontist in the operation room (OR) directly after the tumor resection. The prosthodontist uses a moldable thermoplastic material to create a

bulb on top of the baseplate [35]. Figure 1.6 shows two ISOs, both three weeks post-operative for (a) a hard palate defect using silicone putty and (b) a soft palate defect using flexible silicone. This study, however, focuses only on the hard palate defects. The bulb is fabricated greater than the maxillary defect, mostly at the lateral side, to prevent sunken cheeks. For large palatal defects, a split-thickness skin graft is used to create a layer between the defect and the mucosa junction and creates stabilization of the prosthesis [32]. The prosthesis is stabilized by retention wires, which are connected to the temporal process of the zygomatic process (Figure 1.7), or hooked around



Figure 1.6. Two examples of the immediate surgical obturator (ISO), both three weeks post-surgery. **a)** An ISO for a hard palate defect. **b)** An ISO for a soft palate defect.

the patient teeth [4], [36]. For edentulous patients and total maxillectomy patients, palatal bone screws, titanium implants, or sutures into the surrounding mucosa can also be used to retain the prosthesis. In case of severe bone atrophy, circumzygomatic wiring for edentulous patients is the easiest and most cost-effective method [32], [37].

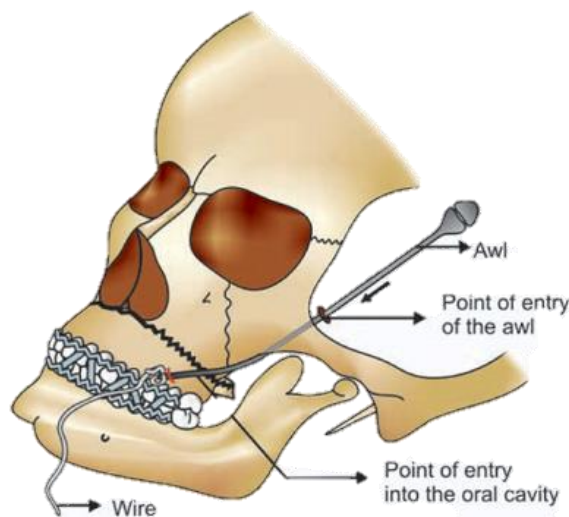


Figure 1.7. Schematical illustration of circumzygomatic wiring [87].

Interim obturator

After 2-4 weeks of surgery, the wound has altered in shape and size due to the quick soft tissue changes that take place within the defect during the healing of the wound. The obturator could consequently be too loose or too tight. Therefore, an interim obturator can be created, by relining the existing prosthesis or by creating a new one [32]. The interim obturator is periodically readapted or relined to fit with the tissue adjustments [4]. A new obturator is often fabricated from acryl resin with wire clasps around the remaining teeth [23], [38].

Definitive obturator

After three to six months, when the defect is completely healed, a definitive obturator is fabricated (see Figure 1.8). The definitive obturator consists of a metal framework of cobalt-chromium, which offers retention, support, and stability [32], [39]. The design of the definitive obturator depends on the size and the shape of the defect, and the absence/presence of the remaining teeth [23]. The prosthesis must have enough retention but without difficulty during insertion and removal of the prosthesis by the patient. Follow-up adjustments of the prosthesis are necessary to optimize speech and nasal leakage of fluids [40].



Figure 1.8. Definitive obturator prosthesis [88].

1.2 Problem statement

1.2.1 Conventional obturators

Besides the advantages of the maxillary prosthesis, the immediate surgical obturators are, on the other hand, large, high-weighted, and unstable. The size and weight depend on the maxillary defect, in the case of a large defect, the obturator can weigh about ± 70 -80 grams. The challenge in heavily weighted obturators is to obtain adequate retention. Besides, the silicone putty is also porous and susceptible to fluid and bacterial uptake, which further increases the weight and results in a foul smell [3]. These disadvantages often reduce the patient's function and comfort. Creating a hollow maxillary obturator could reduce the weight of the prosthesis by 7 – 33 %, depending on the size of the defect [4].

Furthermore, the fabrication of the prosthesis can be rather challenging, including material dispensing, packaging, and shipping. Also, at the lab, the materials need to be plastered, poured, die-cutting, and more [4], [41], [42]. In addition, the tight collaboration between the prosthodontist and the surgeon can be logistically challenging. Besides logistical and time-consuming limitations, the hand-kneaded shape of the obturator is experience-based by the prosthodontist. The varying shapes can lead to an unpredictable obturator fit, loss of retention, and pain [1].

1.2.2 Concept CAD/CAM workflow

Computer-aided design and computer-aided manufacturing (CAD/CAM) designed obturators may overcome the limitations of the conventional method. Researchers at the Netherlands Cancer Institute—Antoni van Leeuwenhoek Hospital (NKI-AVL) designed an in-house concept CAD/CAM technology workflow for fabricating a 3D printed baseplate and a hollow bulb obturator [43]. The 2 mm thick air-filled bulb is merged to a baseplate, designed from a TRIOS 3Shape (Copenhagen, Denmark) intraoral scan (IOS) of the upper teeth and palate, as seen in the different views of

Figure 1.9. The hollow bulb concept CAD/CAM workflow indicated great potential in reducing the weight compared to the solid putty obturator and, as a result, improving the patient's comfort with future ISOs [43].

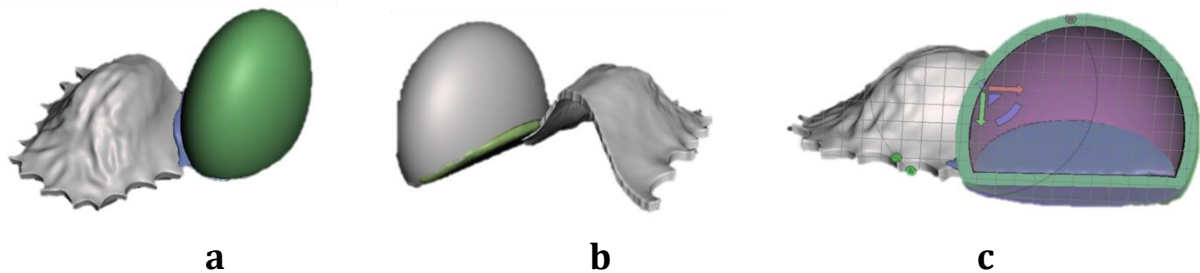


Figure 1.9. Hollow bulb immediate surgical obturator design. **a)** Frontal-lateral view. **b)** Dorsal-medial view. **c)** Sagittal cross-section of hollow bulb [43].

The hollow bulb design, however, is limited to its round shape and does not correspond entirely with the varying shape and size of the conventional ISO. Contrary to the design, the conventional ISO tends to exceed the bony resection margins, especially in larger defects. Increasing the size and improving the shape of the CAD/CAM obturator would gain more weight reduction and, as a result, increase the patient's comfort. Recreating the exact shape, however, can be rather difficult because no research has been published yet about the different types and shapes of the ISOs. In addition to the shape, the overall concept CAD/CAM workflow contains steps that require manual decision-making and is rather complex. Furthermore, the clinical fit of the hollow bulb obturator shape highly depends on the performance of the surgeon. Finally, the design and workflow cannot be clinically implemented yet; it lacks sufficient clinical usage components such as the C-claps and a boulder for circumzygomatic wiring. An optimized obturator shape and workflow could overcome these disadvantages.

1.3 Objectives

This research aims to create a user-friendly workflow for the fabrication of novel optimized hollow immediate surgical obturators. Based on the stated problems, the main objective of this research is:

Create a user-friendly computer-aided design and manufacturing workflow for the fabrication and clinical implementation of the 3D printed hollow immediate surgical obturator to improve the clinical fit, reduce the weight, and increase the maxillectomy patient's comfort.

The research is divided into 3 objectives:

1. Develop an optimized and user-friendly concept workflow containing a novel obturator design.
2. Develop a classification system for the ISO shape prediction to gain an improved clinical fit and weight reduction and therefore increase the patient's comfort.
3. Research the material properties and structural safety of the CAD/CAM design.

1.4 Thesis outline

This thesis is divided into four chapters. After the general introduction, the workflow and clinical fit during several maxillectomy's of the novel CAD/CAM-designed obturators are described. The third chapter describes the retrospective study, which compares the shape, volume, and weight reduction between the conventional and CAD/CAM-designed IOSs. Finally, the fourth chapter describes the mechanical properties of one of the digitally designed prostheses.

1.5 Technical background

1.5.1 CAD/CAM obturators

Recently, several studies started with the design of CAD/CAM obturators to overcome the disadvantages of the conventional method. Besides the fabrication of obturators, CAD/CAM has been used successfully for improved prosthetic dentistry fabrication for many years, allowing virtual surgical planning with high accuracy, which also saves time and cost [41], [44]. For example, Noh et al. (2016) used CAD/CAM technology to fabricate zygomatic implants for additional support of a maxillary prosthesis. In addition, Soltanzadeh et al. (2019) used CAD/CAM technology for a 3D-printed metal framework for a maxillofacial prosthesis [44].

For the imaging acquisition of the CAD/CAM prosthesis, besides imaging techniques such as CT and MRI, intraoral scanning technology can be of use. This optical imaging technique is easy-to-use, light-weighted, and cost-effective, using confocal microscopy to increase the optical resolution and contrast [42], [45]. Michelinakis et al. (2020) compared the accuracy of three types of IOS in which the TRIOS 3Shape IOS being the most precise scanner according to their research (see Figure 1.10) [46]. Furthermore, a recent study by Brucoli et al. (2020) used the TRIOS 3Shape IOS for the fabrication of a definitive obturator prosthesis for twenty-eight patients with a maxillary and/or palatal defect [42]. In addition, Koyama et al. (2019) designed a 3D printed workflow using IOS for definitive hollow bulb obturators [47].



Figure 1.10. The 3Shape TRIOS intraoral scanner [89].

Figure 1.11 shows schematically the differences between the conventional solid putty obturator and a 3D printed hollow CAD/CAM surgical obturator with tissue conditioner (TC). Hollowness instead of a solid obturator decreases the weight of the obturator [48]. The tissue conditioner is a soft lining material, a mixture of powder and liquid in which several brands exist, the NKI-AVL uses Coe-soft. The use of tissue conditioner for a CAD/CAM obturator, instead of the conventional molding material putty, is because of the difference in tensile bond strength to the 3D print [49]. As seen on the inside of the CAD/CAM obturator in Figure 1.11, the air-filled obturator consists of a thin 3D printed layer of a transparent Clear resin (Clear). The surrounding

layer of tissue conditioner enables a precise clinical fit, increases the patient's comfort, and allows post-operative adjustments in the follow-up visits.

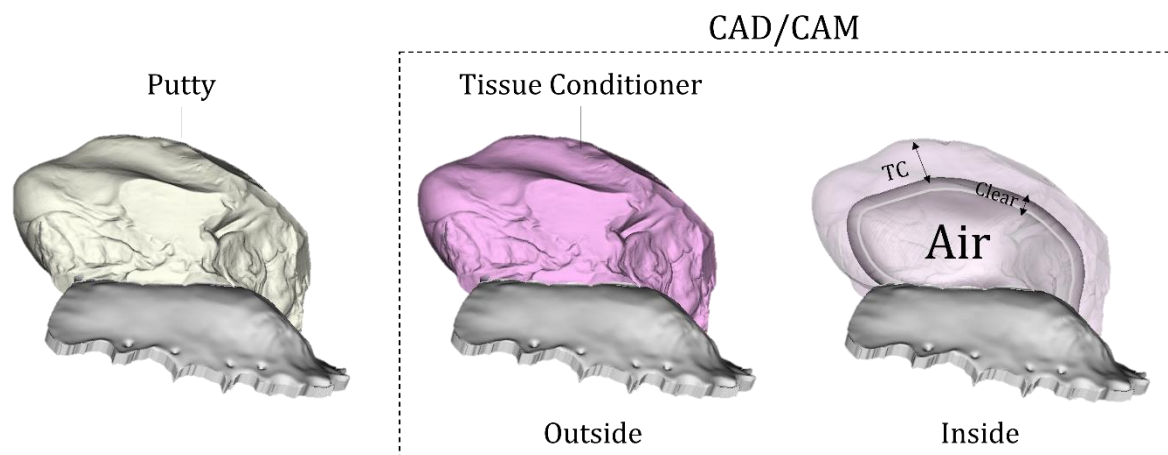


Figure 1.11. Schematically illustrated differences between the conventional solid putty obturator (left panel) and the hollow computer-aided and manufactured (CAD/CAM) obturator. The air-filled CAD/CAM obturator consists of a thin layer of clear resin, surrounded by tissue conditioner, which is a soft denture lining material.

2. Clinical evaluation of the CSM obturator

2.1 Introduction

Recently, several pilot studies have been published about the fabrication of hollow CAD/CAM-designed ISOs to reduce the weight of the conventional ISO. For example, the study by Dartaguiette et al. (2021) used the contours of soft tissue in segmented cadavers from CBCTs to develop CAD/CAM-designed ISOs [50]. Kortés et al. (2018) used both MRI and CT to create the obturator based on the tumor contours [1]. However, both workflows are complicated, time-consuming, and experience-based and thus not user-friendly. In addition, they did not consider that the CAD/CAM design needs to be cable of being reduced in size by the prosthodontist during the follow-up visits. Creating a more automatized method for the varying shapes and sizes of the obturator is therefore necessary.

2.1.1 Previous work: the hollow bulb obturator

As mentioned in the previous chapter, the NKI-AVL started researching a concept CAD/CAM workflow for the fabrication of a baseplate and round hollow bulb obturator [43]. This workflow of A. Steenhuis uses CT scans and intraoral scanning technology for the design of the prosthesis. The hollow bulb design consisted of fitting and resizing a sphere around the bony resection margins as seen in Figure 2.1. Although the workflow has the potential in obtaining a generalized shape for the obturators, it can be optimized in terms of fewer technical and manual steps. Also, the workflow is limited to its round shape, which is contrary to the shape of the conventional ISO, which exceeds the resection bone to find its support in surrounding soft tissue.

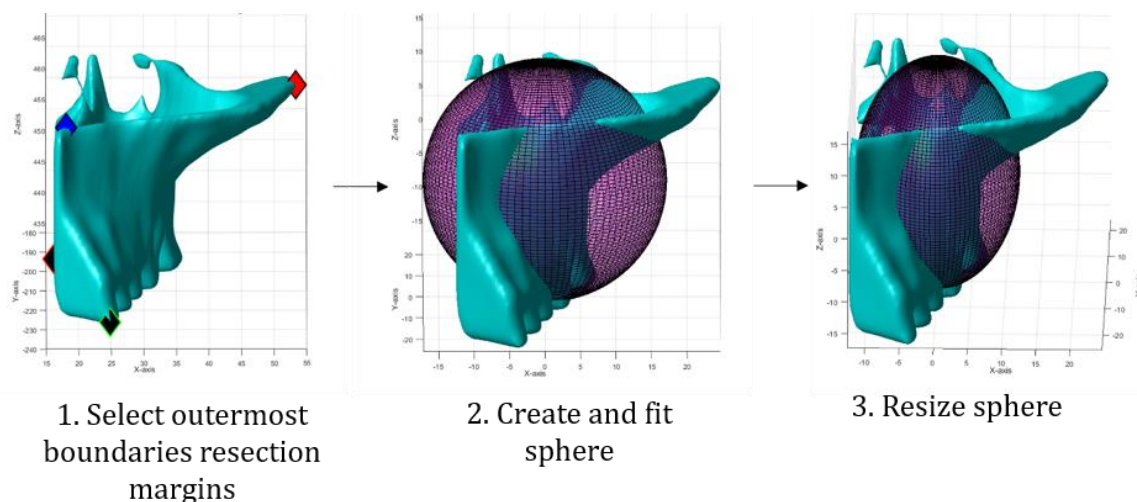


Figure 2.1. Workflow of the computer-aided and manufactured designed hollow bulb immediate surgical obturator in MATLAB (version: R2021a, MathWorks, USA). **1.** The selection of the outermost boundaries of segmented resection margins from a pre-operative CT scan. **2.** A graphical sphere is fitted around the resection margins. **3.** The sphere is reshaped and translated to fit the segmented resection margins.

2.1.2 Hollow closed surface model

This study aims to improve the concept digital NKI-AVL workflow by using a novel method to improve the obturator design, it is called the closed surface model (CSM) obturator (see Figure 2.2). This method fabricates a CSM automatically around all outermost resection boundaries. Figure 2.2 shows an example of a segmented maxilla and its resection bone (blue) from a CT scan. A yellow CSM shape is then automatically fabricated by following the outermost surface points of the resection bone. For larger resection types, the conventional ISO is larger than the resection alone to prevent sunken cheeks. To achieve an enlarged CSM obturator volume, other segmented surrounding tissue besides the resection bone can be included in the design. Figure 2.3 shows an IOS of the upper jaw with examples of such segmented surrounding hard- and soft tissue which can be included in the design. The hollow bulb and CSM shapes are both designed from the pre-operatively planned segmented resection margins. Therefore, the way that the designs fit in the patients 'mouths (referred to in this study as clinical fit) also depends on the surgeon's performance. For this reason, it is key to intra-operatively navigate the pre-operatively virtual planned resection margins.

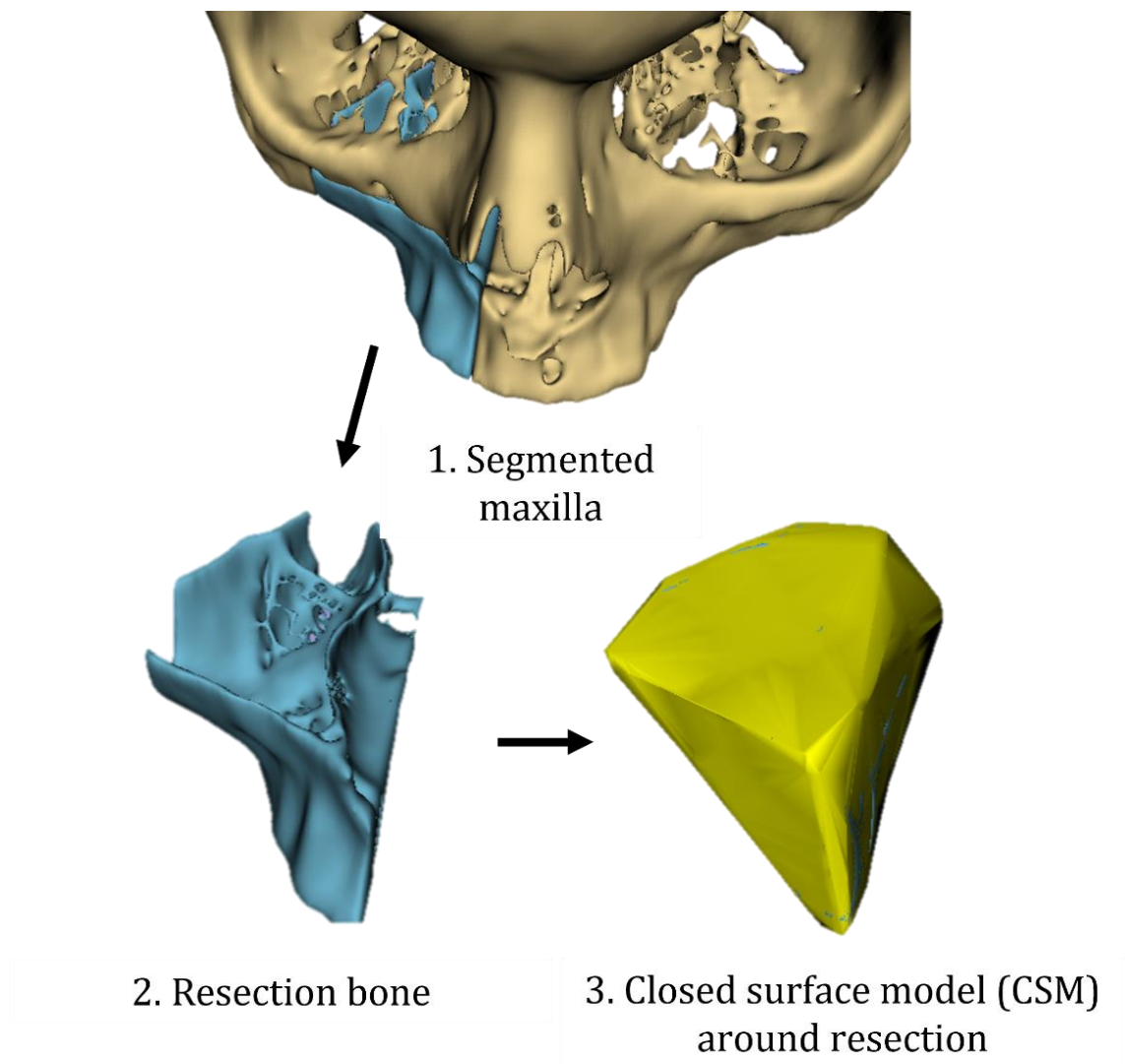


Figure 2.2. Design steps of the closed surface model (CSM) obturator from segmented maxillary resection margins in the open open-source software application 3D Slicer using the 'Marksup to model' extension.

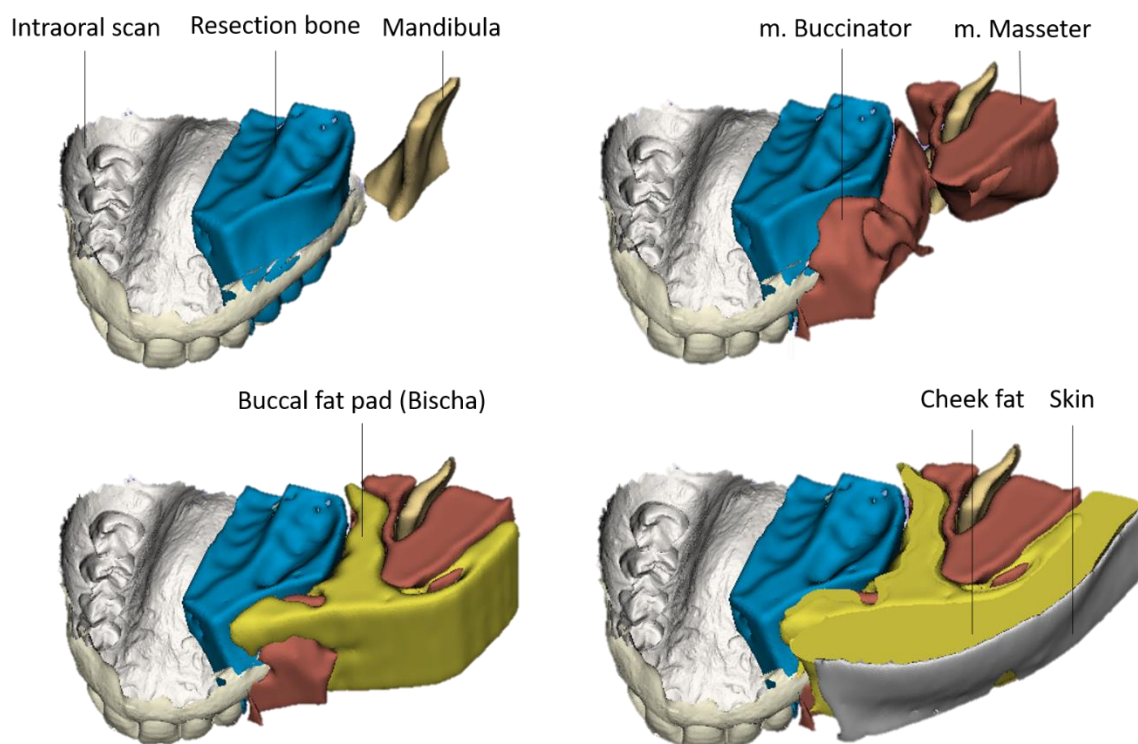


Figure 2.3. Intraoral scan of the upper jaw with segmented CT tissues in the open-source software application 3D Slicer. The figures include the bony resection margin (dark blue) and surrounding soft-tissue parts: buccinator and masseter muscle (red), buccal and cheek fat (yellow), and skin (grey).

2.1.3 Study aim

The following chapter reports the outcome of a clinical trial study of four maxillectomy patients, aiming to evaluate the shape and clinical fit of the novel semi-automatic workflow of the CAD/CAM designed hollow CSM obturators. After examination of the clinical fit, the surgical defect was obturated according to the conventional method. Therefore, this study also aimed to post-operatively compare the weight difference of these conventional putty obturators with the weight of the CSM design. In addition, this research aimed to create a user-friendly digital workflow in which the workflow was optimized throughout the research to obtain this goal. Different types of CSM obturators were thus designed based on the outcome of each clinical case throughout the study. In addition, several scales of the CSM design were researched to investigate the optimal clinical fit, considering that the conventional ISO is polished and reduced in size during the post-operative follow-up appointments.

2.2 Method

2.2.1. Patients

The clinical trial study included all patients who underwent a maxillectomy in the AVL-NKI hospital during the time of research (Oct 2021 – Aug 2022). The criteria for each patient included that a pre-operative CT scan and IOS were available. In addition, the surgical operation needed to consider the hard palate, in which a prosthodontist obturated the defect. The inclusion left four patients who were enrolled in the clinical trial study. Figure 2.4 shows the segmented skulls of each patient in Slicer, with the resection margins highlighted in dark blue.

2.2.2 CT analyses

All scans were acquired at the NKI-AVL using the same CT scanner and settings. Patient 1 underwent a PET-CT scan with a reconstructed slice thickness of 2.0 mm, performed with 140 kVp and exposure 117 mA. The field of view was 512x512 pixels and pixel spacing was 1.17 x 1.17 mm. The CT dose index (CTDI_{vol}) was 6 mGy and the dose length product (DLP) was 239.91 mGy*cm. Patients 2-4 underwent CT scanning with a reconstructed slice thickness of 1.0 mm, performed with 120 kVp and exposure 175 mA. The field of view was 512x512 pixels and pixel spacing was 0.47 x 0.47 mm. The CTDI_{vol} was 22 mGy and DLP 536.1 – 635.3 mGy*cm.

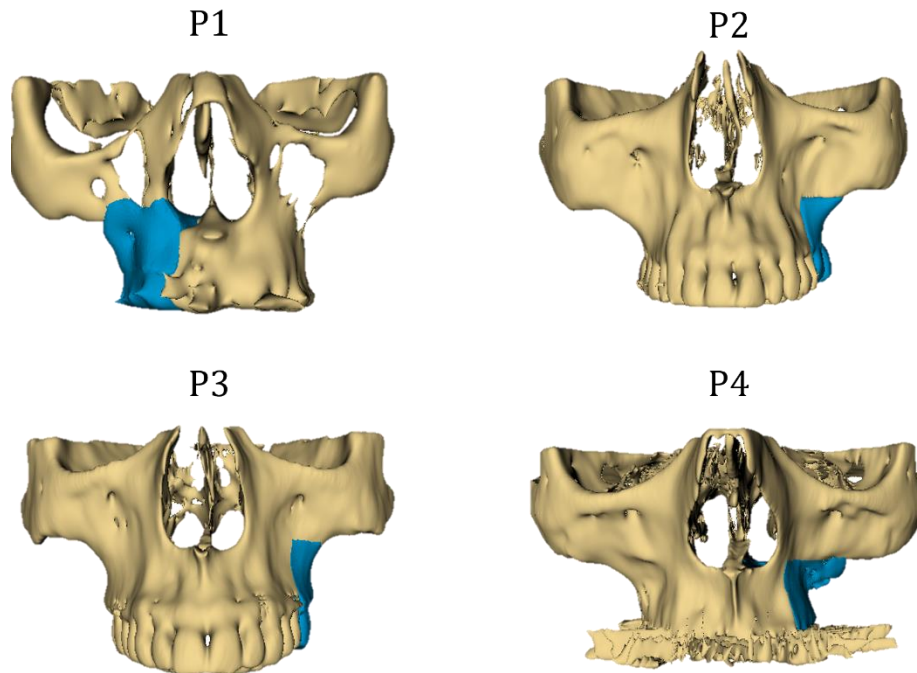


Figure 2.4. Segmented skulls of each included patient (P) in 3D Slicer with the resection margins highlighted in dark blue.

2.2.3 Pre-operative virtual surgical planning

Figure 2.6 gives a schematically overview of the NKI-AVL optimized CAD/CAM workflow for fabricating the 3D printed hollow CSM ISOs, which will be explained further in the following sections. First, the pre-operative head CT scan from PACS and the IOS of the upper jaw, exported as a Stereolithography (STL) file from the TRIOS 3 Shape software, were loaded into Slicer (Slicer 4.4.0 software (Surgical Planning Lab, Harvard Medical School, Harvard University, Boston, USA). The CT scan was used for semi-automatic greyscale thresholding of the bones [51], [52]. A region of interest (ROI) around the maxillary resection margins was then virtually planned together with the head-and-neck surgeon. The CT was cropped using the ROI to create a new volume to segment and generate a resection margin model. The surgical oblique cutting direction (palatine bone midline to the resected teeth) was obtained using a vertical plane cut through the resection model. A detailed segmentation protocol in Slicer was developed during this research for reproductive purposes (see Appendix A1). In addition, these steps were encoded in Python for the automatization of the workflow (see Appendix B1).

After finishing the resection model, the IOS was registered to the teeth of the segmented skull using manually selected fiducial point-based rigid-body registration (FPR) by the 'Slicer IGT' extension [53]. For the FPR, an average of four to five fiducial points were used on distinctive characteristics of the teeth (Figure 2.5A). The manual FPR was chosen due to the height difference between the scanned hard palate mucosa and the segmented hard palate bone (Figure 2.5B). The height difference results in a wrong point correspondence when choosing an automatic registration method such as the iterative closest point (ICP) algorithm. The ICP registration finds

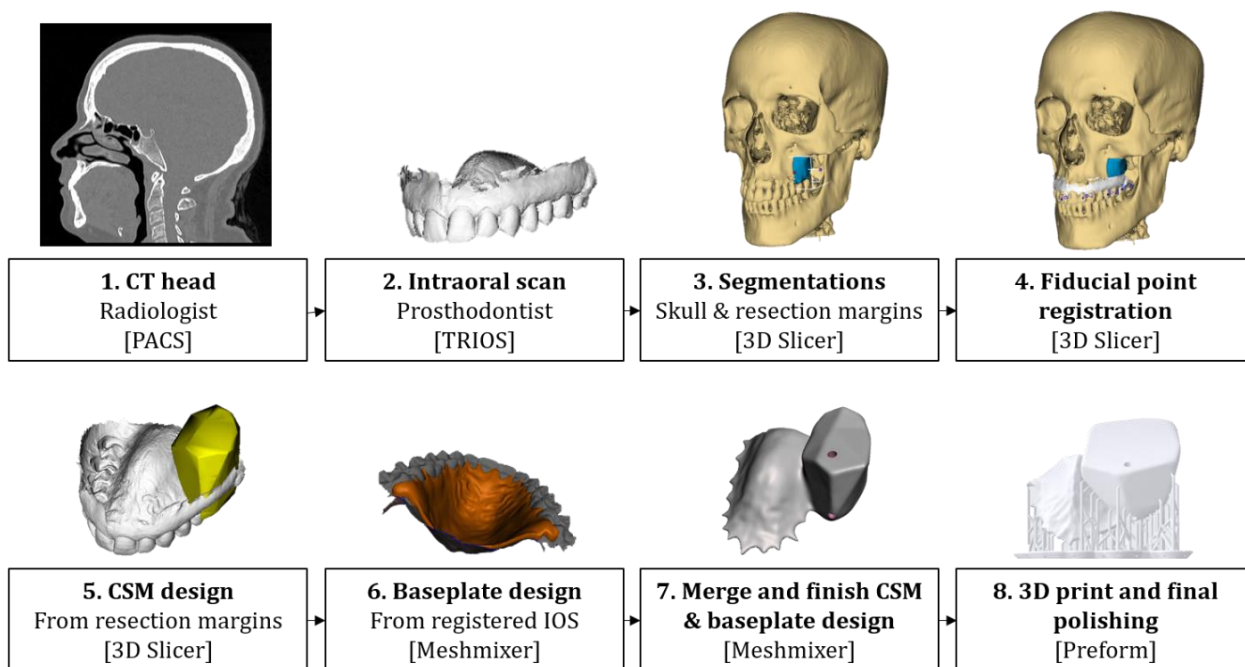


Figure 2.6. Schematical overview of the Netherlands Cancer Institute—Antoni van Leeuwenhoek Hospital (NKI-AVL) in-house concept computed-aided and manufactured (CAD/CAM) technology workflow for fabricating a 3D printed baseplate and closed surface model (CSM) obturator.

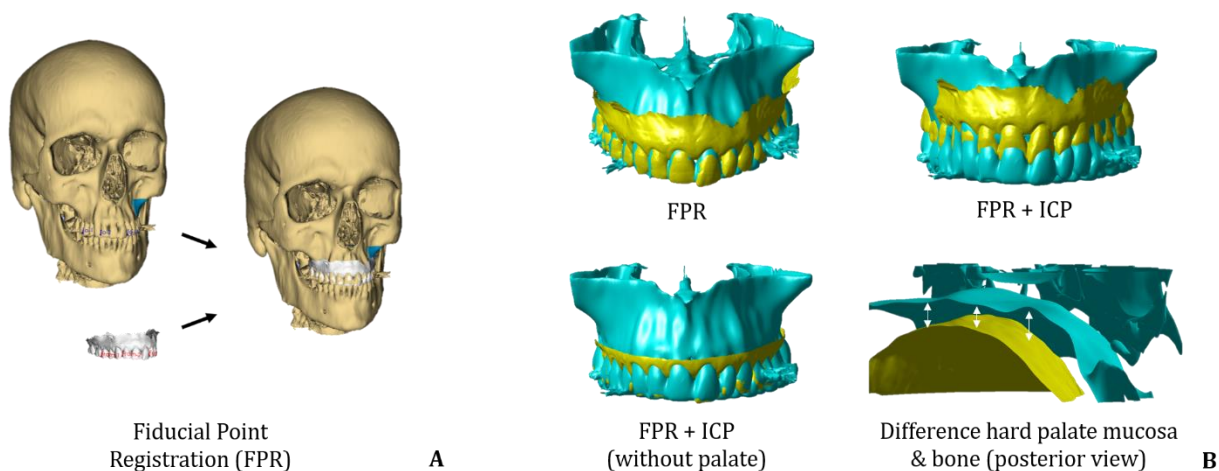


Figure 2.5. Registration of a segmented CT skull and intraoral scan (IOS) of the upper jaw. **A)** Use of four manually selected fiducial point registration (FPR) points on the teeth. **B)** Difference between FPR (upper left), FPR and iterative closest point (ICP) algorithm (upper right), FPR + ICP after removal of the palate (lower left), and the height difference of the palate of the IOS and segmented CT.

the translation and rotation matrices between two 3D point clouds to determine the minimum distances between the points [54]. The analysis of the fiducial registration error (FRE) was calculated by the difference in position between the matching fiducial points: the root mean square (RMS) [53]. In addition, the FRE was visualized by computed distancing mapping between the segmented teeth and IOS of the upper jaw. The final step in Slicer required the design of the CSM around the resection bone by using the ‘Markups to Model’ extension (Figure 2.2). In some of the cases, soft tissue was included in the CSM design (Figure 2.3), which will be further explained for each case in the next sections.

2.2.4 Baseplate design & merge

The CSM obturator was then exported as an STL file and loaded into the freeware Autodesk Meshmixer (Autodesk Inc, San Rafael, CA). The obturator was scaled to different sizes (0.6, 0.7, and 0.8) to investigate the balance between clinical fit and feasibility. Next, the obturator was merged to a 2mm thick, designed baseplate made in Meshmixer from the IOS of the upper jaw. The baseplate was designed according to the protocol of the previous NKI-AVL research. A schematical overview of this protocol is presented in Appendix C [43]. Excessive parts were removed and smoothed from the merged model to prevent sharp edges within the patient's mouth. Next, the obturator was made hollow, again with a thickness of 2mm. Hollow tubes with a 1.5mm radius were subtracted from the design to prevent 3D print failures due to the air trapping of the hollow print [55]. Finally, the finished model was exported again as an STL file. A schematical overview of the steps in Meshmixer is visualized in Figure 2.7.

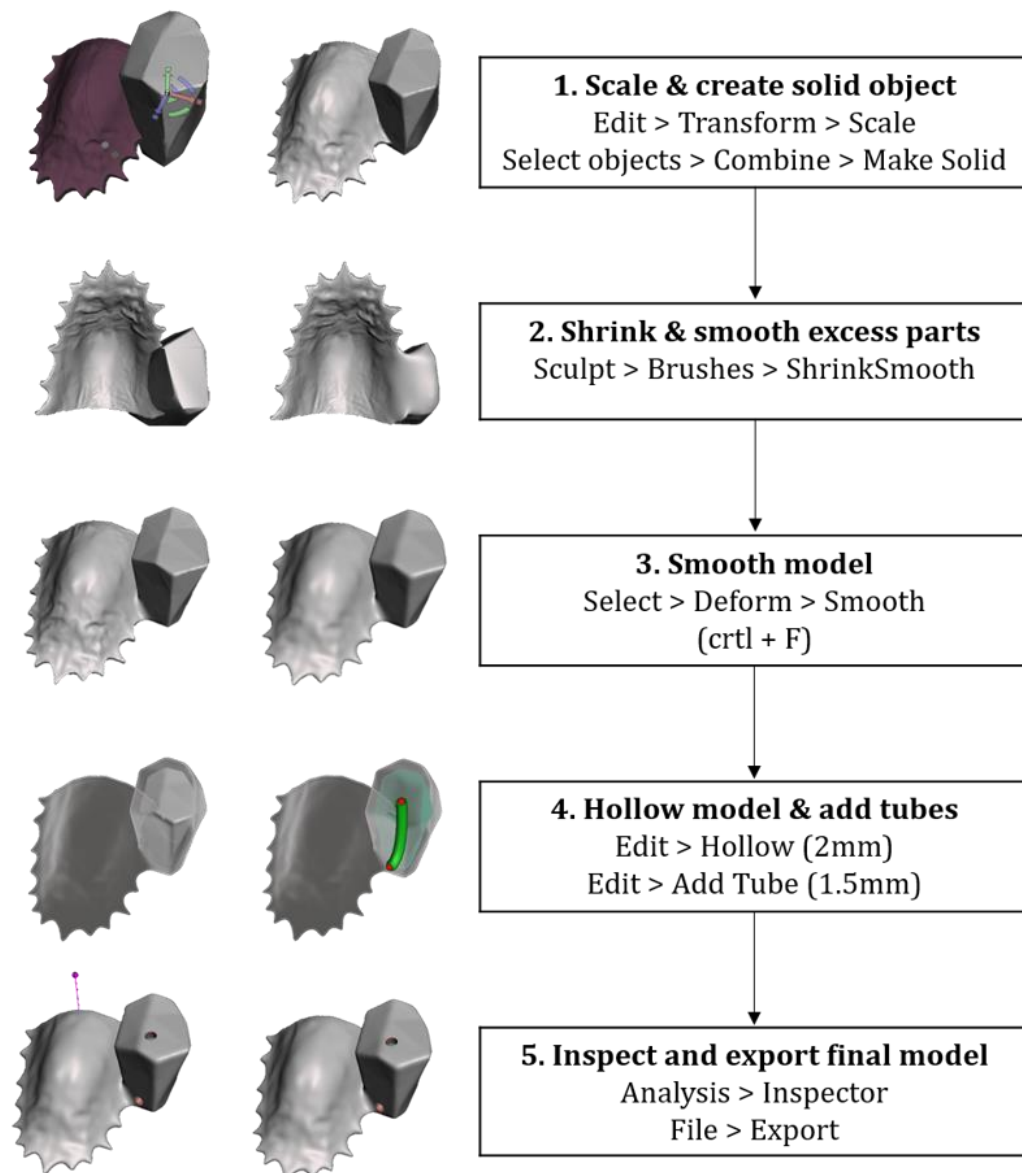


Figure 2.7. Schematic workflow of the merge and finish of the obturator and baseplate in Autodesk Meshmixer. After scaling the obturator, the two objects are merged and smoothed. The obturator is designed hollow with a 2mm thick layer in which 1.5mm tubes are subtracted from the model to allow the air to escape during printing. Finally, after the mesh inspection, the model is exported for printing.

2.2.5 3D printing and final polishing

For the final finish, external supports were added to the STL models in the PreForm version 3.19.1 software (FormLabs Inc., Somerville, MA, USA). Next, the models were printed in Clear resin V4 with the Form 3 (Formlabs Inc) stereolithography (SLA) printer with a layer thickness of 100 μm . The printing was followed by a wash in isopropyl alcohol (IPA) and a cure with UV light [56]. The external supports and sharp edges were removed, the print was polished, and the tube holes were closed using the dental self-curing acrylic material TAB-2000 powder.

2.2.6 Patient-specific obturator design

The patient-specific methods described in this section are in chronological order of the operations. After each case, the methods were discussed and optimized for the next case to obtain a standardized user-friendly workflow. This trial-and-error resulted in different numbers and types of hollow ISOs for each clinical case. The clinical fit for the second, third, and fourth patient were scored numerically from 1 (poor) to 5 (excellent) by the prosthodontist.

The first patient included the resection of the right-sided alveolar bone, from the last molar to the canine (see Figure 2.8). Both the resection margin (blue) and skin of the cheek (grey) were segmented to design an obturator model that reached out to the cheek. The CSM was then cut vertically to agree with the limit of the lateral resection to prevent an overestimation in this direction. The CSM obturator was transformed to a scale of 0.6, 0.7, and 0.8. For comparison, the hollow bulb obturator (Figure 2.1) was also designed, leaving four designed obturator models.

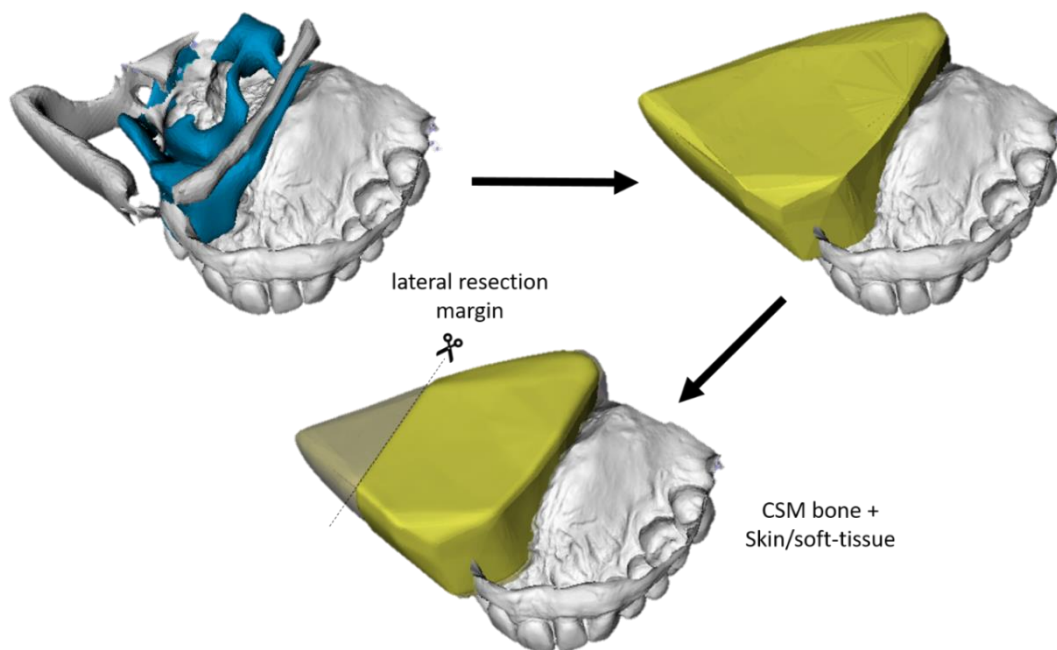


Figure 2.8. Workflow of the obturator design of patient nr. 1. Resection bone (blue) and skin (grey) are segmented in which a closed surface model (CSM) is designed around the segmented parts. The design is then cut vertically to agree with the limits of the lateral resection margin.

The second patient included the resection of the left-sided alveolar bone across the nose septum and three molars. The digital designs included the hollow bulb (Figure 2.1) obturator, followed by five different obturators scaled to a size of both 0.7 and 0.8 (based on the results of the previous case), leaving a total of 11 ISOs. Figure 2.9 gives two examples of the CSM designs: left) a model around the resection bone, right) two combined CSM models around the section bone and the (buccal) fat. Another CSM design included only one CSM for the resection bone and soft tissue. The fourth design included using an IOS file of a putty obturator from a retrospective case

with a similar resection. The final design was a proof of concept by creating the CSM model around manually selected fiducial points. The designs endeavored to prevent overlapping of the model with the lower jawbone. To summarize:

- Hollow bulb
- Two separate merged bone & soft tissue CSMs (2x)
- One bone & soft tissue CSM (2x)
- Retrospective intraoral scanned and fitted putty obturator (2x)
- Model around manual selected fiducial points (2x)

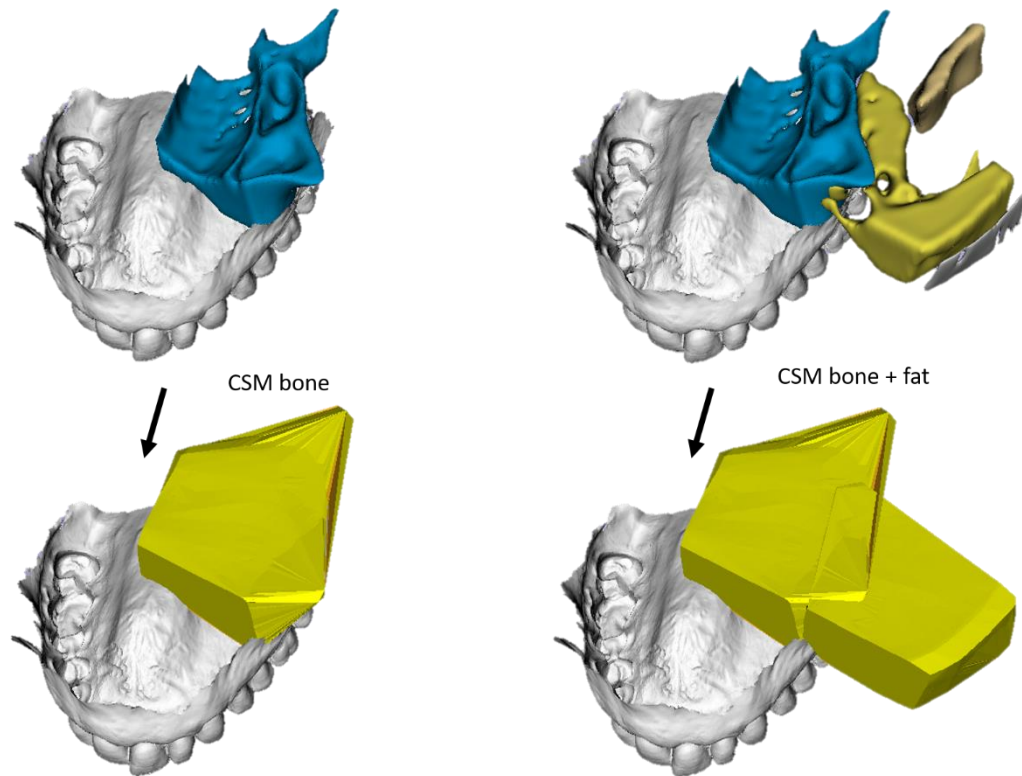


Figure 2.9. Workflow of two obturator designs of patient nr. 2. Resection bone (blue) and buccal fat (yellow) are segmented in which a closed surface model (CSM) is designed around the segmented parts (right panel). In the left panel, the CSM design only surrounds the resection bone.

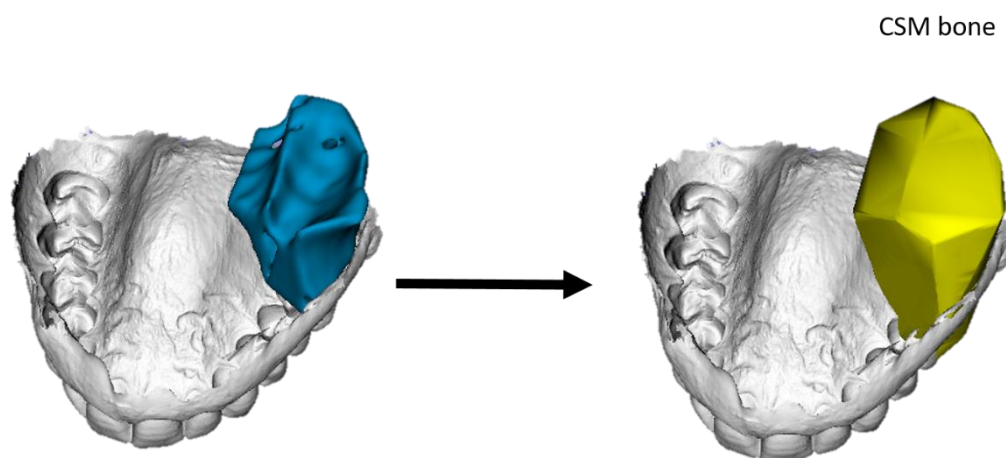


Figure 2.10. Workflow of the obturator design of patient nr. 3. Resection bone (blue) is segmented in which a closed surface model (CSM) is designed around the segment.

The third patient included the resection of the left-sided alveolar bone and three molars. One CSM was designed around the resection bone (see Figure 2.10) in three scaled sizes (0.7, 0.8, and 1.0). In addition, the hollow bulb design was created for comparison, leaving four models in total.

The fourth patient included, like patient 1, the resection of the left-sided alveolar bone, and molars to the canine. A CSM design scaled to 0.8 and 1.0 was created around the resection bone (see Figure 2.11). Two other 0.8-sized designs were created by enlarging the CSM obturators with 5 mm and 10 mm to the lateral side in Meshmixer. In addition, a zygoma wiring bollard on a 0.8 scaled model was designed, and copied from a conventional intraoral scanned ISO of one of the other patients.

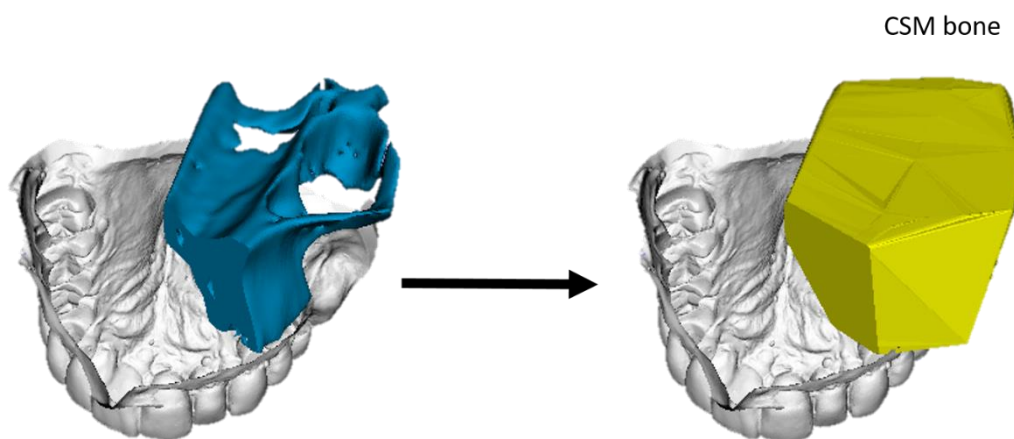


Figure 2.11. Workflow of the obturator design of patient nr. 4. Resection bone (blue) is segmented in which a closed surface model (CSM) is designed around the segment.

2.2.7 Navigation

The in-house Fusion ENT navigation system (Medtronic, Jacksonville, FL) was used for surgical navigation of the virtual surgical planned resection bone (Figure 2.12 A). For the navigation, the resection margins were pre-operative saved as Nearly Raw Raster Data (NRRD) file in Slicer, resulting in a black (0) background and white (1) contoured resection image. The NRRD volume

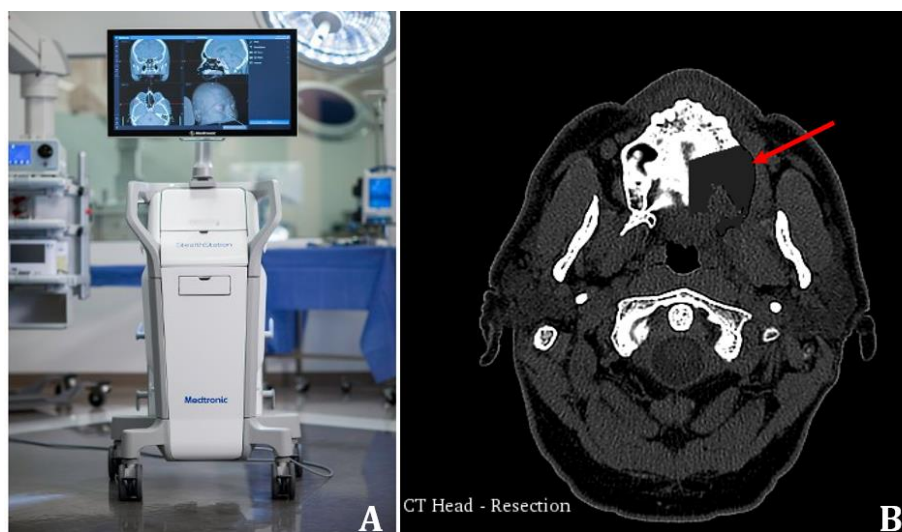


Figure 2.12. Example of virtual surgical planned navigation for a partial maxillectomy. **A)** ENT Medtronic navigation system (Medtronic, Jacksonville, FL). **B)** CT scan of the head with the resection margin subtracted of the scan, visualized as a darker space (red arrow).

was then multiplied with the CT scan to obtain varying greyscale values in the resection area. Next, the multiplied volume was subtracted from the CT scan, resulting in an output volume containing the original scan with the resection area visualized in dark grey contours (see Figure 2.12 B). The output volume was loaded into the Medtronic navigation system for the 3D intra-operative navigation. During surgery, the operator used a navigated pointer to mark the resection margins on the patient before sawing the maxilla and palate bone. After resection, the surgeon checked with the pointer if the resection corresponded with the pre-operative planned margins. A detailed step-by-step protocol of the navigation steps in Slicer developed during this research is found in Appendix A2 and is python scripted for automatization (Appendix B2).

2.2.8 Post-operative analysis

After the clinical fit of the CAD/CAM designs, the defect was obturated with the conventional putty ISO. During the first follow-up visits (T=0), the conventional obturator was removed for volume reduction and polishing by the prosthodontist. After removal, the IOSs were weighted and scanned using the TRIOS 3Shape. To investigate the amount of putty volume reduction, the obturator of P1 was scanned again after 7 weeks (T=7) and registered using FPR to the original sized putty obturator (T=0). The comparison of the putty reduction was made by using colored coded distance maps between the two intraoral scans.

The weights (W) in grams (g) of the digital obturators were calculated by obtaining the digital volumes (V) in Slicer, multiplied by the densities (ρ) of the denture reline (putty & tissue conditioner) and Clear resin. The densities of the materials (see Table 2.1) were based on clinical experiments throughout this research.

Table 2.1. Densities of the denture reline/ resin materials.

Material	Density (g/cm ³)
Putty	1.43
Clear	1.19
Tissue conditioner	1.00

The weight calculations of the digital and conventional obturators were followed by the equations below. The reline material for the conventional ISO included the regular used *Putty* (Eq. 1). The CSM obturator includes a 2mm hollow inner shell of printed *Clear resin* (Eq. 2), and a solid outer shell of *Tissue conditioner (TC)* (Eq. 3). The total weight of the CSM obturator ($W_{CSM\ total}$) is the sum of the inner- and outer shell (Eq. 4). For a visualized perspective, see Figure 1.6 and Figure 2.13.

The weight reduction (W_{red}) was calculated by subtracting the weight of the solid putty ISO (W_{ISO}) from the weight of the CSM obturator ($W_{CSM\ total}$) (Eq. 5). The weight reduction percentage (%) was also calculated (Eq. 6).

$$W_{ISO}(g) = \rho_{putty} * V_{ISO} \quad (1)$$

$$W_{CSM\ inner}(g) = \rho_{clear} * V_{CSM\ inner} \quad (2)$$

$$W_{CSM\ outer}(g) = (V_{ISO} - V_{CSM(solid)}) * \rho_{TC} \quad (3)$$

$$W_{CSM\ total}(g) = W_{CSM\ inner} + W_{CSM\ outer} \quad (4)$$

$$W_{red}(g) = W_{ISO} - W_{CSM\ total} \quad (5)$$

$$W_{red}(\%) = \frac{(W_{CSM\ total} - W_{ISO})}{W_{ISO}} \times 100\% \quad (6)$$

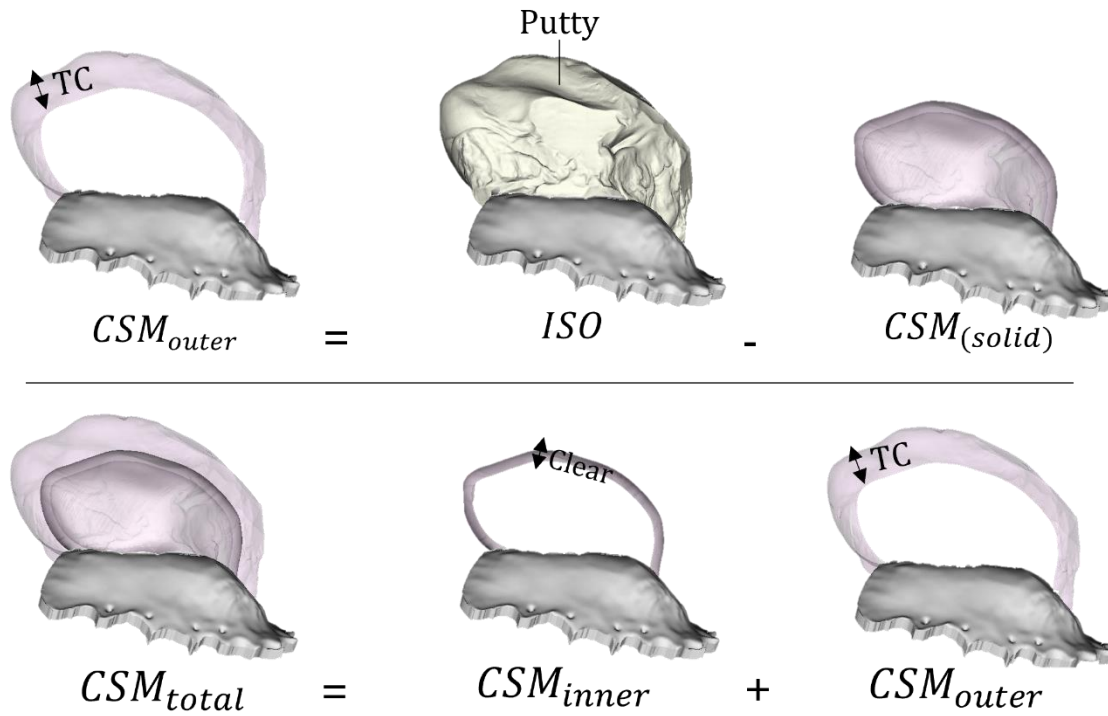


Figure 2.13. Schematical overview of the inner and outer layer calculations of the closed surface model (CSM) obturator. The upper panel visualizes that the outer layer is obtained by subtracting the volume of the conventional obturator with the scaled solid CSM obturator. The lower panel visualizes the summation of the inner and outer shells of the CSM design.

2.3 Results

2.3.1 Patients

Baseline characteristics for the four included patients are shown in Table 2.1.

Table 2.2. Baseline parameters of included patients

Patient No.	Sex	Age (Years)	Type of tumor	Stage	Site of tumor
1	Male	66	SCC	T4N0M0	Right
2	Female	53	PLGA	T2N0M0	Left
3	Male	43	SCC	T2N0M0	Left
4	Male	69	SCC	T2N0M0	Left

SCC = Squamous cell carcinoma; PLGA = Polymorphous low-grade adenocarcinoma.

2.3.2 Registration error

Figure 2.14 shows the result of the FRE in terms of the RMS (mm) of the four clinical cases and is visualized by a distance map overlay of the segmented teeth with the IOS of the upper jaw. As seen by the distance mapping, the overall error is ± 1 mm on the upper teeth. As seen by the RMS, the error is the lowest for patients 2 and 3 at about ± 0.3 mm. The RMS is highest for patient 4, which is also showing the highest number of artifacts around the teeth, seen by the color variation. The resolution of the CT in patient 1 is the lowest as seen by the sharpness and colors of the segmented teeth.

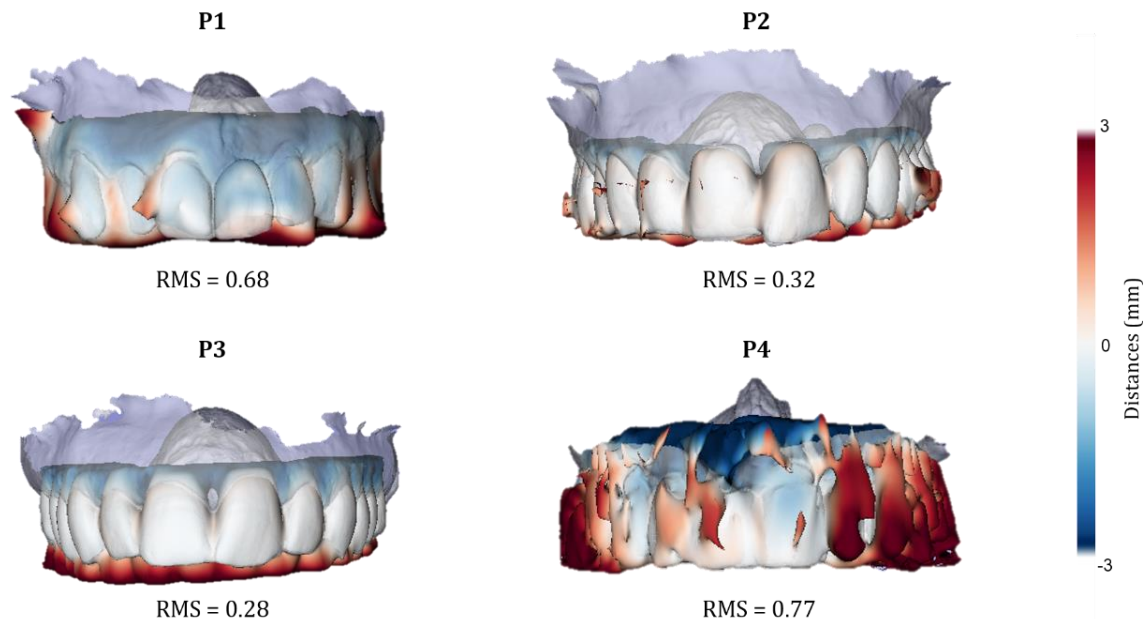


Figure 2.14. Distance mapping of the registration error of the intraoral scan of the upper jaw and segmented teeth of a CT scan for four patients (P). The root mean square (RMS) of each case is given below the registered teeth in millimeters. Note the lower resolution of the segmented CT of P1 and high amount of scattering of the CT of P4.

2.3.3 Clinical evaluation

The outcome of all the CAD/CAM designed ISOs in Autodesk Meshmixer are found in Appendix D. Images of the designs during the fitting in the patient's mouth will be visualized in the following section per patient.

Patient 1

Figure 2.15 shows the result of the OR images of the 3D printed hollow bulb design and the CSM design around bone & soft tissue in three different scales. It can be seen from Figure 2.14 that the lowest scale (0.6) and the hollow bulb had the most underestimated volume compared to the maxillary defect. The CSM scaled to 0.7 indicated a better clinical fit. The volume of the CSM scaled to 0.8 shows the best clinical fit except in the anterior direction, in which the obturator exceeded the remaining alveolar bone.

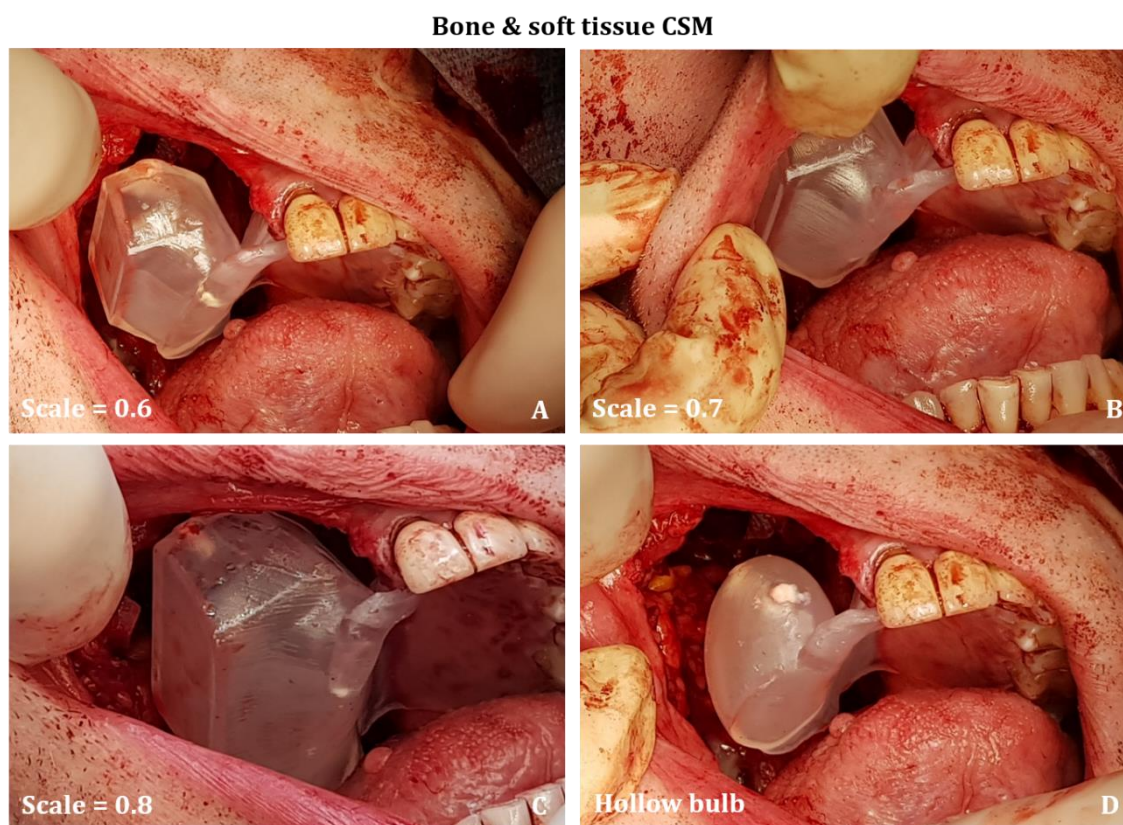


Figure 2.15. Image results of the clinical fitting of the digitally designed prostheses in patient nr. 1, directly after partial resection of the maxilla. The designs included a closed surface model (CSM) around the segmented resection bone and soft tissue in different scales, and a hollow bulb **A)** CSM design scaled to 0.6. **B)** CSM design scaled to 0.7. **C)** CSM design scaled to 0.8. **D)** Hollow bulb design.

Patient 2

Figure 2.16 shows the result of the OR images of the 3D printed hollow bulb design (A), intraoral scanned obturator of a retrospective patient with similar resection margins (B), and four different CSM designs around the bone & soft tissue (C-F). Table 2.3 and Table 2.4 below present the clinical fitting scores from the designs scaled to 0.8 and 0.7 respectively. As can be seen from the tables, the 0.8-scaled obturators showed a better clinical fit compared to the 0.7-scaled. The best scored obturators (score = 4.5) were the 0.8 scaled CSM around the resection bone (D) and the 0.8 scaled IOS scanned obturator (Figure 2.16 B) (score = 4). The worst clinical fit as seen by the scoring tables and on the lateral side of the patient (C+F) were both the automatic bone and soft tissue CSM obturators. The hollow bulb (A) showed an average clinical fit (score = 3) in all directions. The manual CSM (E) showed a bad clinical fit, as seen also at the lateral side.

Bone & soft tissue CSM

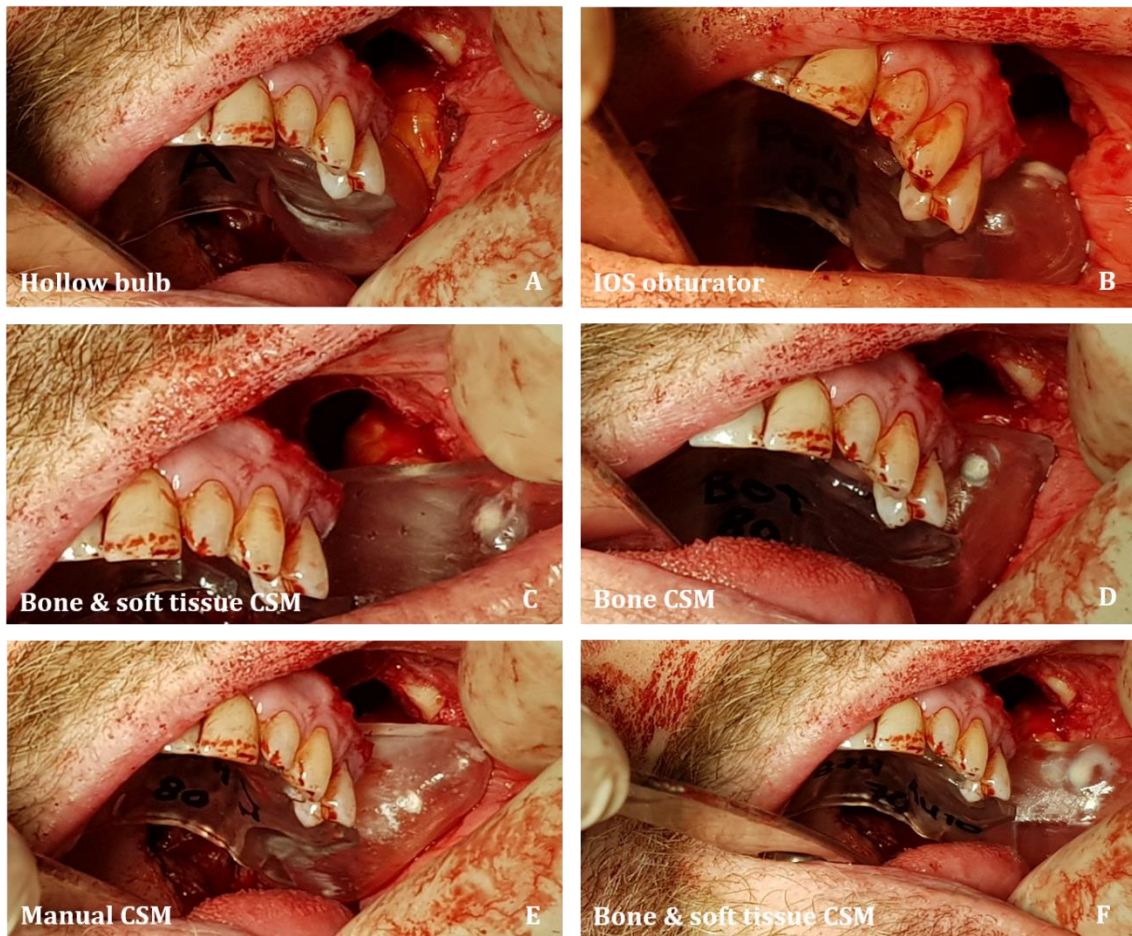


Figure 2.16. Image results of the clinical fitting of the digitally designed prostheses in patient nr. 2, directly after partial resection of the maxilla. The six designs included four different closed surface model (CSM) around the segmented resection (bone) and soft tissue, a hollow bulb, and a fitted intraoral scanned (IOS) obturator. **A)** Hollow bulb design. **B)** IOS of a similar resection. **C)** Automatic two combined CSM's around bone and soft tissue. **D)** Automatic CSM around bone. **E)** Manual selected fiducial points around bone and soft tissue. **F)** Automatic CSM around bone and soft tissue.

Table 2.3. Clinical 0.8 scaled obturator fit in patient nr. 2 scored by prosthodontists.

Design	Poor 1	Bad 2	Average 3	Good 4	Excellent 5
A			X		
B				X	
C	X				
D				X	X
E		X			
F	X				

A = Hollow bulb; B = intraoral scan obturator; C = Two combined bone & soft tissue closed surface model (CSM); D = Bone CSM; E = Manual selected CSM; F = Bone & soft tissue CSM.

Table 2.4. Clinical 0.7 scaled obturator fit in patient nr. 2, scored by prosthodontists.

Design	Poor 1	Bad 2	Average 3	Good 4	Excellent 5
A			X		
B			X		
C	X				
D			X	X	
E			X		
F	X				

A = Hollow bulb; B = intraoral scan obturator; C = Two combined bone & soft tissue closed surface model (CSM); D = Bone CSM; E = Manual selected CSM; F = Bone & soft tissue CSM.

Patient 3

Figure 2.17 shows the result of the OR images of the 3D printed CSM around the resection bone in different scales (A-C) and the hollow bulb design (D). Table 2.5 presents the clinical fitting score results of this case. As shown by both the OR images and the scoring table, each of the CSM designs had a good fit. (score =4). The models connected well with the surrounding tissue except for a little overestimation in the most posterior-inferior corner of the prosthesis when the jaws were enclosing. The differences between the CSM models as visualized in the images are the amount of surrounding space which decreases for the larger scales. The hollow bulb fit scored less compared to the CSM designs.

Bone CSM

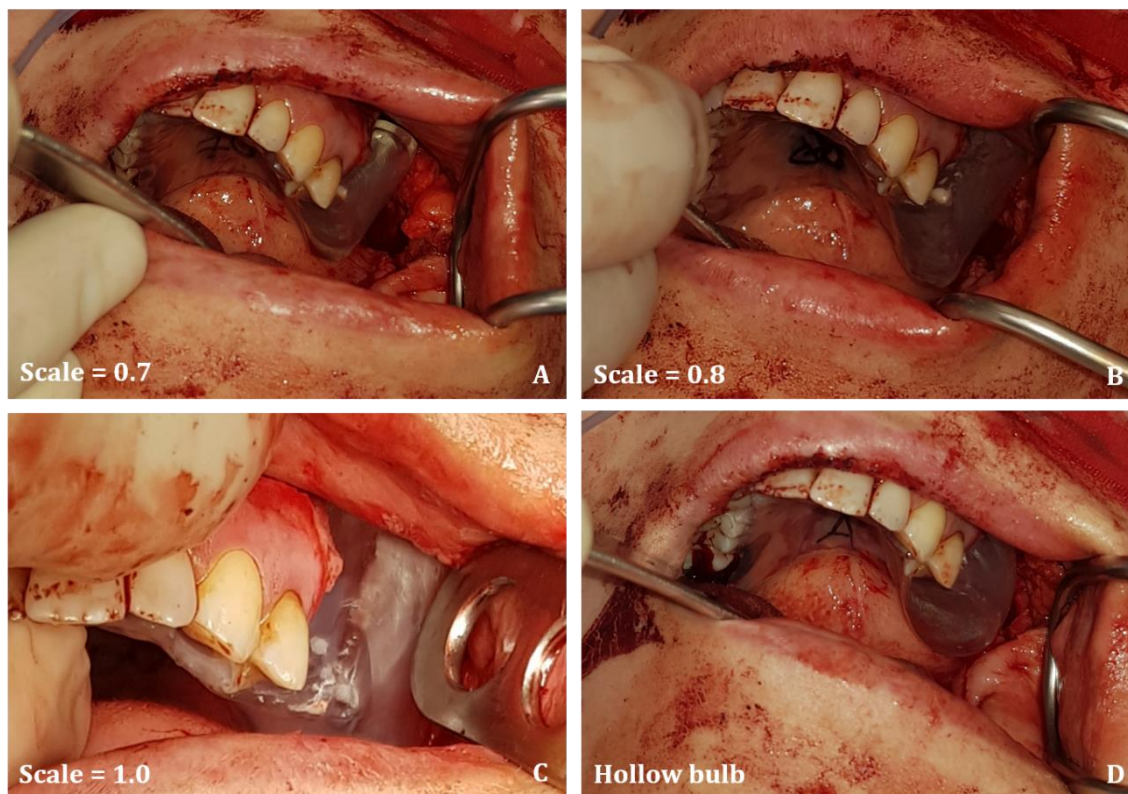


Figure 2.17. Image results of the clinical fitting of the digitally designed prostheses in patient nr. 3, directly after partial resection of the maxilla. The designs included a closed surface model (CSM) around the segmented resection bone in different scales, and a hollow bulb **A)** CSM design scaled to 0.7. **B)** CSM design scaled to 0.8. **C)** CSM design scaled to 1.0. **D)** Hollow bulb design.

Table 2.5 Clinical obturator fit in patient nr. 3 scored by prosthodontists.

Design	Poor 1	Bad 2	Average 3	Good 4	Excellent 5
A				X	
B				X	
C				X	
D			X	X	

A = Closed surface model (CSM), scale = 0.7; B = CSM, scale = 0.8; C = CSM, scale = 1.0; D = Hollow bulb.

Patient 4

Figure 2.18 shows the result of the OR images of the 3D printed CSM around the resection bone, scaled to 0.8 (A-C) and 1.0 (D). The design of Figure 2.18 A show the additional zygoma wiring bollard at the posterior side. The designs of Figure 2.18 B+C show the enlarged lateral width. Table 2.6 presents the clinical fitting score results of this case. All CSM designs had an overall average or good fit (score = 3-4) with a slight overestimation on the medial side. The clinical fit of the bollard itself was not scored. As seen by the scores and the OR images, the 0.8-scaled CSM design with an additional 10 mm width, showed the best clinical fit (score = 4).

Bone CSM

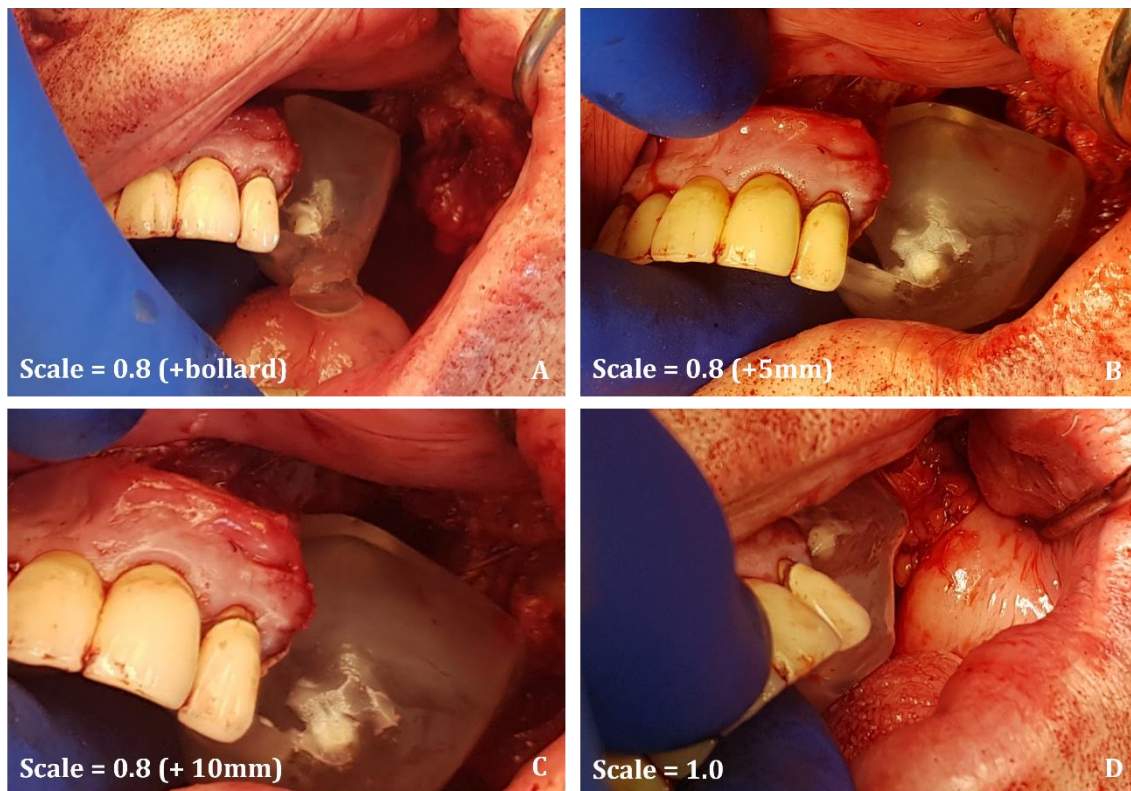


Figure 2.18. Image results of the clinical fitting of the digitally designed prostheses in patient nr. 4, directly after partial resection of the maxilla. The designs included a closed surface model (CSM) around the segmented resection bone in different scales and additional lateral width. **A)** CSM design scaled to 0.8. with a zygoma wiring bollard **B)** CSM design scaled to 0.8 and additional 5 mm width. **C)** CSM design scaled to 0.8 and additional 10 mm width **D)** CSM design scaled to 1.0.

Table 2.6 Clinical obturator fit in patient nr. 4 scored by prosthodontists.

Design	Poor 1	Bad 2	Average 3	Good 4	Excellent 5
A			X	X	
B			X	X	
C				X	
D			X		

A = Closed surface model (CSM), scale = 0.7; B = CSM, scale = 0.8; C = CSM, scale = 1.0; D = Hollow bulb.

2.3.4 Post-operative analysis

Figure 2.19 shows the difference between the putty obturator of P1 directly after surgery (T=0), and after 7 weeks (T=7) of refining and polishing during the post-operative visits. The intraoral scanned obturator of T0 is shown here in four views, the differences are visualized in colored coded distance maps. As seen by the figure, the obturator was mainly reduced at the lateral and posterior sides of the obturator for about 10 – 15 mm.

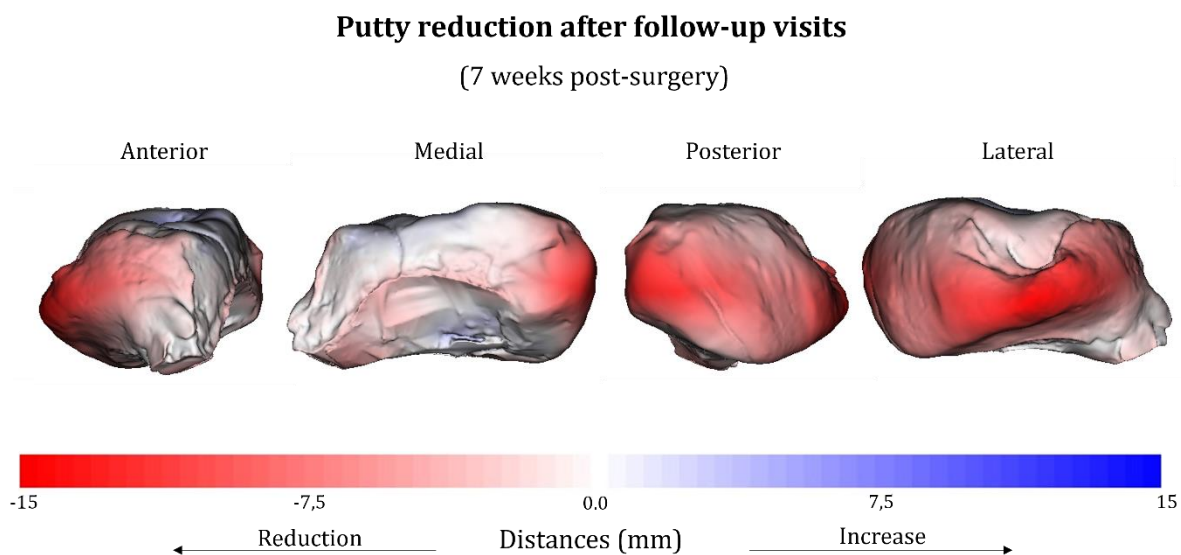


Figure 2.19. Color-coded distance maps of the obturator of case 1, directly after surgery, and after 7 weeks post-surgery in four directions. Note the amount of reduction at the lateral and posterior side of the obturator.

Figure 2.20 shows the results of the best-fitting CSM obturators scaled to 0.8 (yellow), with the registered intraoral scanned conventional ISOs as a transparent overlay. The figure shows the models in the superior view (upper panel) and lateral view (lower panel). There was no data available on patient 4, due to the patient's death.

As seen in Figure 2.20, P1 shows the largest and widest obturator compared to the other patients, in which the CSM shows an anterior overestimation and a posterior underestimation. P2 shows a wide conventional obturator across the septum midline, in which the CSM obturator exceeds the obturator in the posterior direction. P3 has the smallest conventional obturator volume, compared to the other patients. The CSM obturator of P3 shows the best fit inside the contours in the superior view, with an overestimation in the posterior-inferior direction, as shown in the lateral view of Figure 2.20.

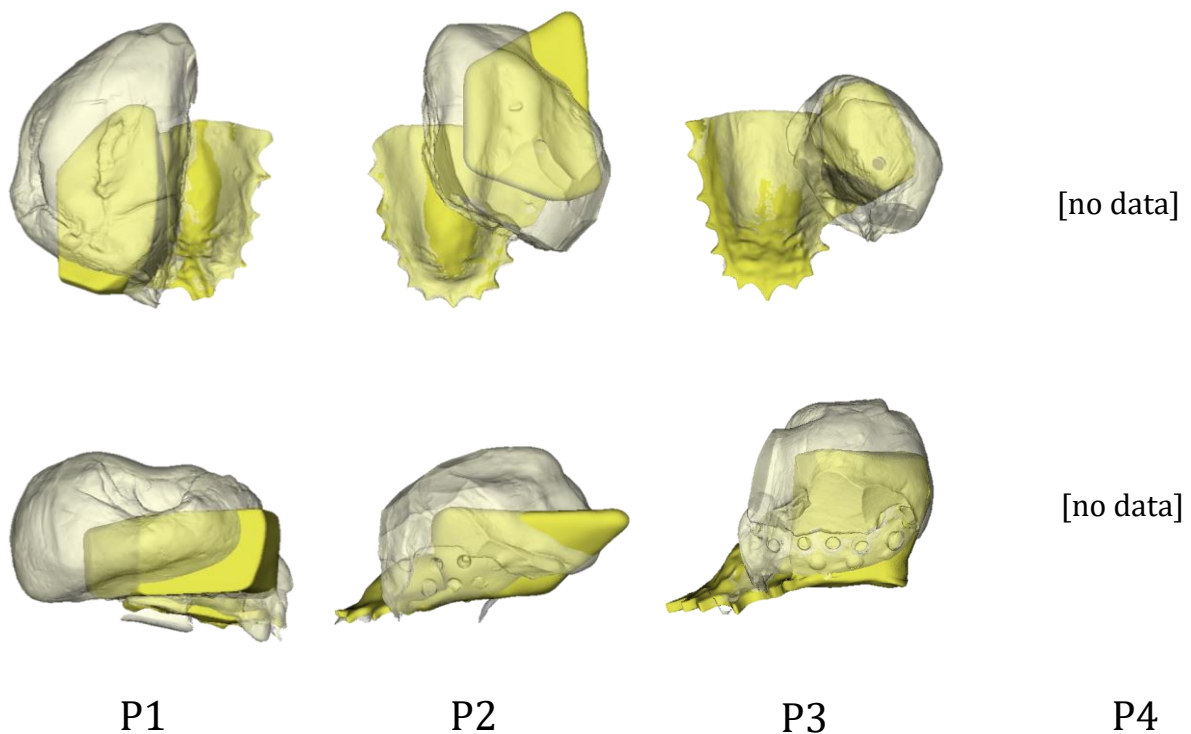


Figure 2.20. Digital closed surface model (CSM) obturators (yellow) with the registered intraoral scanned conventional putty obturator (transparent overlay) per patient (P). The upper panel visualizes the obturators in the superior view, and the lower panel in the lateral view.

2.3.5 Weight reductions

Table 2.7 sums the results of the putty IOS (T=0) and CSM volumes in Slicer and the calculated weight differences using the densities in Table 2.1. The results indicate a correlation between volume and absolute weight reduction. P1 shows the largest conventional weight and volume, and the highest absolute weight reduction. P3 shows the smallest conventional weight and volume, and the smallest absolute weight reduction. The weight percentages for all patients are around $\approx 36 - 39\%$.

Table 2.7 Volume and weight reduction results of each clinical case.

Patient No.	Volume IOS (cm ³)	Volume CSM (cm ³)	Volume TC (cm ³)	Weight IOS (g)	Weight CSM total (g)	Weight reduction (g)	Weight reduction (%)
1	49.97	6.45	37.31	71.46	45.11	26.35	36.87
2	31.11	5.31	21.20	45.92	32.11	18.33	39.92
3	14.06	3.06	8.40	20.10	12.06	8.04	39.99
4	-	-	-	-	-	-	-

CSM= Closed surface model; IOS = Intraoral scan of the conventional obturator.

2.4 Discussion

In this clinical trial study, we examined the shape and clinical fit of novel CAD/CAM 3D printed hollow ISOs in four maxillectomy patients, using intraoral scanning technology and CT to reduce the weight of conventional ISOs. We compared different CSM designs, in which the 0.8 scaled model around segmented resection margins showed the overall best clinical fit with a weight reduction between 36 – 39%.

2.4.1. Interpretation of results

The following section will discuss the different obturator designs for each case, starting with the first patient.

For the first patient, we included both skin and bone in the design to gain more obturator volume, because the conventional ISO is often larger than the defect to prevent sunken cheeks. The skin involvement resulted, however, in an anterior overestimation, exceeding the alveolar bone. Although the design was still considered clinically implementable by the prosthodontist, closing the mouth would be difficult and would look aesthetically unpleasant due to the tight skin around the lip. On the other hand, sufficient surrounding space was visible at the lateral and posterior sides. This result may be explained by the fact that the cheek is widened and thickened here compared to the anterior side. The 0.6 scaled CSM design had an overall volume underestimation and was, therefore, excluded from the designs in the other three patients.

For the second patient, more pre-operative time was available, which enabled more different designs. For a better assessment, we added the clinical scoring table. Based on the previous results, the CSM designs did not include soft tissue anterior to the resection bone. The bone CSM design without soft tissue involvement showed the best clinical fit, contrary to the expectations based on the wide obturator from the previous case. The reason is likely due to the less surgically removed teeth (3), which results in less space for the obturator to fit along the remaining teeth. A wide obturator would not pass the teeth, which explains why the bone CSM design had the best fit. Surprisingly, compared to the conventional ISO (Figure 18), the design had a noticeable posterior overestimation, but this did not affect the clinical fit. A possible explanation could be that the conventional ISO is naturally shaped by the surrounding soft tissue towards the medial side during placement. This shape characteristic is also visible in the other scans of Figure 18.

Moving on to how to consider the IOS obturator design of another research case, although the IOS design showed one of the higher scores, it would not be usable in patients with another resection type. Finally, the manual-designed obturator was not further used because it would not contribute to an optimized workflow. Besides, it had a lower clinical fitting score.

The third patient had the same type of resection (three molars, height of alveolar bone) as the second patient. The difference between them was the size of the palate involvement, which was significantly smaller for this case resulting in a small volume of putty compared to the previous two cases. Based on the results of the previous patient, we expected that bone CSM designs without including soft tissue would have the best clinical fit. Although the different CSM scales scored evenly (=4), the 1.0 scaled obturator had hardly any free surrounding space for additional relining material. As a result, it would not make post-operative volume adjustments possible. As seen from the obturator overlays (Figure 18), the CSM obturator exceeds the baseplate, which troubled the enclosing of the jaws. The posterior-inferior overestimation indicates the importance that the obturator needs to follow the natural shape of the palate parallel to the baseplate.

For the fourth patient, the previously studied hollow bulb was not considered, because it scored less well, as expected, in all three previous cases. The resection type was comparable to the first patient (molars – canine, the height of alveolar bone). Consequently, a wider obturator

shape was expected, and thus both the resection bone and soft tissue would initially be included in the design. The amount of CT scatter (Figure), however, made it challenging to distinguish the soft tissue during the segmentations. For this reason, soft tissue was not included, but the bone designs were enlarged instead at the lateral side to gain more volume. As expected, the enlarged volumes had the best clinical fit. Yet, none of the designs were excellent because of a tight fit against the nasal septum. Safety margins would have prevented this outcome.

One of the issues that emerged from these clinical findings is that the volume and width of the obturator highly depend on the resection type and the number of resected teeth. Furthermore, the post-operative weight calculation findings indicated a correlation between volume and absolute weight reduction. On the contrary, the weight reduction percentage was almost equal in all patients. The weight reduction never exceeded 40% due to the design limitations and the weight contribution of the resin and tissue conditioner. Nevertheless, this amount of weight reduction exceeded the maximum expected 33%, as stated by Dalkiz et al., 2018. Moreover, the post-operative findings showed a significant reduction in obturator size in the lateral and posterior direction (10 – 15 mm). This result indicated the need for scaling of the CAD/CAM design to allow the prosthodontist to alternate the design during the follow-up visits.

2.4.2 Strength and weaknesses

The study had multiple limitations. First, there were limitations regarding the population group. The research cohort is relatively small due to the low incidence of maxillectomy patients each year in the NKI-AVL. Another drawback was that the patient's comfort after the actual implementation of the obturator was not researched. Nevertheless, it should be considered that this was a *trial-and-error* clinical study, and a small patient cohort is often seen in similar clinical case studies in this field [1], [57]. On the other hand, despite this small cohort, this is the largest clinical trial cohort yet in this field to research CAD/CAM designed ISOs. This study alone gained much information about the shape and sizes of ISOs in general since it lacks in literature. Future collaborations with other hospitals could enlarge the cohort.

Second, there were limitations regarding the accuracy of the CT images involving the registration error. The PET-CT scan of patient 1 had a spacing between slices of 1.17 mm and a slice thickness of 2.0 mm, which affected the resolution of the segmentations. For this reason, it made it more difficult to find distinctive characteristics of the teeth, resulting in a higher RMS value. In addition, the scatter of the fourth patient also resulted in a higher RMS value due to the artificial teeth. On the other hand, the RMS of all patients was <1mm, which suggests that the FPR method is valid and would have had limited influence on the clinical fit. Another drawback that highly affects the clinical fit, was that the pre-and- postoperative resection margin variability was not measured. Yet, we assumed that using the virtual surgical planned Fusion ENT navigation system would have improved the clinical fit. Also, research has stated that this navigation system results in a higher accuracy of surgical procedures [58].

Third, the study had limitations regarding the precision of the resection margin contours. Only one observer defined these contours. Nevertheless, the shape of the CSM alters with the varying resection margins contours, and therefore the observer does not affect the clinical fit. Furthermore, there was an intra-observer variation by a learning curve in the design choices for each patient. The learning curve is an essential issue for future research. Additionally, there was an intra-observer variation in the clinical fit scoring of the obturators by the prosthodontist.

Fourth, the registration steps of the digital NKI-AVL workflow were limited to dentate patients. The registration steps can be alternated for edentate patients. For example, the study of Deferm et al. (2022) used a soft tissue-based registration algorithm to register IOS and CT scans [59]. However, a drawback of this algorithm is the need for a high-resolution (CB)CT scan. Another solution for the future inclusion of edentate patients could be with registered marker points on dentures while scanning. Furthermore, the digital NKI-AVL workflow is not fully automated yet, despite the fewer (manual) steps. For instance, the encoded Slicer steps (Appendix B1 and B2)

could be integrated into a user interface. For reproductive purposes, the protocols of Appendix A1 and A2 should provide additional clarity for future (non-technical) users.

Finally, the different scales used for the CSM design were based on trial-and-error and thus not according to the literature. Previous studies in this field only focused on the clinical fit immediately at surgery and did not take the post-operative adjustments of the ISO into account. For example, the study by Kortjes et al. (2018) researched a 3D ISO for a clinical case based on CT and MRI. They re-printed a new interim obturator for the first follow-up visit, which is not time and cost-effective [1]. In addition, compared to their innovative method, in which they used the tumor contour verification (and its margins) for the obturator design, the current CSM workflow seems faster, easier, and more automated.

2.4.3. Future recommendations

Several questions remain unanswered at present. The patient's comfort after implementing the digital hollow-designed ISOs should be researched in future, larger cohort, clinical studies. It is recommended to implement the conventional ISO for the control group. In addition, we suggest a study that focuses on the impact of weight reduction differences experienced by a patient at different CAD/CAM design scales (e.g., 0.7, 0.8). The importance lies in the patient's comfort rather than researching the exact shape or scale of the obturator design. Also, the feasibility of small maxillary defects regarding the patient's comfort, time, and cost-effectiveness of obturators, should be researched.

Further work is required to establish the final clinical implementation. The baseplate needs holes for the teeth retention wires together with a well-designed boulder for larger type defects. In addition, to gain retention and stability in large complex maxillary defects, a 3D zygomatic implant-supported prosthesis could be considered in future designs [60]. Furthermore, investigating the safety margins, especially for the nasal septum and the lower jaw movements, is important to improve the clinical fit in future research. In addition, enlarging the CSM obturator in the lateral direction could be a solution for CTs with scatter or larger (>1mm) slice thickness. Also, this design choice could be an improved substitute for the CSM model around the bone and soft tissue, which should be researched.

In terms of the digital workflow, creating a (partly) automated user interface would ease the steps for (non-technical) users. Finally, future research should also measure the pre-and postoperative resection margin variability using the in-house Fusion ENT navigation system. Future research should also consider using a more advanced type of surgical navigation to reduce the variability or may use surgically navigated cutting guides.

2.5 Conclusion

The purpose of the current clinical-trial study was to evaluate the digital hollow CSM design and to improve the existing NKI-AVL concept CAD/CAM workflow.

Taken together, our findings suggested a promising prospect for using this automatic CSM approach when comparing the existing hollow bulb obturator design. Based on the results, it is expected that a CSM scale around 0.8 could be a good balance between obtaining weight reduction, clinical fit, and post-operative usability. Furthermore, these findings may help us to understand how the resection type influences the shape and, therefore, the clinical fit of the ISO. We thus recommend predicting the obturator shape based on the resection margins in future research.

Further improvement of the baseplate design is required for clinical implementation of the digital ISO workflow by including retention wire holes and a boulder. In addition, the workflow should be more automated and include safety margins in the obturator design.

3. Retrospective study: verification of the CSM obturator

3.1. Introduction

A clinically relevant finding of the study described in chapter 2 was that the shape of the ISO varies and highly depends on the maxillary defect. The varying obturators make it difficult to predict and design the final CAD/CAM shape. Compared to literature, no research on obturator shapes has been reported yet, to our knowledge. Nevertheless, many maxillectomy classification systems exist, such as Brown's (see chapter 1.8). These classification systems, however, are used for maxillectomy planning and do not provide knowledge about obturator shapes. Although those classification systems can provide guidance, the shape of the ISO is determined by more factors than the bony resection alone. From our clinical experience, the ISO is shaped and supported by surrounding hard- and soft tissue and depends on the resection height and number of resected teeth. For example, as indicated in the previous clinical study, resecting the canines is an important factor in whether the obturator is enlarged at the lateral side. Consequently, this obturator variation depending on resection type needs to be considered in future CSM designs. To obtain a supporting tool to classify and predict the surgical obturator shape to standardize the CSM designs, and to gain a more user-friendly workflow, we developed a novel classification system.

The classification system is called: the Ooms' ISO classification system based on the maxillary defect. The classification system is based on our clinical experiences, and expert knowledge, and is inspired by existing maxillary classification systems. The following paragraphs explain which factors contribute to the shape of the ISO, separated into horizontal and vertical components.

3.1.1. Horizontal components

From an axial point of view, the shape of the ISO can be divided into four components, which are schematically shown in Figure 3.2. The first component (red), the medial side, is the preoperatively determined palatal resection margin perpendicular to the nasal septum. The remaining part of the palate and the nasal structures, such as the septum, concha, and cartilage, cause a straight vertical line at the medial side of the ISO. The second component is the oblique preoperatively determined palatal resection margin, directed to the most anterior resected tooth.

The third component points to the lateral direction. The size and angle depend on the vertical resected location on the basal arch of the maxilla. This component is shaped by surrounding soft tissue such as the cheek and therefore follows its anatomical direction. A large defect allows vertical and wide horizontal expansion of the ISO, resulting in increased pressure against the cheek. The third component tends to be significantly narrower in small posterior defects where for example only the molars are resected. The narrow shape is also due to the essential point that a large ISO will not fit through the mouth in this example. Figure 3.1 highlights the comparison of the second and third components of two intraoral scanned ISOs, along with a schematically drawing of teeth. In the case of the narrow obturator (yellow), only the molars are

resected, while in the wide obturator (purple), the resection also includes the premolars and the canine.

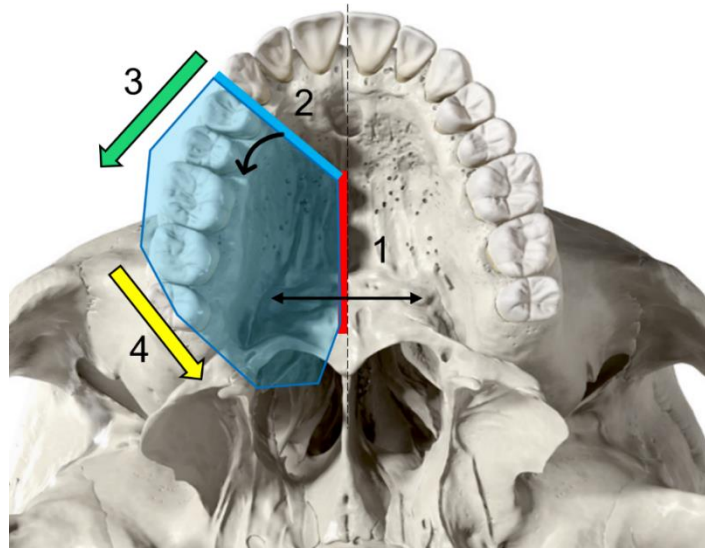


Figure 3.2. The four horizontal direction components of the immediate surgical obturator. **1)** Vertical resection component. **2)** Oblique resection component. **3)** Lateral component following the direction of the cheek. **4)** Medial component shaped by the buccal and masticator space.

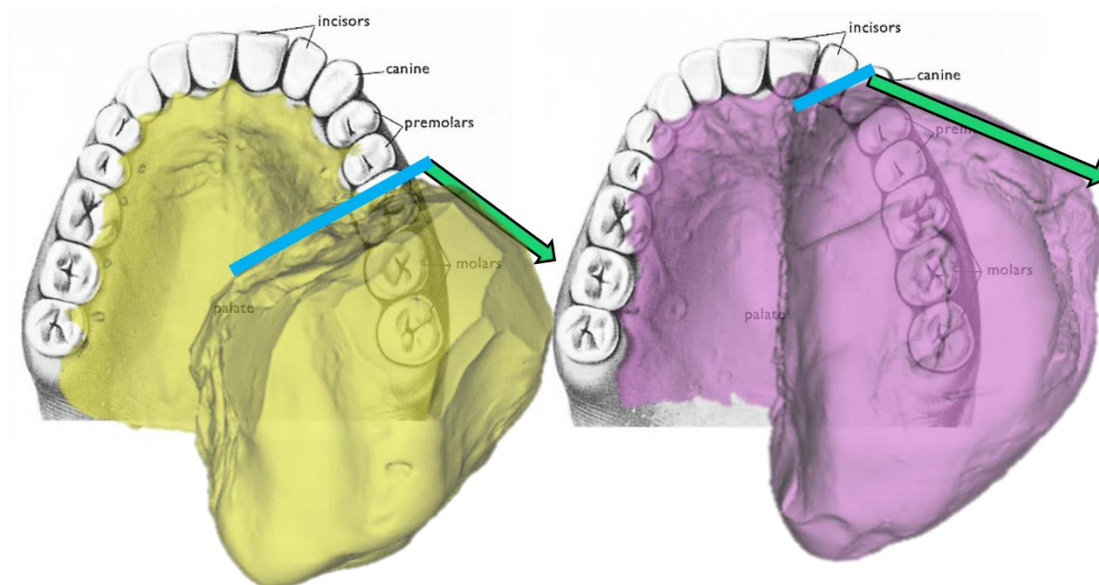


Figure 3.1. Comparison of two intraoral scanned immediate surgical obturators (ISO's) with the direction of the ISO's pointed out by the oblique surgical resection margin (blue line) and its lateral outer direction (green arrow). Note that in case of the purple ISO, three more teeth are resected and therefore the green direction arrow is wider and larger.

Finally, the fourth component follows a medial direction due to the surrounding soft tissue (see yellow arrow Figure 3.1). To illustrate these surrounding structures, Figure 3.3 shows two axial MRI slices of the upper jaw with highlighted soft tissue spaces. An essential structure, for example, is the buccal space (orange) which contains the buccal fat pad (BFP), also-called Bichat's fat pad. The BFP consists of the main body located at the posterior maxilla with four extension lobes. The contour of the cheeks is mainly determined by the buccal extension of the BFP. Recently, the BFP is occasionally used to enclose postsurgical maxillary defects [61]. Another important

surrounding structure is the masticator space (green), which includes the mastication muscles and the posterior mandible [62].

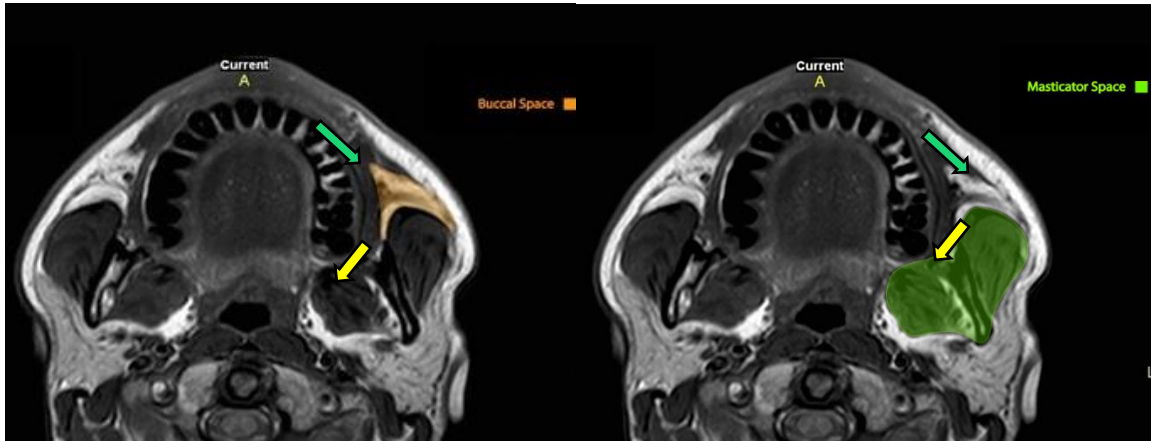


Figure 3.3. MRI slices of the upper jaw (axial view) with highlighted surrounding soft tissue: buccal space (orange) and masticator space (green). The lateral and medial directions of the immediate surgical obturator are marked by a green and yellow arrow, respectively.

3.1.2. Vertical components

Besides the horizontal components, the size and shape of the ISO depends on the height of the resection. Table 3.1 and Figure 3.4 present the cephalometric landmarks contributing to the classification system [63], [64].

Table 3.1 List of anatomical landmarks in the maxillofacial region.

Landmarks	Definition
Canine eminence (Ce)	Maxilla surface point corresponding to the canine root apex
Zygomaxillare (Zm)	Most inferior point of the zygomaticomaxillary suture
Zygoorbitale (Zo)	Most superior point of the zygomaticomaxillary suture

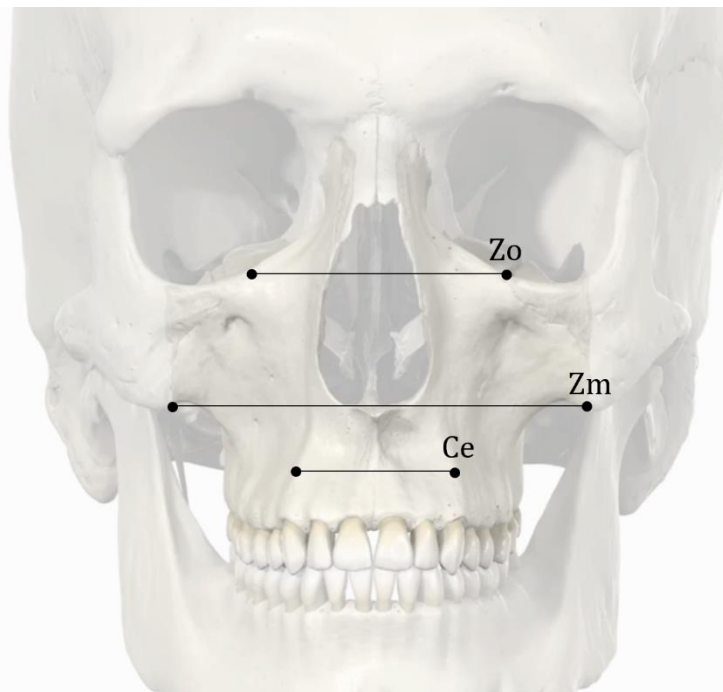


Figure 3.4: The maxillary cephalometric landmarks of the Ooms’ classification system in anterior view.

The zygoma arch is an essential factor because it mainly shapes the facial structure and aesthetics, in which the ISO replaces these important bone structures. For this reason, it is necessary to divide whether the resection involves the alveolar bone or exceeds the Zygomaxillare (Zm), with its maximum to the orbital floor (Zo). Alongside the maxillary heights, the figure shows another landmark, the canine eminence (Ce). This landmark separates the anterior (incisors) and posterior (molars) maxillary arch. The Ce landmark is used as a border for the classification system to state whether the conventional obturator expands horizontally to the cheeks as explained in the previous section.

3.1.3. Classification system

Based on the previously explained horizontal and vertical components, Figure 3.5 illustrates the seven categories of the Ooms' ISO classification for unilateral maxillectomy resections. The system defines whether the horizontal resection is below or above the Zm landmark, which is defined here as alveolar (A) and zygoma (Z) respectively. The vertical axes define if the resection is medial (I), intersects (II), or is lateral to the Ce landmark (III). The fourth vertical category (IV) involves the resection of the whole unilateral maxilla. Examples of classified conventional ISOs used to develop the classification system are visualized in Appendix E

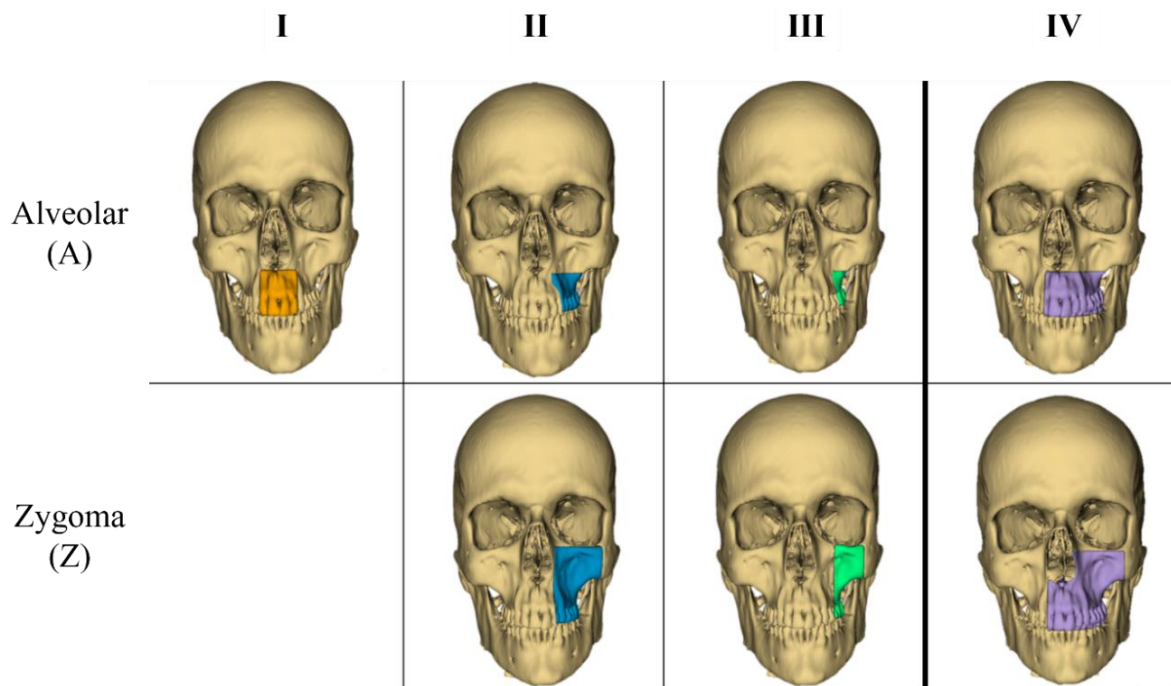


Figure 3.5. Ooms' immediate surgical obturator classification system based on the unilateral maxillary defect. Each class is horizontally divided into the height of the resection: alveolar (A) and or zygoma (Z). Vertically, the classes are divided into the frontal arch (I), and whether the canine eminence is resected (II) or not (III). The fourth category (IV) involves the resection of the whole unilateral maxilla.

Table 3.2 explains how the resection margins affect the shape of the CAD/CAM obturator design and whether soft tissue is involved besides the segmented bone. For a visualized perspective, see Appendix F.

Table 3.2. Ooms' immediate surgical obturator classification.

Alveolar	
Class I	The horizontal maxillary resection involves the alveolar bone, and the vertical resection is located medial from the canine eminences. The obturator remains small and never exceeds the bony resection margins because of the tight skin around the lip. Therefore, only the resection bone is considered in the ISO design. The maximum height is limited to the nasal spine.
Class II	Maxilla resection involves the alveolar bone horizontally and intersects the canine eminence vertically. The resection results in additional space for a wide-shaped ISO. The obturator exceeds the bony resection margins mainly at the lateral side, adding more pressure to the surrounding soft tissue. Therefore, both the resection bones and the m. Buccinator are considered in the ISO design. The height of the ISO is limited to the horizontal resection margin.
Class III	The horizontal maxillary resection involves the alveolar bone, and the vertical resection is located lateral from the canine eminences. The obturator consequently remains narrow, slightly exceeding the bony resection margins. Therefore, only the resection bone is considered in the ISO design. The height of the ISO is limited to the horizontal resection margin.
Class IV	The horizontal maxillary resection involves the alveolar bone, and the vertical resection is located both medial and lateral from the canine eminences. The resection results in a combination of classes A-I and A-II.
Zygoma	
Class II	The horizontal maxillary resection involves the alveolar bone and exceeds the inferior zygomaxillare suture. The vertical resection intersects the canine eminence. The large width and height of the resection, result in a tall and wide ISO, finding its support in the cheeks. Therefore, both the resection bone and the buccal fat pad are considered in the ISO design. The height is limited to the horizontal resection with its maximum at the orbital floor.
Class III	The horizontal maxillary resection involves the alveolar bone and exceeds the inferior zygomaxillare suture. The vertical resection is located laterally from the canine eminence. The ISO is narrow and tall, slightly exceeding the contours of the bony resection. Therefore, only the resection bone is considered in the ISO design. The height is limited to the horizontal resection with its maximum at the orbital floor.
Class IV	The horizontal maxillary resection involves the alveolar bone and exceeds the inferior zygomaxillare suture. The vertical resection is located both medial and lateral from the canine eminences. Therefore, the design results in a combination of classes A-I and Z-II.

3.1.4. Study aim

This research is a retrospective study that aims to validate the CSM design based on the Ooms' ISO classification system. It is thus expected that the CSM design needs to be enlarged around surrounding soft tissue for classes A-II, A-IV, Z-II, and Z-IV according to Table 3.2. These statements will be validated by comparing the shape, volume, and weight reduction of the CSM designs with segmented conventional ISOs from post-operative CT scans.

3.2. Methods

3.2.1. Patients

The retrospective study included patients who underwent a maxillectomy between 2009 – and 2020 in the AVL – NKI hospital. The criteria included that both a pre-and postoperative CT scan were available for each patient. In addition, the conventional bulb could be distinguished in grayscale and therefore segmented from the postoperative CT scan. This inclusion left 17 patients who were enrolled in the study (Figure 3.6).

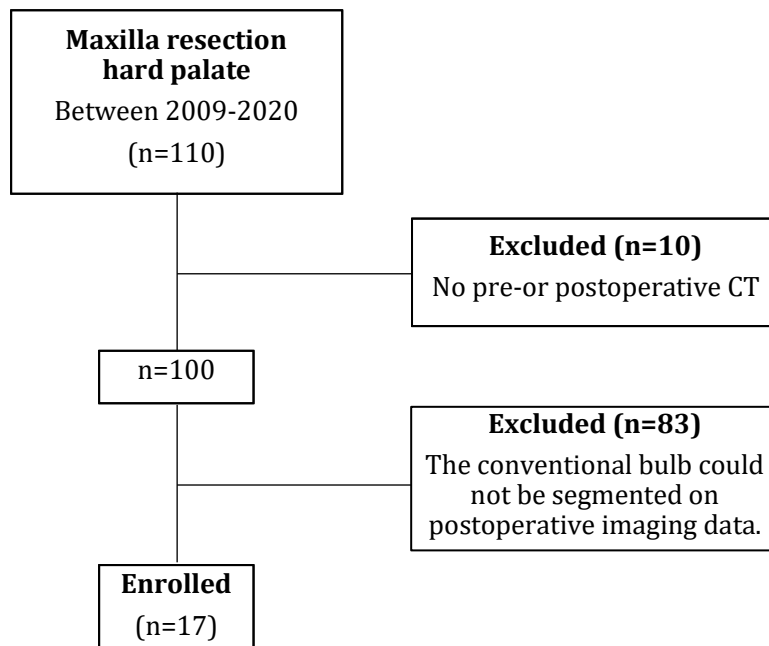


Figure 3.6. Inclusion criteria for maxillectomy patients in the Antoni van Leeuwenhoek hospital – National Cancer Institute.

3.2.2. CT analyses

Patients underwent CT scanning with a reconstructed slice thickness of 0.5–5.0 mm. All CT scans were made at the NKI-AVL using the same CT scanner and settings. All scans were performed with 120 kVp and exposure 18–300 mA. The field of view was 512x512 pixels and pixel spacing varied between 0.24 × 0.24 mm and 1.17 × 1.17 mm. The CT dose index (CTDI_{vol}) was 1.97–29.39 mGy and the dose length product was 70–1039 mGy*cm.

3.2.3. Technical analysis

The open-source software Slicer was used for semi-automatic greyscale thresholding of the skulls. The maxillary resection margins were obtained by registration (FPR) and subtraction of the segmented post- and pre-operative skulls (Figure 3.7). The conventional obturator was segmented from the postoperative scan.

All the resection margins were classified using the Ooms' classification system. The bilateral cases were considered as class A-IV or Z-IV. The CAD/CAM CSM obturators were automatically designed from the maxillary pre-operative resection margins using the Slicer extension 'Markups to Model' (see Figure 2.2). For Ooms' classification classes A-II, A-IV, Z-II, and Z-IV, additional 3D models were designed from both the resection margins and the surrounding soft tissue. This resulted in 3D-designed '*bone CSMs*' and '*bone & soft tissue CSMs*'.

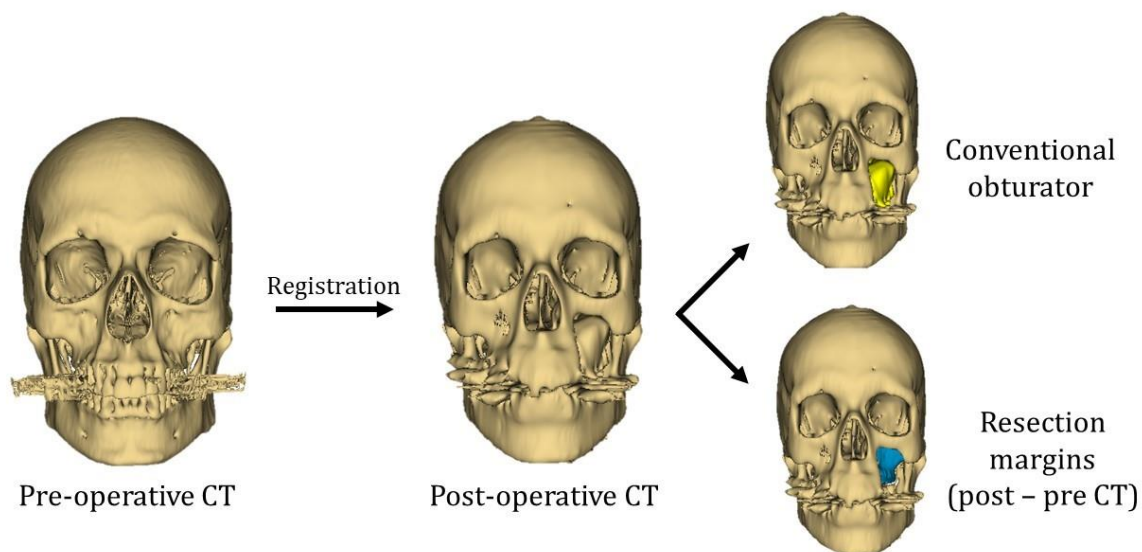


Figure 3.7. Workflow to obtain the segmented conventional obturator and resection margins. First, the pre-operative CT is registered to the post-operative CT. Next the conventional obturator is segmented from the post-operative scan, and the resection margins are obtained by subtraction of the skulls.

Both the CSMs and conventional ISOs (Figure 3.8 A) were then exported and saved as a STL file format. The STL models were imported into the open-source-3D-modeling software Meshmixer. The CSM designs were scaled to 0.8, based on the clinical results of Chapter 2, and made hollow with a 2mm thick edge of Clear resin. On top of the Clear resin, an outer layer of TC was considered (Figure 3.8 B).

Two additional theoretical reference obturators were designed, by transforming the solid conventional obturator (Figure 3.8 A) into a hollow model with a 2mm thick edge Clear resin. The first reference model, without an outer layer of TC, was referred to as the Theoretical Maximum Reference (TMR) (Figure 3.8 C). For a more clinically feasible comparison, the second reference model was scaled to 0.8 to contain an additional layer of TC, referred to as the Theoretical Clinical Reference (TCR) (Figure 3.8 D). The different hollow obturator volumes (Figure 3.8 B-D) were compared to the conventional solid putty obturator volumes (Figure 3.8 A).

The weights (W) of the digital obturators were calculated by obtaining the digital volumes (V) in Slicer, multiplied by the density (ρ) of the denture reline (putty and TC) materials and Clear resin. The absolute and percentage weight reductions of the TMR, TCR, and CSM design, compared to the segmented conventional obturator, were calculated according to the methods described in Chapter 2.2.7.

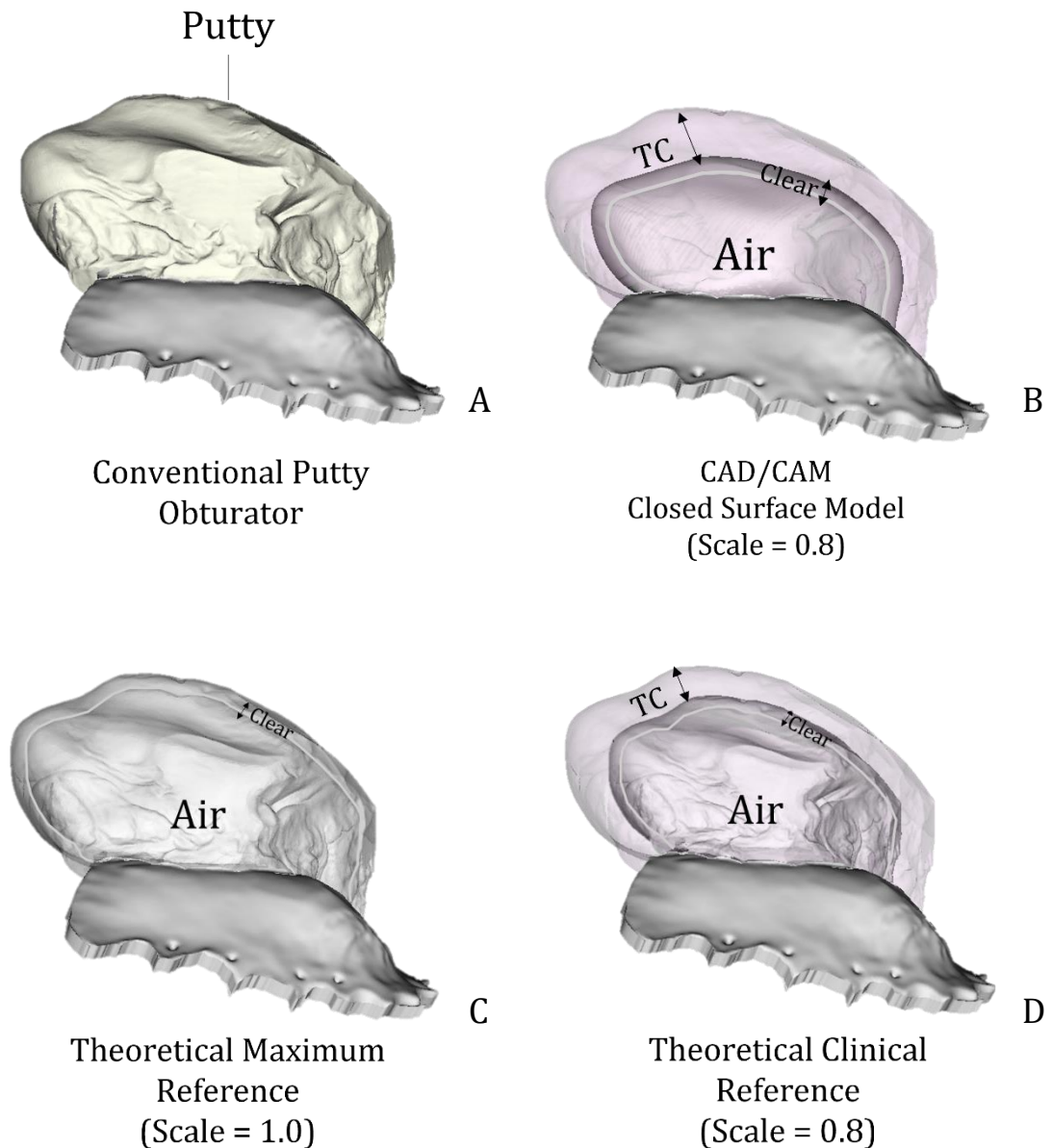


Figure 3.8. Schematic overview of the different obturator designs. **A)** Conventional putty obturator. **B)** Computer aided- and designed (CAD/CAM) closed surface model (CSM) design, scaled to 0.8 with a layer of tissue conditioner (TC). **C)** Theoretical Maximum Reference: hollow 2mm thick Clear resin conventional obturator. **D)** Theoretical Clinical Reference: hollow 2mm thick Clear resin conventional obturator scaled to 0.8, with a layer of TC.

The shape and volume comparison between the conventional obturator and CSM design was assessed in Slicer by one of the most used overlap-based segmentation metrics: the Hausdorff Distance (HD) [65]. The HD calculates the largest distance (d) between point set X (CSM obturator) to Y (conventional obturator) as schematically visualized in Figure 3.9 [66]. Furthermore, the 95th percentile (95%) HD was calculated, which is the maximum HD without outliers. In addition, the average HD was calculated, which takes the average of all distances (d) between the point sets [67]. For an additional virtual comparison, the distances from the CSM design to the conventional ISO (d_{xy}) were saved as colored-coded distance maps and projected on the conventional ISOs.

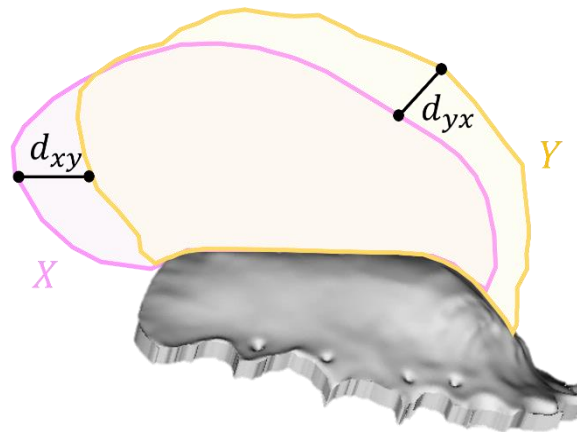


Figure 3.9. Schematic overview of the Hausdorff Distance [66].

3.2.4. Statistical methods

Descriptive statistical analyses were performed using IBM SPSS version 28 (IBM Corp., Armonk, NY, USA). These analyses included correlation calculations between weight reduction and volume using Pearson's product-moment correlation coefficient (r) for a significant p -value <0.01 . In addition, boxplots were made to summarize the minimum, maximum, mean values, and standard deviations of the HDs and obturator volumes.

3.3. Results

3.3.1 Patients

Baseline characteristics for the seventeen included patients are shown in Table 3.3.

Table 3.3. Baseline parameters of included patients.

Case No.	Ooms' class	Type of tumor	Tumor stage	Site of tumor	Bilateral resection	Time post-operative scan after surgery (days)
1	Z-III	OM	cT4N0M0	Left	No	4
2	Z-IV	SCC	cT4N0M0	Left	No	63
3	A-III	AdCC	cT4N0M0	Left	No	27
4	Z-II	SCC	cT4N0M0	Right	No	92
5	Z-IV	SCC	cT3N0Mx	Left	No	46
6	Z-IV	SCC	cT4N0Mx	Left	No	31
7	A-III	SCC	cT4N0M0	Right	No	273
8	Z-II	SCC	cT4N0M0	Right	No	43
9	Z-II	SCC	cT4N0M0	Left	No	32
10	Z-IV	AdCC	cT2N0M0	Left	No	78
11	A-IV	SCC	cT4N0M0	Right	No	75
12	Z-IV	SCC	cT4N0M0	Right	No	25
13	Z-IV	SCC	cT4N0M0	Right	No	72
14	Z-IV	SCC	cT4N0M0	Left	No	28
15	A-IV	AdCC	cT4N0M0	Right	Yes	50
16	Z-IV	SCC	cT4N0M0	Left	Yes	25
17	A-II	SCC	cT4N0M0	Right	No	31

SCC = Squamous cell carcinoma; AdCC = Adenoid cystic carcinoma; OM = Odontogenic mycoma.

Table 3.4 presents a summary of the number of patients with a designed '*bone CSM*' and with an additional '*bone & soft tissue CSM*'. The table is also divided by uni- and lateral resection margins.

Table 3.4. Summary of the number of patients per CSM type.

Definition	Number
Uni- and bilateral bone CSM	17
Uni- and bilateral bone- and soft tissue CSM	11
Unilateral bone CSM	15
Unilateral bone- and soft tissue CSM	9

CSM = Closed Surface Model.

3.3.2 Weight reduction

Table 3.5 presents the summary of the weight reduction results of the TMR, TCR, and bone CSM obturator, compared to segmented conventional obturators of seventeen uni- and bilateral cases. The direct comparison is shown in Table G1 of Appendix G. The weight reduction values include the minimum, maximum, mean values, and standard deviations. This table shows that the highest weight reduction is achieved by the TMR obturator, with an absolute reduction of 60g and a percentage reduction of 69%. The TCR and CSM both have a mean absolute reduction of 40g and percentage reduction of 47%.

Table 3.5. Summary of the weight reduction results, presenting minimum (min), maximum (max), mean (μ) values, and standard deviations (σ) for n=17.

	TMR		TCR		CSM	
	Weight reduction (g)	Weight reduction (%)	Weight reduction (g)	Weight reduction (%)	Weight reduction (g)	Weight reduction (%)
Min	28.8	55.5	19.4	37.1	15.7	34.5
Max	207.2	82.3	137.4	54.6	99.2	59.9
$\mu \pm \sigma$	60.4 \pm 43.1	69.7 \pm 6.9	40.3 \pm 28.6	46.6 \pm 4.6	39.6 \pm 21.8	47.0 \pm 6.5

TMR = Theoretical Maximum Reference; TCR = Theoretical Clinical Reference; CSM = Closed Surface Model.

Table 3.6 shows similar weight reduction results as Table 3.5, without the two bilateral cases (n=15). Compared to Table 3.5, this table shows that the minimum values are identical and the maximum absolute weight reduction values are lower. The mean weight reduction percentages differ $\leq 1\%$.

Table 3.6. Summary of the weight reduction results, presenting minimum (min), maximum (max), mean (μ) values, and standard deviations (σ) for n=15.

	TMR		TCR		CSM	
	Weight reduction (g)	Weight reduction (%)	Weight reduction (g)	Weight reduction (%)	Weight reduction (g)	Weight reduction (%)
Min	28.8	55.5	19.4	37.1	15.7	34.5
Max	87.4	76.0	58.2	50.8	59.9	59.9
$\mu \pm \sigma$	48.4 \pm 18.7	68.7 \pm 6.5	32.4 \pm 12.4	45.9 \pm 4.4	34.3 \pm 15.1	47.6 \pm 6.6

TMR = Theoretical Maximum Reference; TCR = Theoretical Clinical Reference; CSM = Closed Surface Model.

Figure 3.10 shows the correlation between the weight reduction and different volume scales of the CSM obturator (i.e., the higher the scale, the less use of tissue conditioner) of patient number 1. Both graphs show that the weight reduction is exponentially growing for increasing volume scales. The maximum weight reduction percentage, the TMR, is 70%.

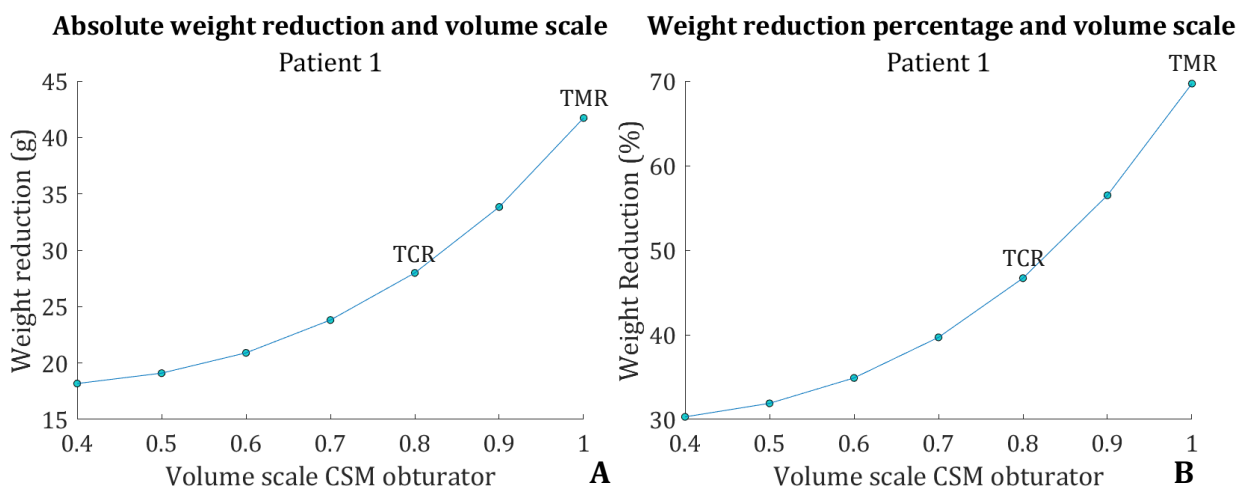


Figure 3.10. Correlation between the 2mm Clear resin volume scale of the closed surface model (CSM) obturator and weight reduction of one clinical case. **A)** The absolute weight reduction. **B)** The weight reduction percentage.

Figure 3.11 shows the Pearson's correlation results between the absolute weight reduction and conventional obturator volume for (A) seventeen uni-and bilateral and (B) fifteen unilateral cases. The plots show the TMR (blue), TCR (yellow), and CSM (red) obturator. All the correlation plots show a strong relationship and are statistically significant for $p < .001$. As seen from the graphs, all directions are positive (i.e., a greater volume is associated with greater weight reduction). What stands out in Figure 3.11 A is the outlier, which has the largest volume and weight reduction for all three plots. Furthermore, Figure 3.11 shows that the values of the TCR and CSM obturators are more similar compared to the TMR, which has the overall highest weight reduction values.

Figure 3.12 shows similar correlation plots as Figure 3.11, presenting the Pearson's correlation results between the weight reduction percentages and conventional obturator volumes. All the correlation plots show a weak Pearson's relation and are not significant. The plots are in a horizontal direction, all TMR values are around 70% and are 40-50 % for the TCR and CSM. Similarly, as Figure 3.11, the bilateral cases resulted in outliers and were excluded for the remaining figures of this section.

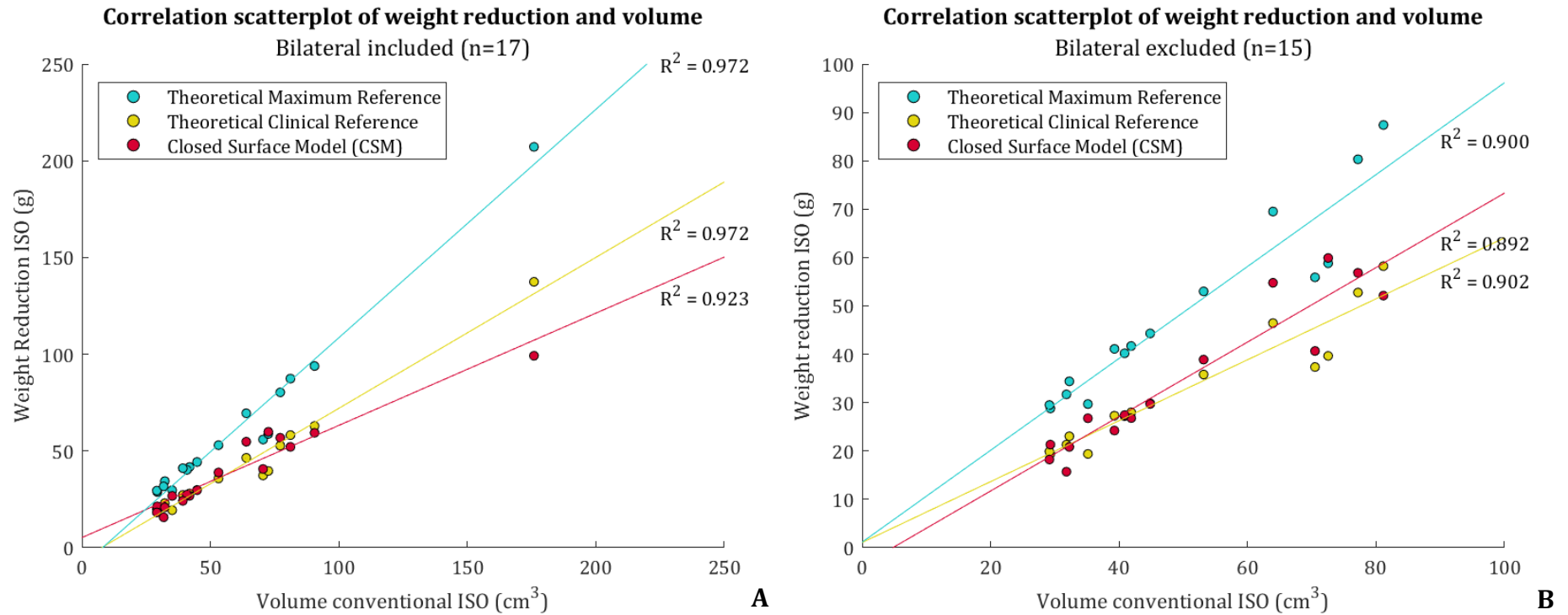


Figure 3.11. Pearson's correlation scatterplots of the segmented conventional obturator volume and absolute weight reduction seventeen uni- and bilateral **(A)** and fifteen unilateral **(B)** obturators. The plots present the differences between the computer-aided and designed (CAD/CAM) closed surface model (CSM) obturator, the theoretical maximum reference: conventional volume (hollow), and the clinical reference: 0.8 scaled conventional volume (hollow) with a layer of TC. Note the outlier differences between the two graphs and the similar positive trend of the different variables.

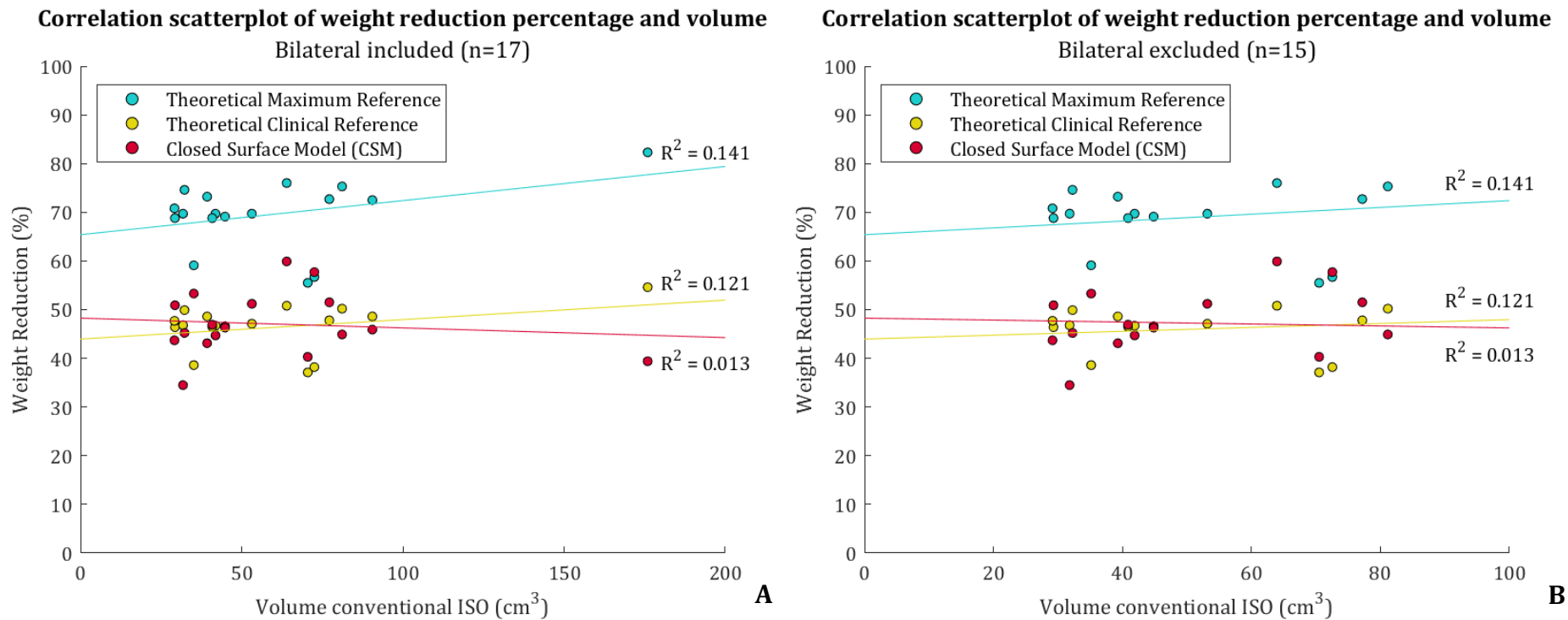


Figure 3.12. Pearson’s correlation scatterplots of the segmented conventional obturator volume and weight reduction percentage of seventeen uni- and bilateral **(A)** and fifteen unilateral **(B)** obturators. The plots present the differences between the computer-aided and designed (CAD/CAM) closed surface model (CSM) obturator, the theoretical maximum reference: conventional volume (hollow), and the clinical reference: 0.8 scaled conventional volume (hollow) with a layer of TC. Note the maximum weight reduction around 70% and the other designs around 40-50%.

3.3.3 Shape & volume comparison

Table 3.7 presents the summary of the obturator volumes and the HDs between the fifteen unilateral conventional obturators and the 0.8 scaled bone-CSM designs. The direct comparison is shown in Figure G2 (Appendix G). As seen from the table, the minimum and maximum volumes of the CSM obturators are significantly less than the conventional obturators. The average HD is about 2 mm, which is considered to be the average overestimation. The maximum 95% HD value is around 9 mm, which is about twice as small as the maximum HD (16 mm) since it includes outliers. The minimum HD values are 0 mm, which indicates there are CSM designs without a shape overestimation.

Table 3.7. Summary of the obturator volumes and Hausdorff Distances, presenting minimum (min), maximum (max), mean (μ) values, and standard deviation (σ) for n=15.

	Obturator volumes (cm ³)		Conventional vs. CSM 0.8 (mm)		
	Conventional	Bone-CSM	HD Maximum	HD Average	HD 95 th percentile
Min	29.1	5.5	0	0	0
Max	81.1	45.2	16.2	1.8	8.7
$\mu \pm \sigma$	49.5 \pm 18.6	22.6 \pm 11.6	7.9 \pm 4.5	0.6 \pm 0.5	3.5 \pm 2.6

HD: Hausdorff Distance; CSM = Closed Surface Model.

Table 3.8 presents the summary of the obturator volumes and the HDs between the nine unilateral conventional obturators and the 0.8 scaled bone and soft tissue-CSM designs. The direct comparison is shown in Figure G3 (Appendix G). Compared to the results of Table 3.7, the bone & soft tissue-CSM designs had a larger shape overestimation, which is seen especially in the average HD values in this table. In addition, none of the minima are equal to zero, indicating that every CSM design shape is overestimated.

Table 3.8. Summary of the obturator volumes and Hausdorff Distances, presenting minimum (min), maximum (max), mean (μ) values, and standard deviation (σ) for n=9.

	Obturator volumes (cm ³)		Conventional vs. CSM 0.8 (mm)		
	Conventional	Bone & soft tissue-CSM	HD Maximum	HD Average	HD 95 th percentile
Min	29.3	22.0	12.0	0.9	5.1
Max	81.1	61.0	17.5	2.8	9.9
$\mu \pm \sigma$	58.3 \pm 19.3	42.1 \pm 13.8	15.0 \pm 1.8	1.8 \pm 0.6	8.1 \pm 1.6

HD: Hausdorff Distance; CSM = Closed Surface Model.

Figure 3.14 shows the boxplots of the HD results from Table 3.7 and Table 3.8 respectively. As seen by the plots, the maximum (95 %) HD values have a wider range in the *bone-CSM* compared to the *bone & soft tissue-CSM*. All mean HD values of the boxplots in Figure 3.14 B are larger compared to Figure 3.14 A.

Figure 3.13 compares the conventional obturator volumes of each Ooms' classification class. Figure 3.13 A compares the alveolar and zygoma classes, and Figure 3.13 B compares all classes. As seen in the Figure, the mean volumes of the zygoma classes are larger than the alveolar classes. Class Z-IV has the highest mean volume and A-II has the lowest. The research cohort consists of only one case for the classes A-II, A-IV, and Z-III, and none of the cases are A-I.

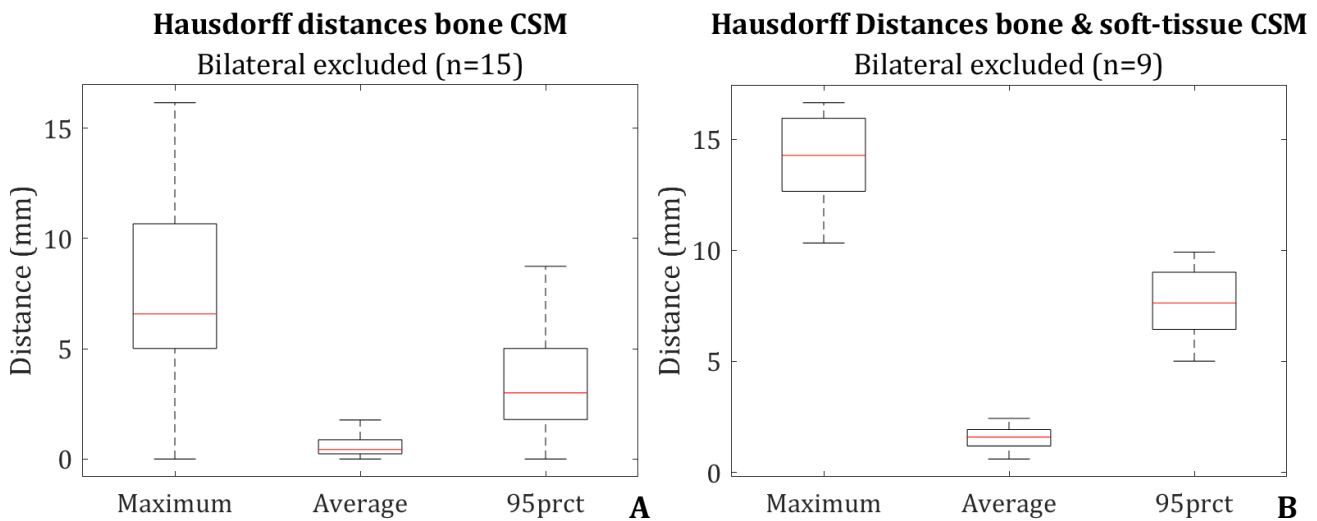


Figure 3.14. Boxplots of the maximum, average, and maximum 95th percentile Hausdorff Distances (HD) between the unilateral conventional obturator and the closed surface model (CSM) designs. **A)** Bone-CSM designs. **B)** Bone & soft tissue- CSM designs. Note that the mean HD values are higher in the right panel (**B**) compared to the left panel (**A**).

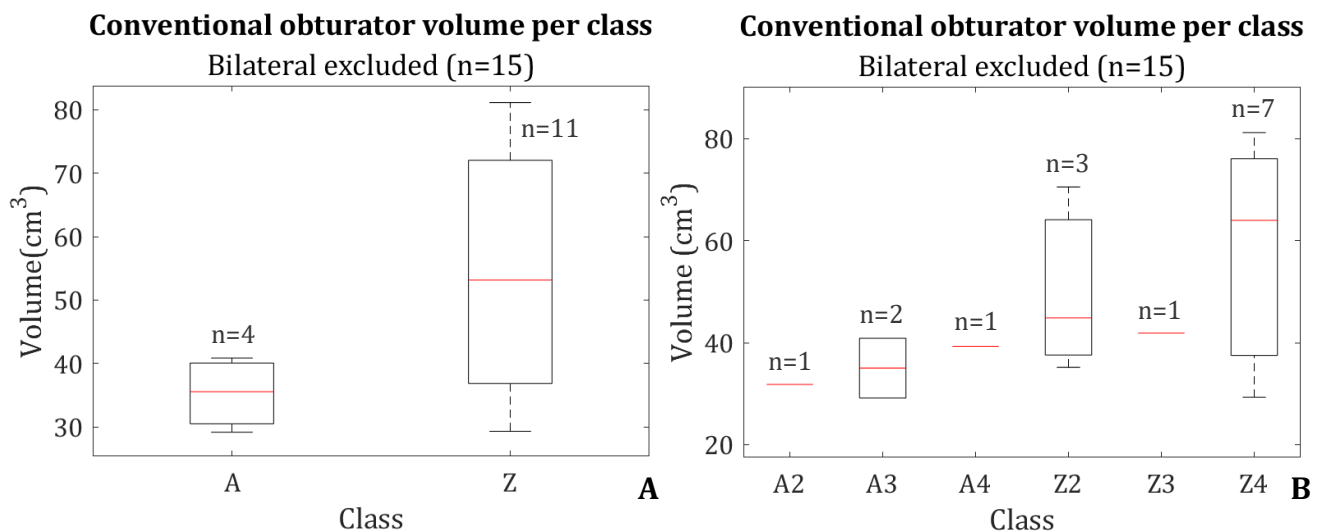


Figure 3.13. Comparison of the volumes of the unilateral conventional obturators per class of the Ooms' classification system. **A)** Alveolar and zygoma class comparison. **B)** All classes included.

Figure 3.15 shows the segmented skull, the *bone-CSM* design, and the conventional obturator in different views with a colored-coded distance map overlay of two cases. The colors indicate whether there is an overestimation (red) or underestimation (blue) of the CSM shape compared to the conventional obturator. As seen by the blue colors in Figure 3.15A, the CSM shape was mostly underestimated except for 1-2mm at the medial side (nose septum). The CSM design shape in Figure 3.15B indicates more overestimation (red), especially at the orbit as seen by the anterior view. An overview of all cases for both the *bone-CSM* and *bone & soft tissue-CSM* designs is shown in Appendix H1 and H2, respectively. Most of the *bone & soft tissue-CSM* designs are overestimated in shape and volume as seen by the red areas.

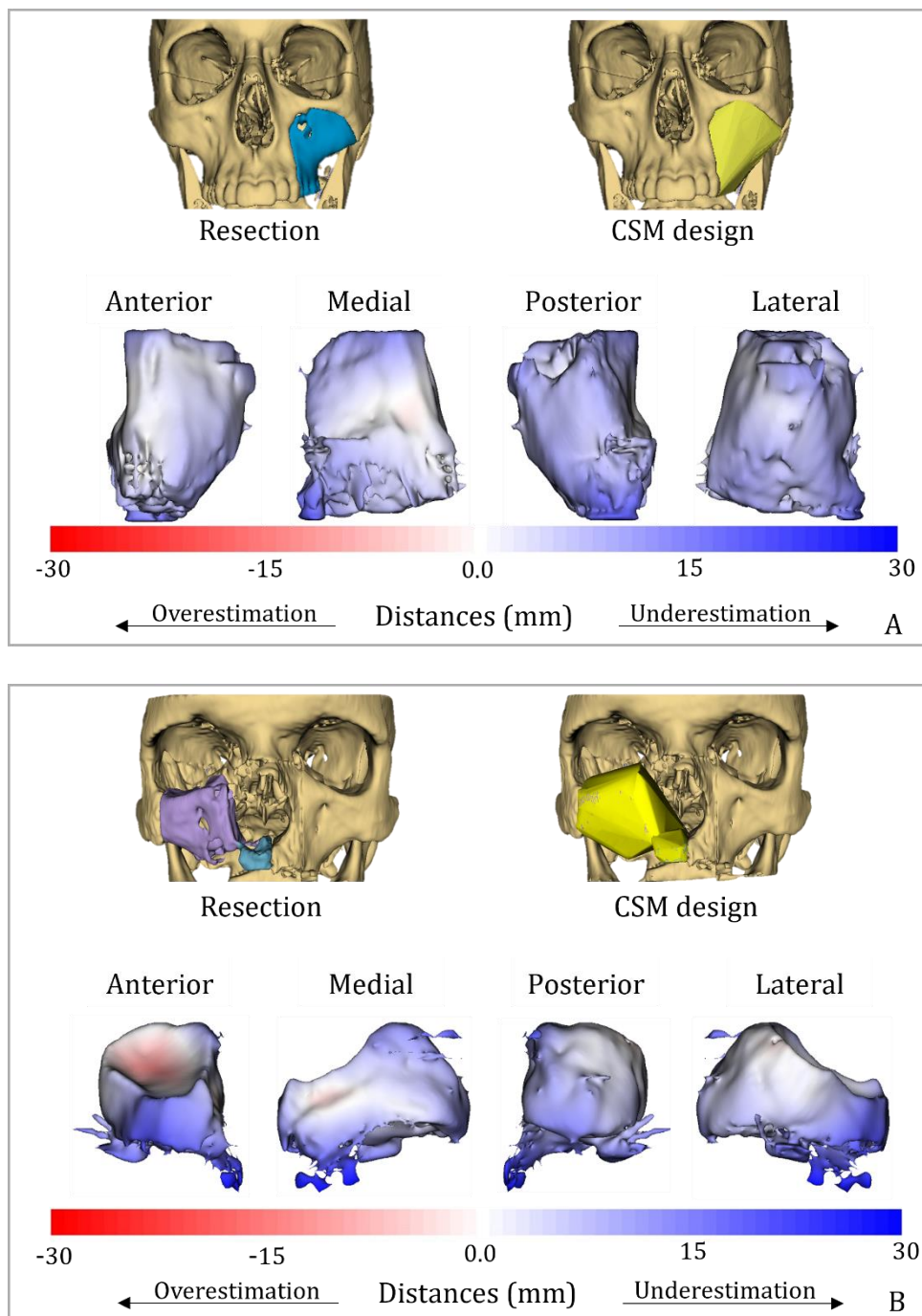


Figure 3.15. Two cases with their closed surface model (CSM) (yellow), designed from the segmented resection bone, and the conventional obturator with a distance mapping overlay. The overlay indicates the distance between the conventional and the CSM obturator (i.e. red/negative distance is an overestimation and blue/positive distance is an underestimation). **A)** Patient 1, classification Z-III. **B)** Patient 12, classification Z-IV. Note the increased overestimation in patient 12 compared to patient 1, and the amount of segmentation spikes in the conventional obturators.

3.4 Discussion

This retrospective study verified the closed surface model obturator by comparing the shape, volume, and weight reduction with Ooms' classified conventional obturators. The theoretical maximum achievable weight reduction was 69%, and the 0.8 scaled *bone-CSM* design and clinical reference designs achieved an average weight reduction of 47%.

3.4.1 Interpretation of results

The Pearson's correlation coefficient between volumes and the absolute weight reduction calculated for the *bone-CSM* was close to the value one, which shows a high direct positive correlation. The correlation indicated that the weight reduction increased for larger obturator volumes. Nevertheless, the percentage weight reduction results showed that volume did not influence the reduction as seen by the horizontal correlation plots. Furthermore, the weight reduction values of the TCR and *bone-CSM* designs had comparable results. These findings enhanced the use of the CSM method. Though, the volumes of the *bone & soft tissue-CSM* designs were often too large, resulting in a weight gain instead of a weight reduction. For this reason, these designs were excluded from the weight reduction results. These findings, however, did not correspond with the previous clinical-trial research results for those Ooms' classes.

The 0.8-scale was also based on the clinical results of Chapter 2. The results in Figure 3.10 compared the weight reduction for different scales of an average-sized obturator and showed exponential growth. A larger scale will thus result in more weight reduction with a maximum of 70% (TMR) due to the weight of the Clear resin. The TMR, however, is not clinically feasible because of the missing denture relining material, which deteriorates the clinical fit and does not allow post-operative adjustments by the prosthodontist. Therefore, it is essential to find a scale that balances clinical usability and weight reduction, in which the results suggested the 0.8-scale. Even though this scale does not achieve the maximum weight reduction, the 40-50% reduction is larger compared to literature stating that a hollow obturator reduces the weight by 7 – 33% [35]. The next step for future research would be optimizing the scale and final shape of the CSM obturator.

The two bilateral cases resulted in significant outliers in the weight reduction results. Therefore, they were excluded from the shape and volume results. Also, the Ooms' classification system only considers unilateral resections. The bilateral cases, classed as A-IV and Z-IV, were controversial with these terms. Expanding the classification system or designing a separate system would allow the inclusion of bilateral cases.

Turning now to the shape results, which were assessed by the HDs. There were significant differences between the maximum HD and the 95% HD. The resolution of the segmentations could be a possible explanation, which will be discussed in the next section. The mean average HD and 95% HD were less than 5mm for the *bone-CSM* designs. Although we desired that the CSM designs were not exceeding the conventional obturator shape, it needs to be considered that the scans were made within an average of six weeks after surgery. The first clinical case (Chapter 2) indicated that the size of the conventional obturator decreased by 10 – 15 mm after 7 weeks of surgery (Figure 2.19). Therefore, we expected that the segmented obturators were larger directly after surgery than visible on the postoperative CT scans, which probably resulted in higher HD values. For this reason, the prosthodontist still considered the *bone-CSM* designs clinically useful, despite some of the red overestimated areas as seen in the color-coded distance maps in Appendix H1.

Regarding the Ooms' classification system, the 'Z'-classes had a larger volume than the 'A'-classes, especially the Z-IV classes. This result followed our expectations based on the increased height and width of the resections for those classes (Figure 3.5). Ooms' classes A-II and A-III had the smallest obturator volume and the least weight reduction (<20 gram). It should be researched whether those types of obturators have enough physical impact on the patient and, therefore, see

whether it is feasible designing them. Even though this study failed to demonstrate the *bone- and soft tissue CSM* weight reduction, the volume differences between the classes suggested that obturators can be classified and that these classes may need different CAD/CAM design approaches. Yet, it needs to be considered that the number of cases per class in this research cohort was not equal.

3.4.2 Strength and weaknesses

The study had multiple limitations. First, there were limitations regarding the population size. The research cohort was relatively small due to the lack of postoperative CT scans, which resulted in exclusion of maxillectomy patients. The population size limitation mainly affected the obturator comparison between the Ooms' classification classes. However, this was not the main objective of this study. More cases in different classes would provide more knowledge for the (future) CSM designs. Future cooperation with other hospitals could enlarge the cohort. Despite the population size, the Pearson's correlation plots showed significant results and provided insight in the clinical applicability of the CSM designs.

Second, there were limitations regarding the accuracy of the CT scans. The scans with a larger slice thickness (>1 mm) affected the resolution of the skull and resection margin segmentations. Hence, soft tissue could not always be segmented, and classes could not be distinguished very well. The resolution could lead to too sharp protruding edges and overestimations in the CSM designs. For example, the sharp edges caused an increased HD in case 11, caused by a slice thickness of 5 mm. Usually, these edges would manually be smoothed and removed before clinical implementation (see methods chapter 2), which probably would have led to a lower HD. These manual alterations were not made to prevent inter-observer variability in designing the obturators. Still, the volume of the *bone-CSM* designs were considered useful based on the minimal HD overestimations, despite the lack of alterations. Furthermore, the accuracy of the CT images sometimes resulted in holes and spikes within the conventional obturator segmentations, which could have led to an under- or overestimation of the obturator volume, respectively. Although the slice thickness affected the results, it needs to be considered that nowadays, CT scans are often made with a slice thickness of 1 mm, which minimizes this limitation regarding accuracy.

Third, the use of segmented soft tissue as a design method for the *bone & soft tissue-CSM* designs was questioned by the results. For example, cheek fat was included in the Z-II and Z-IV designs. The cheek fat, however, was often crooked in the scan by the tumor. In addition, the mastication muscles for classes A-II and A-IV were sometimes hard to distinguish in the scans because of the slice thickness or scattering. As an alternative in future designs, the lateral side of *bone-CSM* designs could be enlarged, similar to the fourth clinical case of Chapter 2. The enlargement resulted in the best clinical fit, which indicated that this could be an alternative method for the Ooms classes with a wide obturator volume.

Fourth, the pre-and postoperative CT scans were registered by one observer, causing inter-observer variability, in which the registration error was not measured. On the other hand, the whole skull was registered with multiple notable features at different locations, such as the infraorbital foramen (Chapter 1 Figure1). Also, Chapter 2 indicated that the FPR method resulted in a minimal error (<1mm). Therefore, it is expected that the registration error in this study would have been similar and had minimal effect on the results.

Finally, it needs to be considered that all calculations were digitally measured and do not simulate any clinical conditions. Although the densities used in this research were based on clinical experiments, the water and bacteria uptake in the putty obturators could have differed in each case, affecting the actual weight. Also, the results lack information about the material properties of the designs in terms of strength and fracture load. In addition, the clinical fit of the CSM designs was not researched in this study and should be considered in future randomized control clinical trial studies.

3.4.3 Future recommendations

A larger cohort in future research would gain more information about the differences in shapes, volume, and weight reduction between the CAD/CAM designs and the conventional ISOs. In addition, it is expected that a larger cohort would allow more Ooms' class distribution and therefore more insight into the shape prediction for CAD/CAM designs, since no research has previously been published on this subject. Though, slight alterations in the design methods need to be made for the Ooms' classes A-II, A-IV, Z-II, and Z-IV that result in the *bone-and soft tissue-CSM* obturators. Furthermore, the classification could be expanded, or classes could be combined to allow the inclusion of bilateral cases.

The question raised by this study is thus whether the use of segmented soft tissue is the optimal method to enlarge the CSM design. It is recommended to use other strategies, such as enlargement of the *bone-CSM* in the lateral direction, as used in one of the designs in the previous chapter. On the other hand, the shape, volume, and weight-reduction results of the *bone-CSM*, together with the clinical results of Chapter 2, indicate a clinically valid method for designing CAD/CAM obturators. Future research should further optimize these methods, including optimizing the 0.8-scale.

On the other hand, this study raised the question whether the limitations, such as the CT accuracy and the underestimated volume of the segmented conventional obturators, affected the results. Also, no manual alterations were made to the CSM designs which would have altered the shape by cutting off the sharp edges. It is recommended for future research to focus more on a clinical-trial study rather than a retrospective study due to these limitations. In addition, a retrospective study does not gain information about the clinical fit.

3.5 Conclusion

The purpose of the current retrospective study was to verify the digital hollow CSM design according to the Ooms' classification system in terms of weight reduction, shape, and volume.

The findings in this study confirmed that the *bone-CSM* design is a promising CAD/CAM method for replacing conventional ISOs. The forthcoming steps would be to investigate the clinical fit by implementation through a randomized clinical-trial study and to investigate the safety of the designs by researching the material properties.

Additional improvements of the Ooms' classification are needed to allow direct shape prediction of the ISO shapes. Furthermore, the designs need further optimizations in the scale and design methods for the larger obturators.

4. Material properties of the CSM obturator

4.1 Introduction

The previous chapters assessed multiple factors such as the shape, volume, and weight reduction of the novel CAD/CAM obturator prosthesis. Another essential aspect before clinical implementation is the research of the biomechanical behavior of the obturators. Although the prosthesis design could be very comfortable for the patient, it could be, on the contrary, susceptible to fracture. In general, the mechanical failure in the acrylic resin can be enhanced by the oral cavity because of the unfriendly environment that presents temperature, pH variation, and fatigue cycling. In addition, water absorption occurs in acrylic resins causing dimensional instability, which reduces the tensile strength of the material and eventually could lead to fracture [68]. Therefore, the dimensional stability of prosthetic devices, associated with their retention and comfort, is an important parameter.

Besides the demands of the oral cavity, the prostheses are exposed to gravity-induced stress and chewing load. Furthermore, the obturator can experience increased mechanical stress during the prosthesis removal for cleaning or adjustment purposes during the follow-up visits. It is expected that prosthetic devices such as the obturator prosthesis could stand out against both the aging effect and the bending moment during insertion and removal of it in the patient's mouth.

According to a literature review, the key factor for the success or failure of this treatment modality is to evaluate the pattern in which stresses are transferred to the prosthetic device [69]. However, most of the available studies only consider the chewing load simulation instead the stress generated during the prosthesis removal [70]. One viable method for clinicians to assess prostheses deformation due to the oral cavity environment is with the aid of 3D models superimposition and intraoral scanners [71]. Additionally, the fracture resistance of the prosthesis can be measured with compressive loading using a universal testing machine. However, to our knowledge, there is a lack of data about obturator prostheses in the literature, especially for prostheses made by additive manufacturing through 3D printing [72].

Another widely used tool to assess the mechanical behavior of removable partial dentures, prostheses, and supporting structures is finite element analysis (FEA). FEA provides digital quantitative 3D information in which the loading and stress distribution can be simulated from 3D model data. For the FEA simulation, a certain load can be applied to the chosen area of interest with additional boundary conditions [69] [73],[74], [75].

4.1.1 Study aim

This study aimed to evaluate whether the CSM designs are limited to the demands of the oral cavity and mechanical stress during the prosthesis removal. These mechanical properties are analyzed by using one of the CSM designs in chapter 2. The hypothesis was that most stress during the prosthesis removal would occur in the sharpest angles of the prosthesis, which is at the connection between the baseplate and obturator. In addition, it was expected that the prosthesis was resistant to the simulated oral cavity environment.

4.2 Methods

4.2.1 Pre-processing

The best-fitted CSM design of the fourth clinical maxillectomy patient (Chapter 2.3.3, Figure 2.18 C) was chosen to research the mechanical behavior. The prosthesis was printed (Figure 4.1) six times in Clear resin using the identical settings as the clinical case study of Chapter 2. Each design was numbered for identification and scanned using the 3Shape TRIOS scanner (see Figure 1.10). To improve the scanning accuracy, the surfaces were coated with powder and additional color variation was created with permanent markers [76].



Figure 4.1. Three-dimensional (3D) printed computer-aided and manufactured designed immediate surgical obturators.

Next, the prints were weighed using the Mettler-Toledo analytical balance and placed for three weeks in water with a temperature of 37° Celsius to simulate the aging in the oral cavity (Figure 4.2). The prints were dried and weighed again to measure the water absorption. In addition, the prostheses were intraoral scanned again to measure the material stability which will be further explained.



Figure 4.2. Experiment tools. **A)** Material weighting using the Mettler-Toledo analytical balance. **B)** Stove with the prosthesis placed in 37° Celsius heated water.

4.2.2 Compressive resistance test

The fracture mechanic performance of the prostheses was researched by a compressive resistance test (see Figure 4.3). The prostheses were clamped at the obturator side and vertical compressive forces with a linear speed of 1 mm/min were applied through a screw using the Instron machine (Model no. 6022, Instron Ltd., Buckinghamshire, UK). Dental composite resin was added in place of compression for the stabilization of the screw.



Figure 4.3. Vertical applied load (red arrow) on the fixated obturators using the Instron 6022 machine.

4.2.3 Digital analysis

To measure the material stability by the aging simulation, the optical scans were superimposed by using the best-fit alignment and compared in a 3D inspection software program (GOM Inspect 2019; GOM) [77]. The material stability analysis was evaluated with color-coded maps and with absolute deviations.

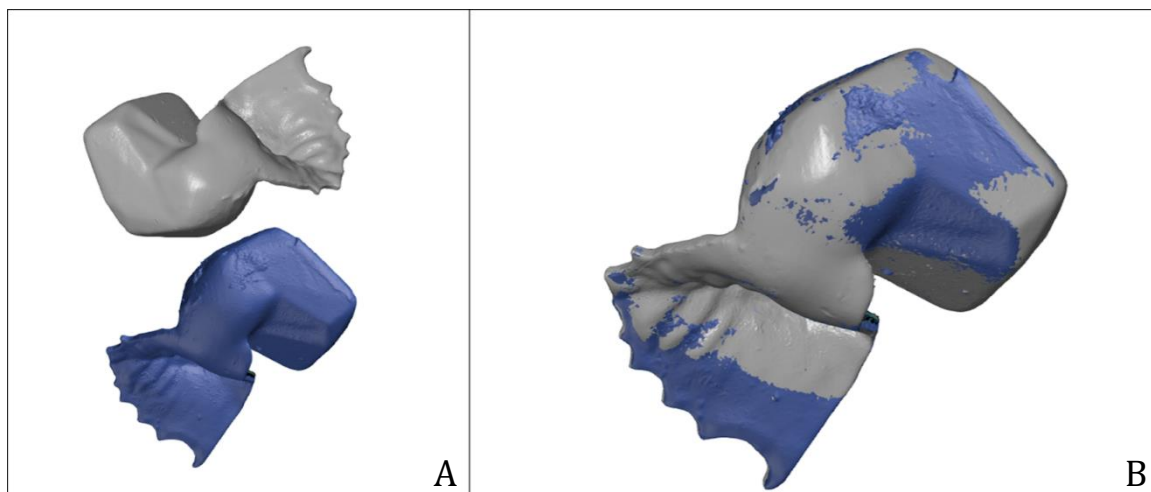


Figure 4.4. Best-fit alignment of the intraoral scanned prosthesis. **A)** Before alignment. **B)** After alignment.

4.2.4 Finite element analysis

For the FEA, the STL files containing the intraoral scans were converted to a standard for the exchange of product (STEP) format to the CAD software (ANSYS 19.2; ANSYS Inc., Houston, TX, USA) [70], [78]. A 3D mesh of an intraoral scan was generated (Figure 4.5A). The Clear resin elastic modulus (2.8 GPa), and a Poisson ratio of 0.3 based on acrylic resin dentistry, were assigned to the mesh [79], [80]. Similar to the compressive test, the prosthesis was constrained at the

obturator side and a vertical load was applied to the lateral side, opposite to the obturator. The load magnitude was the average fracturing load defined by the *in-vitro* compressive test. The tensile stress and deformation after removal of the prosthesis in the patient's mouth were simulated with this FEA set-up [70], [81].

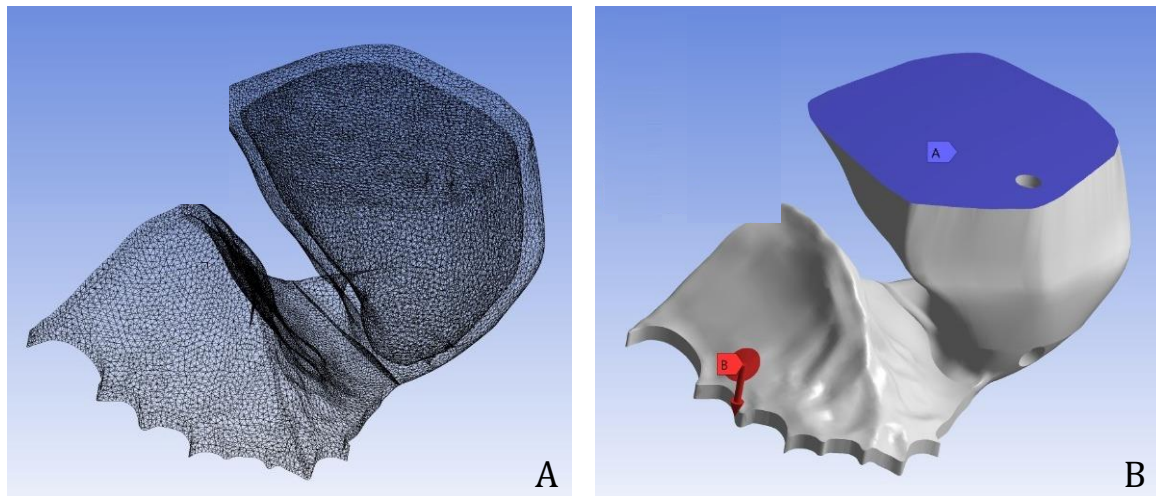


Figure 4.5. 3D models in Ansys. **A)** Mesh. **B)** Constraint obturator (purple) with an applied vertical load on the opposite lateral side of the baseplate (red arrow).

4.3 Results

4.3.1 Compressive resistance test

The results of the compressive resistance test are presented in Table 4.1, the average fracturing load is about ± 25 N. Furthermore, prostheses 1-3 were not sealed enough, and therefore water leakage occurred within the obturator (Figure 4.6 A). The table also presents the weight differences, in which the sealed prosthesis (number 4-6) showed the least weight increase percentage of around 2%.

Table 4.1. Weight and fracturing load results of the compressive resistance test.

No.	Weight (g) T0	Weight (g) T1	Weight increase (%)	Sealing capability	Fracturing load (N)
1	9.87	10.15	2.84	No	-30.62
2	9.84	10.38	5.48	No	-17.35
3	9.92	10.56	6.49	No	-23.05
4	10.00	10.22	2.16	Yes	-36.06
5	9.99	10.21	2.22	Yes	-26.12
6	9.93	10.15	2.16	Yes	-17.78
$\mu \pm \sigma$	9.92 ± 0.06	10.28 ± 0.16	3.56 ± 1.92	-	25.16 ± 7.34

Figure 4.6 B shows the results of the fracture locations of the six baseplates after the compressive resistance test. As seen in the Figure, all prostheses fractured at the transition side between the obturator and baseplate.

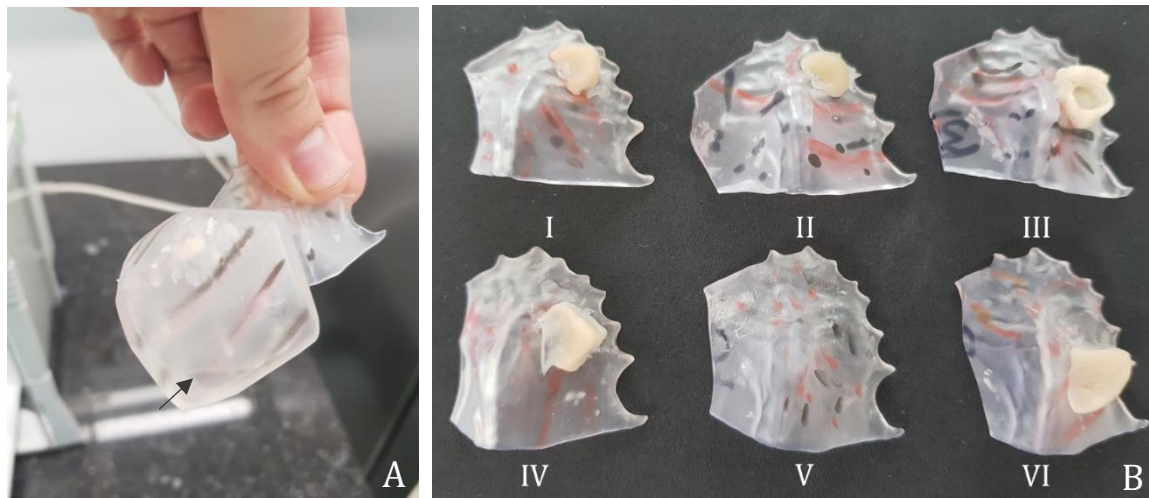


Figure 4.6. Prostheses after the aging simulation and compressive resistance test. **A)** Water leakage (black arrow) in the obturator. **B)** Fracture locations after the applied load.

4.3.2 Material stability analysis

Figure 4.7 shows the results of one of the prosthesis material deformities, presented with color-coded maps in the GOM software. As seen by the figure, the vast majority of the prosthesis is colored green, indicating no deformation. The highest value (± 1 mm) was noticed at the lateral side of the baseplate opposite to the obturator. In addition, the palate midline shows a deformity of (± 0.5 mm).

Table 4.2 shows similar material stability results as Figure 4.7, presented in absolute deviations of all prostheses. No alignment was possible for prosthesis number 4. As seen in the table the average deviation is 1.38 mm, and the maximum deviation value is 1.82mm.

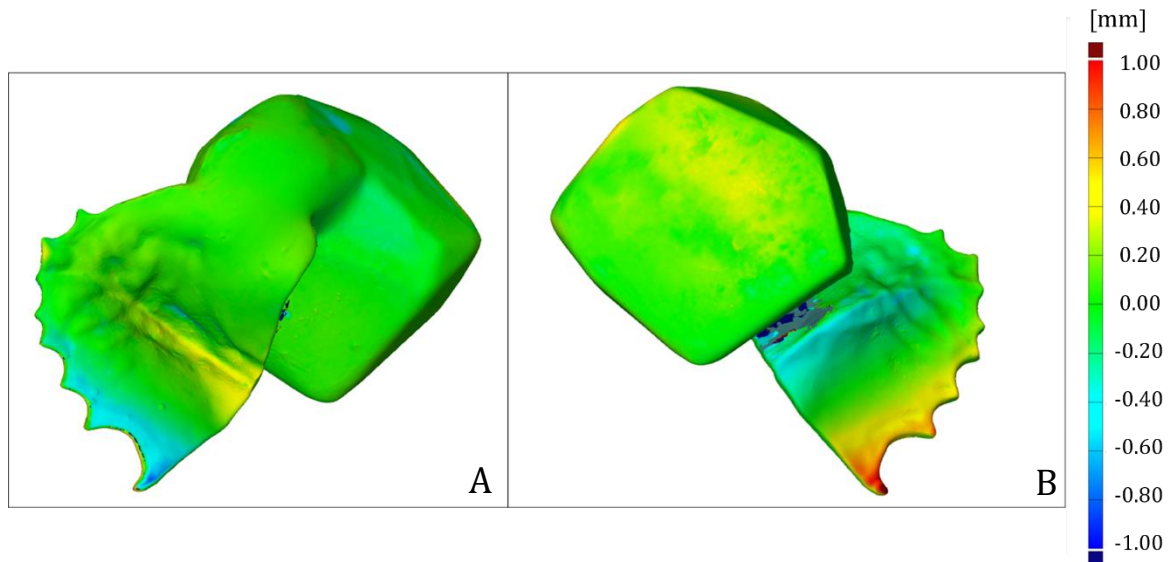


Figure 4.7. Material deformity after the aging simulation. **A)** Bottom surface. **B)** Upper surface.

Table 4.2. Absolute deviations of the material deformities.

No.	Absolute deviation (mm)
1	1.15
2	1.82
3	1.70
4	-
5	0.90
6	1.35
$\mu \pm \sigma$	1.38 ± 0.38

4.4.3 Stress assessment

Figure 4.8 shows the results of the tensile stress after the obturator constraint and applied average fracturing load of 25 N (Table 4.1) in ANSYS. As seen by the upper surface (Figure 4.8 A), the highest and most tensile stress is generated at the connection side between the baseplate and obturator. The tensile stress peak was 67.4 MPa.

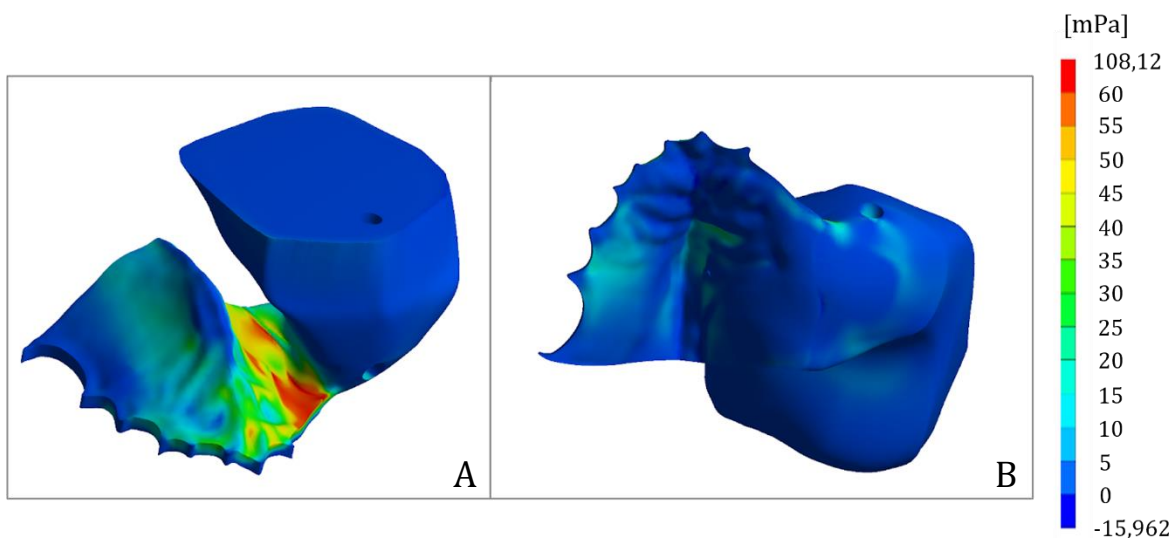


Figure 4.8. Tensile stress generated in the prosthesis. **A)** Upper surface. **B)** Bottom surface.

Figure 4.9 shows the deformation results of the prosthesis after the constraint of the obturator and the applied vertical load on the lateral side of the baseplate in ANSYS. Similar to the compressive test, the prosthesis showed elastic behavior before fracture and deforms according to the simulation with a minimum of 0 mm on the obturator side, and with a maximum of 19 mm on the opposite side.

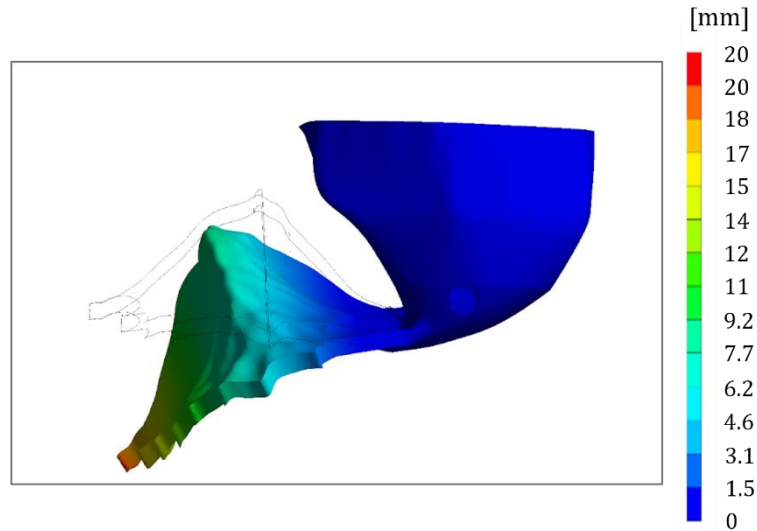


Figure 4.9. Deformation of the prosthesis during incidence of removal force.

4.4 Discussion

This material property study aimed to predict the clinical reliability of a Clear resin CAD/CAM designed immediate surgical obturator in the oral cavity environment and researched the mechanical stress during the prosthesis removal. In the present study, water absorption of 2% and material deformation at the thinnest, lateral side of the baseplate were observed, rejecting the null hypothesis.

4.4.1 Interpretations of results

Researching the mechanical properties are important in the field of maxillofacial prosthetics and removable dentures. Several studies use FEA to study the stress distribution in maxillofacial obturator prostheses. For example, Harihara Sudhan et al. 2020 used FEA to study the tensile stress in different definitive CAD/CAM-designed obturators after a digitally applied chewing load of 150 - 250 N [82]. The study of de Sousa et al. (2014) used FEA to research the stress on implanted-supported obturator prostheses for edentulous patients. They used an applied force of 35 N and 80 N, representing the maximum occlusal (jaw enclosing) force of the surface of the anterior and posterior teeth, respectively [83]. In the present study, FEA was used with a vertical applied load of 25 N, aiming to simulate the pulling of the prosthesis during removal.

In addition to the *in-vitro* experiment, the present investigation used a numerical approach by FEA. The FEA, however, does not consider all the conditions found in the oral environment. The oral cavity eases the water uptake due to thermal changes and moisture contamination, causing internal stress and could eventually result in fracture [84]. The extent and rate of water uptake of the denture resins depend on the material polarity. Yet, it was expected that a longer aging simulation than the three weeks would have not altered the chemical reaction (i.e., the 2% water absorption). It was also highly expected that the lack of decent sealing was caused by the insufficient enclosing of the print holes with TAB-2000 powder (see Chapter 2), which resulted in the larger weight increase percentages.

The use of a virtual model superimposition to evaluate printed structures' stability has been already reported in literature. For example, the study by Goodacre et al. (2016) used this method to compare the denture base adaptation of conventional and CAD/CAM fabricated complete dentures [85]. The CAD-CAM denture was found to be the most accurate and reproducible denture fabrication technique. As seen in the literature, the use of a virtual model superimposition allows for a fast and highly accurate evaluation [77]. Structure stability studies of the 3D printed maxillofacial prosthesis, however, are lacking. However, in the present study, the effects of 37^o C water uptake were investigated, which resulted in a bending of the material at the most lateral side of the baseplate, opposite to the obturator. This location was not surprising, considering this is the thinnest part of the prosthesis. Also, the deformation in this specific location was about 1mm, which probably would not have a severe consequence for the clinical fit. In addition, in a clinical situation, the prosthesis is fixed to the palate and tight between the remaining teeth in the patient's mouth, which questions if the prosthesis would also deform as it did here.

Moreover, the *in-vitro* compressive resistance test resulted in an average fracturing load of 25 N, which resulted in a digital FEA tensile stress peak of 67.4 MPa at the connection side of the baseplate and obturator. The tensile stress peak was similar to the maximum tensile strength of 65 MPa of Clear resin, as stated by the manufacturer (Formlabs) [79]. These results increased the reliability of the fracturing load results and the use of FEA for future mechanical properties studies.

The compressive force, however, that is applied during prosthesis removal was not previously researched, which raises the question of whether the fracture load of 25 N is clinically reliable. The fracture load amount is, for example, far less than the average chewing load. The ISO, however, other than the definitive obturator, has all its retention hooked around the patient's

remaining teeth or zygoma bone. Therefore, the ISO experiences far less chewing load. In addition, a previous finite element study simulated 10 N of force to remove a conventional full denture from its position. Therefore, assuming this value as a threshold and the results from the present investigation, the prosthesis design manufactured in this report would be able to resist the removal force without fractures or mechanical complications [73]. Furthermore, both the *in-vitro* test and FEA indicated the amount of bending behavior of the material before fracture. The bending could be a warning for the prosthodontist and patient that a possible fracture occurs when the removal continues at this position.

4.4.2 Strength and weaknesses

The present study had multiple limitations. First, this study researched only one ISO design. As seen in the previous chapters, the maxillary defect and consequently the obturator prosthesis differ in shape and size. Therefore, the mechanical stress distribution could vary in different prosthesis designs. On the other hand, each design is made from the same material and consists of the same two elements: the baseplate and the obturator. Thus, it is expected that these findings will not highly differ from other prosthesis designs. The designs, however, could be optimized by creating smoother and rounder shapes to strengthen the prosthesis. For example, at the transition between the baseplate and the obturator because the results indicated the most stress here.

Second, the *in-vitro* compressive resistance test and FEA may not reproduce the oral environment. On the other hand, the clinical conditions were simulated by the aging simulation. As mentioned in the previous section, it was expected that the water leakage during the aging simulation was caused by insufficient enclosing of the print holes. The executor of this step lacked experience compared to a highly capable prosthodontist. Additionally, in a clinical situation, the CAD/CAM prosthesis would be covered with reline material which would have further sealed the prosthesis. Therefore, it is expected that there will be no water leakage in future clinical CAD/CAM ISOs.

Third, the prostheses were printed in Clear resin for research purposes and cost savings. For final clinical implementation, it is recommended to use a more biocompatible material such as Dental Clear Resin (Formlabs). It is expected that this material is better resistant to the oral environment. Furthermore, in terms of the oral environment, the aging simulation was limited to the temperature of 37° Celsius. Varying temperatures, pH values, etc. were not studied.

Fourth, the *in-vitro* tests needed to be repeated several times because of the instability of the screw on the surface of the prosthesis, even with the additional composite resin. Also, the clamping of the obturator and the exact surface point where the vertical force was applied differed slightly in each prosthesis. These factors contributed to the differences in the fracturing loads. On the other hand, the average fracture loads resulted in very trustworthy results, as seen in the tensile stress FEA measurements. Furthermore, the load was measured on only one surface location at a time and only in one direction. The FEA can be expanded to different kinds of loads, on multiple surface points in future research. Yet, it needs to be considered that it remains difficult to digitally simulate the exact loads in all directions. A clinical trial study would be more helpful than simulating it all.

Finally, to measure the digital material stability, the prostheses were intraoral scanned by one observer, resulting in intra-observer variability. The registration error was not measured, but this is the most precise scanner currently available. It is thus not expected that this affected the results [46]. On the other hand, the scanner could not reach the whole surface of the medial side of the obturator due to the relatively high palate blocking the scanner. Thus, the material deformity was not measured across the whole surface.

4.4.3 Future recommendations

For the future clinical implementation of the prosthesis, it is recommended to optimize the design to obtain its maximal strength. The optimization includes mainly the connection between the baseplate and obturator. According to the results, this is likely the first location for the prosthesis

to fracture. The optimization should include a more curved and smooth transition without blocking the surrounding anatomical structures.

Furthermore, the results indicated that the experimental set-up for both the *in-vitro* test and the FEA were reliable. Therefore, it is recommended to redo these experiments after researching different designs or alterations. In addition, the clinical environment could be more simulated in terms of varying temperatures and pH values. On the other hand, it needs to be considered that it is difficult to simulate the exact clinical environment, which raises the question of what more knowledge additional simulated data would gain. It would be recommended, however, to compare the biocompatible Dental Clear resin using this set-up with the findings of this research.

4.5 Conclusion

This study aimed to study the mechanical stress during removal of the Clear resin CAD/CAM designed ISOs and whether these prostheses are consistent with the demands of the oral cavity.

The finite element analysis in this study indicated to be a reliable tool to predict the mechanical stresses of the maxillary prosthesis. The most tensile stress was found at the connection between the baseplate and obturator, which can be considered in future optimizations of the CAD/CAM design. In addition, the material deformed at the thinnest part of the prosthesis after the aging simulation. Using a more biocompatible material for future clinical implementation could result in higher resistance against oral demands.

References

- [1] J. Kortés, H. Dehnad, A. N. T. Kotte, W. M. M. Fennis, and A. J. W. P. Rosenberg, "A novel digital workflow to manufacture personalized three-dimensional-printed hollow surgical obturators after maxillectomy," *Int. J. Oral Maxillofac. Surg.*, vol. 47, no. 9, pp. 1214–1218, Sep. 2018, doi: 10.1016/J.IJOM.2018.03.015.
- [2] S. Iyer and K. Thankappan, "Maxillary reconstruction: Current concepts and controversies," *Indian J. Plast. Surg.*, vol. 47, no. 1, p. 8, 2014, doi: 10.4103/0970-0358.129618.
- [3] O. F. Ikusika, O. O. Dosumu, D. M. Ajayi, and T. J. Ogunrinde, "Effect of resilient lining of obturator bulbs on patients with maxillectomies," *J. Prosthet. Dent.*, vol. 116, no. 6, pp. 932–936.e1, Dec. 2016, doi: 10.1016/J.PROSDENT.2016.04.011.
- [4] M. Dalkiz and A. S. Dalkiz, "The Effect of Immediate Obturator Reconstruction after Radical Maxillary Resections on Speech and other Functions," *Dent. J.*, vol. 6, no. 3, Sep. 2018, doi: 10.3390/DJ6030022.
- [5] D. J. Bell, "Maxilla | Radiology Reference Article | Radiopaedia.org," 2021. <https://radiopaedia.org/articles/maxilla>.
- [6] K. L. Moore and A. F. Dalley, *Clinically Oriented Anatomy*. Wolters kluwer india Pvt Ltd, 2018.
- [7] A. Sieroslawska, "Maxilla: Anatomy, function, clinical aspects | Kenhub," 2021. <https://www.kenhub.com/en/library/anatomy/the-maxilla>.
- [8] M. Helwany and M. Rathee, "Anatomy, Head and Neck, Palate," *StatPearls*, Jun. 2021, [Online]. Available: <https://www.ncbi.nlm.nih.gov/books/NBK557817/>.
- [9] "Definition of maxillary sinus - NCI Dictionary of Cancer Terms - National Cancer Institute." <https://www.cancer.gov/publications/dictionaries/cancer-terms/def/maxillary-sinus>.
- [10] J. Jones, "Maxillary sinus | Radiology Reference Article | Radiopaedia.org," Sep. 26, 2021. <https://radiopaedia.org/articles/maxillary-sinus?lang=us>.
- [11] H.-J. Kim, K. K. Seo, H.-K. Lee, and J. Kim, "General Anatomy of the Face and Neck," *Clin. Anat. Face Fill. Botulinum Toxin Inject.*, pp. 1–53, 2016, doi: 10.1007/978-981-10-0240-3_1.
- [12] R. M. Soriano and J. M. Das, "Anatomy, Head and Neck, Maxilla," *StatPearls*, Sep. 2020, [Online]. Available: <https://www.ncbi.nlm.nih.gov/books/NBK538527/>.
- [13] M. Sharawy and C. E. Misch, "22: Applied Anatomy for Dental Implants | Pocket Dentistry," Jan. 05, 2015. <https://pocketdentistry.com/22-applied-anatomy-for-dental-implants/>.
- [14] S. Shafique and J. M. Das, "Anatomy, Head and Neck, Maxillary Nerve," *StatPearls*, Jun. 2021, [Online]. Available: <https://www.ncbi.nlm.nih.gov/books/NBK542277/>.
- [15] O. Locca *et al.*, "Locally advanced squamous cell carcinoma of the head and neck: A systematic review and Bayesian network meta-analysis of the currently available treatment options," *Oral Oncol.*, vol. 80, pp. 40–51, 2018, [Online]. Available: <https://doi.org/10.1016/j.oraloncology.2018.03.001>.
- [16] S. Sjöstedt *et al.*, "Incidence and survival in sinonasal carcinoma: a Danish population-based, nationwide study from 1980 to 2014," <https://doi.org/10.1080/0284186X.2018.1454603>, vol. 57, no. 9, pp. 1152–1158, Sep. 2018, doi: 10.1080/0284186X.2018.1454603.
- [17] K. Rahmani, S. Taghipour Zahir, M. Baghi Yazdi, and A. Navabazam, "Aggressive Adenoid Cystic Carcinoma of Maxillary Sinus in a 43-Year-Old Male: Rare Case Report and Review of Literature," *Case Rep. Med.*, vol. 2017, 2017, doi: 10.1155/2017/2324717.
- [18] A. Young and O. T. Okuyemi, "Malignant Tumors of the Palate," *StatPearls*, Feb. 2022, [Online]. Available: <https://www.ncbi.nlm.nih.gov/books/NBK564515/>.
- [19] N. M. Praveena and G. Maragathavalli, "Carcinoma of the Maxillary Antrum: A Case Report," *Cureus*, vol. 10, no. 5, May 2018, doi: 10.7759/CUREUS.2614.
- [20] P. M. Dubal *et al.*, "Squamous cell carcinoma of the maxillary sinus: A population-based analysis," *Laryngoscope*, vol. 126, no. 2, pp. 399–404, Feb. 2016, doi: 10.1002/LARY.25601.
- [21] J. J. Beitler, M. W. McDonald, J. T. Wadsworth, and P. A. Hudgins, "Sinonasal Cancer," *Clin. Radiat. Oncol.*, pp. 673–697.e2, Jan. 2015, doi: 10.1016/B978-0-323-24098-7.00036-8.
- [22] "Maxillary sinus cancer TNM stages and grades | Cancer Research UK," 2021. <https://www.cancerresearchuk.org/about-cancer/nasal-sinus-cancer/stages-grades/maxillary-sinus-tnm>.
- [23] M. N. Alhajj, I. A. Ismail, and N. Khalifa, "Maxillary obturator prosthesis for a

- hemimaxillectomy patient: A clinical case report," *Saudi J. Dent. Res.*, vol. 7, no. 2, pp. 153–159, Jul. 2016, doi: 10.1016/J.SJDR.2016.03.001.
- [24] "Maxillectomy and Partial Maxillectomy Information for patients," *Oxford Centre for Head and Neck Oncology*, 2019. .
- [25] D. W. Klotch and N. J. Panetta, "3 Ablative and reconstructive surgery of the midface and craniofacial junction," *Adv. Craniomaxillofacial Surg.*, Oct. 2020, doi: 10.1055/B-0040-178441.
- [26] H. S. Won *et al.*, "Treatment outcome of maxillary sinus cancer," *Rare Tumors*, vol. 1, no. 2, pp. 110–114, Dec. 2009, doi: 10.4081/RT.2009.E36.
- [27] T. Albonette-Felicio, G. G. Rangel, R. Martínéz-Pérez, D. A. Hardesty, R. L. Carrau, and D. M. Prevedello, "Surgical management of anterior skull-base malignancies (endoscopic vs. craniofacial resection)," *J. Neuro-Oncology 2020 1503*, vol. 150, no. 3, pp. 429–436, Feb. 2020, doi: 10.1007/S11060-020-03413-Y.
- [28] H. Hoffman, "Maxillectomy | Iowa Head and Neck Protocols," 2017. <https://medicine.uiowa.edu/iowaprotocols/maxillectomy>.
- [29] H. El Fattah, A. Zaghoul, E. Pedemonte, and T. Escuin, "Pre-Prosthetic surgical alterations in maxillectomy to enhance the prosthetic prognoses as part of rehabilitation of oral cancer patient," *Med. Oral Patol. Oral Cir. Bucal*, vol. 17, no. 2, p. e262, Mar. 2012, doi: 10.4317/MEDORAL.17482.
- [30] A. Dayal Gupta, "Maxillofacial defects and their classification: a review.," *Int. J. Adv. Res.*, vol. 4, no. 6, pp. 109–114, 2016, doi: 10.21474/IJAR01.
- [31] "3 Ablative and reconstructive surgery of the midface and craniofacial junction," *Adv. Craniomaxillofacial Surg.*, Oct. 2020, doi: 10.1055/B-0040-178441.
- [32] V. V. Haribhakti, "Prosthetic Rehabilitation: Fundamentals," *Restoration, Reconstr. Rehabil. Head Neck Cancer*, pp. 315–346, 2019, doi: 10.1007/978-981-13-2736-0_20.
- [33] M. Corsalini *et al.*, "Obturator Prosthesis Rehabilitation after Maxillectomy: Functional and Aesthetical Analysis in 25 Patients," *Int. J. Environ. Res. Public Health*, vol. 18, no. 23, p. 12524, Dec. 2021, doi: 10.3390/IJERPH182312524.
- [34] V. I. Shambharkar, S. B. Puri, and P. G. Patil, "A simple technique to fabricate a surgical obturator restoring the defect in original anatomical form," *J. Adv. Prosthodont.*, vol. 3, no. 2, p. 106, 2011, doi: 10.4047/JAP.2011.3.2.106.
- [35] H. S. Çöttert, A. G. Türk, R. Midilli, and S. Gode, "Immediate Obturator with Airway for Maxillary Resection Surgery: A Case Report," *Madridge J. Dent. Oral Surg.*, vol. 3, no. 1, pp. 80–84, Jan. 2018, doi: 10.18689/MJDL-1000119.
- [36] M. Alrawas *et al.*, "Sustaining an obturator prosthesis with zygomatic suspension wires in a case of subtotal maxillectomy and insufficient ridge supported retention: A case report," *Bangladesh J. Med. Sci.*, vol. 19, no. 3, pp. 582–585, 2020, doi: 10.3329/BJMS.V19I3.45879.
- [37] R. Appadurai, D. Lingeswar, B. Dilshad, and S. Maria, "Surgical retention for immediate obturator in maxillectomy patients," *Indian J. Dent. Res.*, vol. 30, no. 1, p. 133, Jan. 2019, doi: 10.4103/IJDR.IJDR_201_17.
- [38] N. Bettie, "A Conservative Method of Retaining an Interim Obturator for a Total Maxillectomy Patient," *J. Pharm. Bioallied Sci.*, vol. 9, no. Suppl 1, p. S299, Nov. 2017, doi: 10.4103/JPBS.JPBS_127_17.
- [39] L. Sadighpour and F. Massoumi, "Rhinorrhoea triggered by an obturator prosthesis: A clinical report," *J. Prosthet. Dent.*, vol. 97, no. 2, pp. 75–77, Feb. 2007, doi: 10.1016/J.PROSDENT.2006.12.004.
- [40] M. Lauren and G. Bolding and Ghassan, "Oral Rehabilitation Rehabilitation, dental/oral," *Oral Cancer*, Jun. 2020, doi: 10.1055/B-0040-176925.
- [41] K. Noh, A. Pae, J. W. Lee, and Y. D. Kwon, "Fabricating a tooth- and implant-supported maxillary obturator for a patient after maxillectomy with computer-guided surgery and CAD/CAM technology: A clinical report," *J. Prosthet. Dent.*, vol. 115, no. 5, pp. 637–642, May 2016, doi: 10.1016/J.PROSDENT.2015.10.015.
- [42] M. Brucoli, P. Boffano, A. Pezzana, C. Corio, and A. Benech, "The use of optical scanner for the fabrication of maxillary obturator prostheses," *Oral Maxillofac. Surg.*, vol. 24, no. 2, pp. 157–161, Jun. 2020, doi: 10.1007/S10006-020-00836-9.
- [43] A. Steenhuis, "Fabrication process of maxillary hollow bulb immediate surgical obturator using intraoral scanning technology and computer-aided design/ manufacturing," University of Twente, 2021.
- [44] P. Soltanzadeh, J. M. Su, S. R. Habibabadi, and M. T. Kattadiyil, "Obturator fabrication incorporating computer-aided design and 3-dimensional printing technology: A clinical

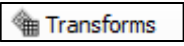
- report," *J. Prosthet. Dent.*, vol. 121, no. 4, pp. 694–697, Apr. 2019, doi: 10.1016/J.PROSDENT.2018.06.019.
- [45] J.-M. Park and J.-S. Shim, "Optical Impression in Restorative Dentistry," *Comput. Vis. Dent.*, Feb. 2019, doi: 10.5772/INTECHOPEN.84605.
- [46] G. Michelinakis, D. Apostolakis, A. Tsagarakis, G. Kourakis, and E. Pavlakis, "A comparison of accuracy of 3 intraoral scanners: A single-blinded in vitro study," *J. Prosthet. Dent.*, vol. 124, no. 5, pp. 581–588, Nov. 2020, doi: 10.1016/J.PROSDENT.2019.10.023.
- [47] S. Koyama, H. Kato, T. Harata, and K. Sasaki, "A workflow for fabricating a hollow obturator by using 3D digital technologies," *J. Prosthet. Dent.*, vol. 123, no. 4, pp. 648–652, Apr. 2020, doi: 10.1016/J.PROSDENT.2019.05.020.
- [48] Y. low Wu and N. G. Schaaf, "Comparison of weight reduction in different designs of solid and hollow obturator prostheses," *J. Prosthet. Dent.*, vol. 62, no. 2, pp. 214–217, Aug. 1989, doi: 10.1016/0022-3913(89)90317-X.
- [49] A. N. Awad, S. H. Cho, M. J. Kesterke, and J. H. Chen, "Comparison of tensile bond strength of denture reline materials on denture bases fabricated with CAD-CAM technology," *J. Prosthet. Dent.*, Aug. 2021, doi: 10.1016/J.PROSDENT.2021.06.047.
- [50] M. Dartaguiette, M. Elbashti, P. Girardeau, F. Jacob, M. Laurentjoye, and A. Naveau, "Three-dimensional printed immediate surgical obturator before maxillectomy: A pilot study," *Int. J. Maxillofac. Prosthetics*, vol. 4, no. 1, pp. 18–24, May 2021, doi: 10.26629/IJMP.2021.04.
- [51] A. Fedorov *et al.*, "3D Slicer as an image computing platform for the Quantitative Imaging Network," *Magn. Reson. Imaging*, vol. 30, no. 9, pp. 1323–1341, Nov. 2012, doi: 10.1016/J.MRI.2012.05.001.
- [52] J. Wallner *et al.*, "Clinical evaluation of semi-automatic open-source algorithmic software segmentation of the mandibular bone: Practical feasibility and assessment of a new course of action," *PLoS One*, vol. 13, no. 5, May 2018, doi: 10.1371/JOURNAL.PONE.0196378.
- [53] M. Franaszek and G. S. Cheok, "Selection of fiducial locations and performance metrics for point-based rigid-body registration," *Precis. Eng.*, vol. 47, pp. 362–374, Jan. 2017, doi: 10.1016/J.PRECISIONENG.2016.09.010.
- [54] R. Marani, V. Renò, M. Nitti, T. D'Orazio, and E. Stella, "A Modified Iterative Closest Point Algorithm for 3D Point Cloud Registration," *Comput. Civ. Infrastruct. Eng.*, vol. 31, no. 7, pp. 515–534, Jul. 2016, doi: 10.1111/MICE.12184.
- [55] Formlabs, "Cupping blowout," 2022. https://support.formlabs.com/s/article/Cupping-Blowout?language=en_US.
- [56] J. V. Chen, A. B. C. Dang, and A. Dang, "Comparing cost and print time estimates for six commercially-available 3D printers obtained through slicing software for clinically relevant anatomical models," *3D Print. Med.*, vol. 7, no. 1, Dec. 2021, doi: 10.1186/S41205-020-00091-4.
- [57] T. Tasopoulos, G. Kouveliotis, G. Polyzois, and V. Karathanasi, "Fabrication of a 3D Printing Definitive Obturator Prosthesis: a Clinical Report," *Acta Stomatol. Croat.*, vol. 51, no. 1, p. 53, Mar. 2017, doi: 10.15644/ASC51/1/7.
- [58] A. Sieiškiewicz, T. Łysoń, Z. Mariak, and M. Rogowski, "[Neuronavigation in transnasal endoscopic paranasal sinuses and cranial base surgery: comparison of the optical and electromagnetic systems]," *Otolaryngol. Pol. = Polish Otolaryngol.*, vol. 63, no. 3, pp. 256–260, 2009, doi: 10.1016/S0030-6657(09)70118-0.
- [59] J. T. Deferm, J. Nijsink, F. Baan, L. Verhamme, G. Meijer, and T. Maal, "Soft tissue-based registration of intraoral scan with cone beam computed tomography scan," *Int. J. Oral Maxillofac. Surg.*, vol. 51, no. 2, pp. 263–268, Feb. 2022, doi: 10.1016/J.IJOM.2021.04.004.
- [60] N. Vosselman, H. H. Glas, B. J. Merema, J. Kraeima, H. Reintsema, and G. M. Raghoobar, "Three-Dimensional Guided Zygomatic Implant Placement after Maxillectomy," 2022.
- [61] A. Hassani, S. Shahmirzadi, and S. Saadat, "Applications of the Buccal Fat Pad in Oral and Maxillofacial Surgery," *A Textb. Adv. Oral Maxillofac. Surg. Vol. 3*, Aug. 2016, doi: 10.5772/63133.
- [62] T. Fernandes, J. C. Lobo, R. Castro, M. I. Oliveira, and P. M. Som, "Anatomy and pathology of the masticator space," *Insights Imaging*, vol. 4, no. 5, pp. 605–616, Oct. 2013, doi: 10.1007/S13244-013-0266-4/FIGURES/19.
- [63] M. Bayome, J. Hyun Park, and Y. A. Kook, "New three-dimensional cephalometric analyses among adults with a skeletal class I pattern and normal occlusion," *Korean J. Orthod.*, vol. 43, no. 2, pp. 62–73, Apr. 2013, doi: 10.4041/KJOD.2013.43.2.62.
- [64] G. R. J. Swennen, F. Schutysen, and J.-E. Hausamen, *Three-Dimensional Cephalometry*. Springer,

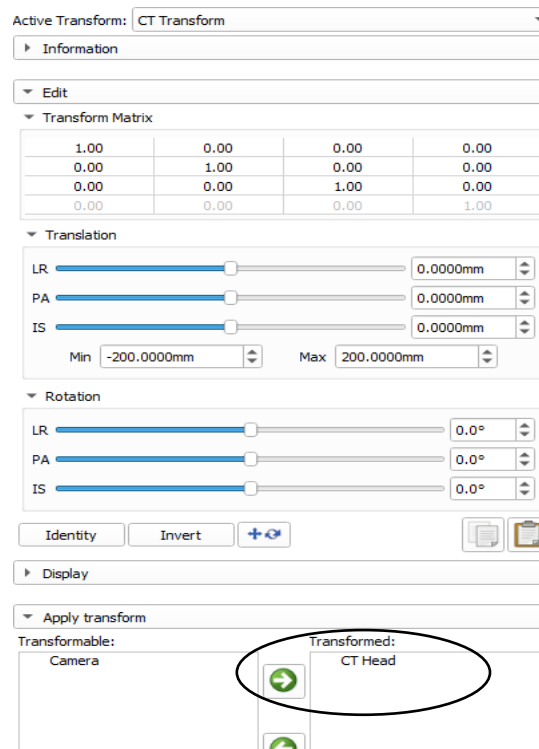
- 2006.
- [65] A. Reinke *et al.*, "Common Limitations of Image Processing Metrics: A Picture Story," vol. 1, no. 1, 2021, [Online]. Available: <http://arxiv.org/abs/2104.05642>.
- [66] O. U. Aydin *et al.*, "On the usage of average Hausdorff distance for segmentation performance assessment: hidden error when used for ranking," 2021, doi: 10.1186/s41747-020-00200-2.
- [67] O. U. Aydin *et al.*, "On the usage of average Hausdorff distance for segmentation performance assessment: hidden error when used for ranking," *Eur. Radiol. Exp.*, vol. 5, no. 1, Dec. 2021, doi: 10.1186/S41747-020-00200-2.
- [68] S. H. Tuna, F. Keyf, H. O. Gumus, and C. Uzun, "The Evaluation of Water Sorption/Solubility on Various Acrylic Resins," *Eur. J. Dent.*, vol. 2, no. 03, p. 191, Jul. 2008, doi: 10.1055/s-0039-1697377.
- [69] M. A. Mousa, J. Y. Abdullah, N. B. Jamayet, M. K. Alam, and A. Husein, "Biomechanical Stress in Obturator Prostheses: A Systematic Review of Finite Element Studies," *Biomed Res. Int.*, vol. 2021, 2021, doi: 10.1155/2021/6419774.
- [70] R. F. Villefort *et al.*, "Stress distribution on different bar materials in implant-retained palatal obturator," *PLoS One*, vol. 15, no. 10, Oct. 2020, doi: 10.1371/JOURNAL.PONE.0241589.
- [71] B. J. Goodacre, C. J. Goodacre, N. Z. Baba, and M. T. Kattadiyil, "Comparison of denture tooth movement between CAD-CAM and conventional fabrication techniques," *J. Prosthet. Dent.*, vol. 119, no. 1, pp. 108–115, Jan. 2018, doi: 10.1016/J.PROSDENT.2017.02.009.
- [72] F. A. Alshahrani *et al.*, "Impact of Polymerization Technique and ZrO₂ Nanoparticle Addition on the Fracture Load of Interim Implant-Supported Fixed Cantilevered Prostheses in Comparison to CAD/CAM Material," *Dent. J.*, vol. 10, no. 6, p. 102, Jun. 2022, doi: 10.3390/DJ10060102.
- [73] J. P. M. Tribst *et al.*, "Effect of different materials and undercut on the removal force and stress distribution in circumferential clasps during direct retainer action in removable partial dentures," *Dent. Mater.*, vol. 36, no. 2, pp. 179–186, Feb. 2020, doi: 10.1016/J.DENTAL.2019.11.022.
- [74] J. P. M. Tribst, A. M. de O. Dal Piva, M. A. Bottino, C. J. Kleverlaan, and J. H. Koolstra, "Mouthguard use and TMJ injury prevention with different occlusions: A three-dimensional finite element analysis," *Dent. Traumatol.*, vol. 36, no. 6, pp. 662–669, Dec. 2020, doi: 10.1111/EDT.12577.
- [75] J. P. M. Tribst, A. M. de Oliveira Dal Piva, A. L. S. Borges, V. A. Rodrigues, M. A. Bottino, and C. J. Kleverlaan, "Does the prosthesis weight matter? 3D finite element analysis of a fixed implant-supported prosthesis at different weights and implant numbers," *J. Adv. Prosthodont.*, vol. 12, no. 2, pp. 67–74, Apr. 2020, doi: 10.4047/JAP.2020.12.2.67.
- [76] H. S. Oh, Y. J. Lim, B. Kim, M. J. Kim, H. B. Kwon, and Y. W. Baek, "Influence of scanning-aid materials on the accuracy and time efficiency of intraoral scanners for full-arch digital scanning: An in vitro study," *Materials (Basel)*, vol. 14, no. 9, 2021, doi: 10.3390/ma14092340.
- [77] G. S. de Andrade *et al.*, "Impact of different complete coverage onlay preparation designs and the intraoral scanner on the accuracy of digital scans," *J. Prosthet. Dent.*, pp. 1–10, 2022, doi: 10.1016/j.prosdent.2022.05.001.
- [78] J. P. M. Tribst, A. M. de O. Dal Piva, and L. Kalman, "Stress Concentration of Hybrid Occlusal Splint-Mouthguard during a Simulated Maxillofacial Traumatic Impact: 3D-FEA," *Dent. J.*, vol. 10, no. 4, Apr. 2022, doi: 10.3390/DJ10040065.
- [79] Formlabs, "Material data sheet," 2013.
- [80] S. M. Chung, A. U. J. Yap, W. K. Koh, K. T. Tsai, and C. T. Lim, "Measurement of Poisson's ratio of dental composite restorative materials," *Biomaterials*, vol. 25, no. 13, pp. 2455–2460, 2004, doi: 10.1016/J.BIOMATERIALS.2003.09.029.
- [81] A. M. de O. Dal Piva, J. P. M. Tribst, R. O. de A. e. Souza, and A. L. S. Borges, "Influence of Alveolar Bone Loss and Cement Layer Thickness on the Biomechanical Behavior of Endodontically Treated Maxillary Incisors: A 3-dimensional Finite Element Analysis," *J. Endod.*, vol. 43, no. 5, pp. 791–795, May 2017, doi: 10.1016/J.JOEN.2016.11.020.
- [82] R. H. Sudhan, G. N. Chander, and K. V. Anitha, "Finite element stress analysis of Aramany class I maxillectomy defect with single- and two-piece closed bulb obturators," *Gerodontology*, vol. 38, no. 2, pp. 209–215, Jun. 2021, doi: 10.1111/GER.12518.
- [83] A. A. De Sousa and B. S. C. Mattos, "Finite element analysis of stability and functional stress with implant-supported maxillary obturator prostheses," *J. Prosthet. Dent.*, vol. 112, no. 6, pp. 1578–1584, Dec. 2014, doi: 10.1016/J.PROSDENT.2014.06.020.

- [84] "(PDF) Water Sorption and Solubility of Denture Base Resins-An Evaluation." https://www.researchgate.net/publication/283778598_Water_Sorption_and_Solubility_of_Denture_Base_Resins-An_Evaluation (accessed Aug. 19, 2022).
- [85] B. J. Goodacre, C. J. Goodacre, N. Z. Baba, and M. T. Kattadiyil, "Comparison of denture base adaptation between CAD-CAM and conventional fabrication techniques," *J. Prosthet. Dent.*, vol. 116, no. 2, pp. 249–256, 2016, doi: 10.1016/j.prosdent.2016.02.017.
- [86] H. J. Kim *et al.*, "A modified midfacial degloving approach for the treatment of unilateral paranasal sinus tumours," *J. Cranio-Maxillofacial Surg.*, vol. 39, no. 4, pp. 284–288, Jun. 2011, doi: 10.1016/J.JCMS.2010.06.006.
- [87] Mitra Geeti Vajdi, *Illustrated Manual of Oral and Maxillofacial Surgery*. 2009.
- [88] R. G. West and D. VeyVoda, "Definitive Obturator - Dentist In Oyster Bay, NY | The Oyster Bay Family Dentists," 2022. <https://www.oysterbaydentists.com/definitive-obturator>.
- [89] A. Dentistry, "The 3Shape Trios Intraoral Scanner - Advanced Dentistry," 2018. <https://www.advanceddentistrypdx.com/the-3d-biocad-trios-intraoral-scanner/>.

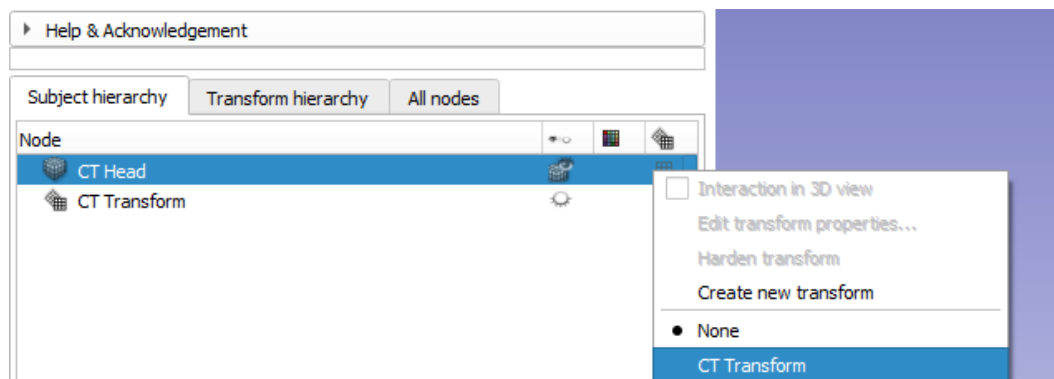
Appendix

A1: Protocol segmentation steps in Slicer

1. Load in your files. If desired, rename your files by double clicking on the name in . Make sure that the Maxilla is aligned straight in the CT if so, skip step 2 and 3.
2. Go to **Select**  **Active Transform > Create new Linear Transform as >** Fill in name. Set CT to '**Transformed**' node and use the sliders to translate and rotate the CT.



3. Go back to **Data**. Right click on the  next to the CT to switch the transform on and off. After the transform, repeat this step and select **Harden transform**.



Example:

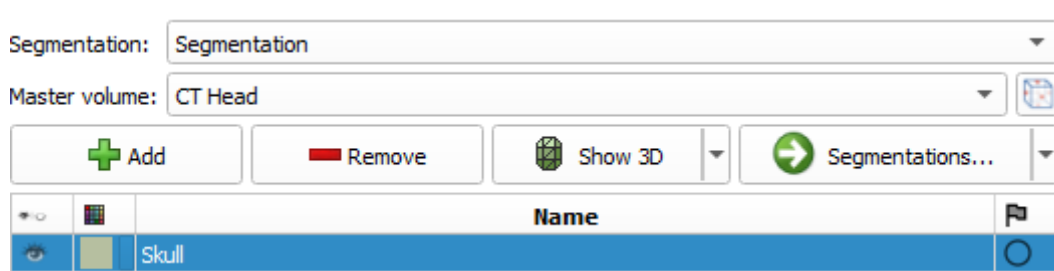
Before transform:



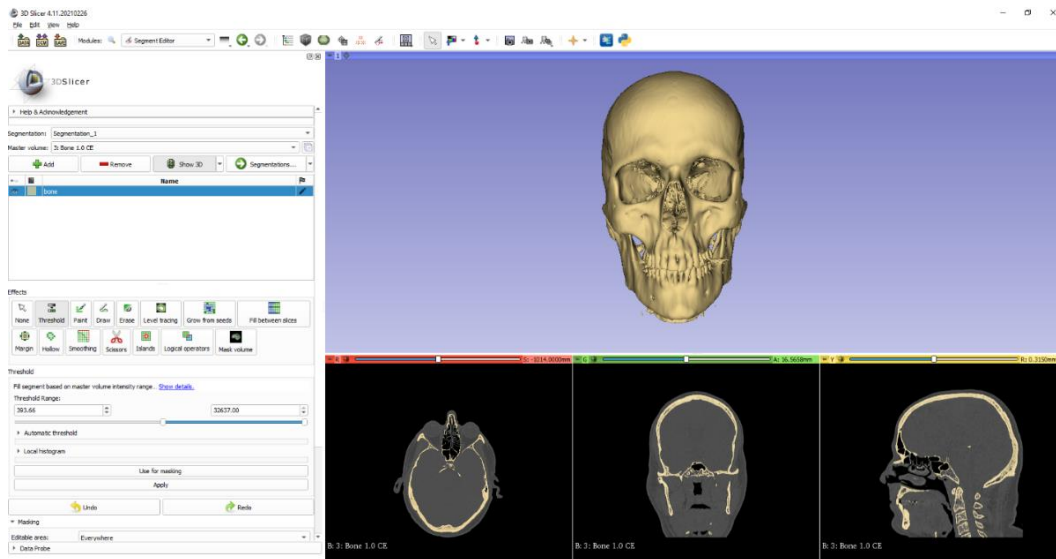
After transform:



4. Go to  Segment Editor and segment the skull. Select the CT as **Master Volume** > press **Add**. Double click on the segment name and color to change them. Go to **Threshold** and set the range to the threshold of the bones. Press **Apply**.

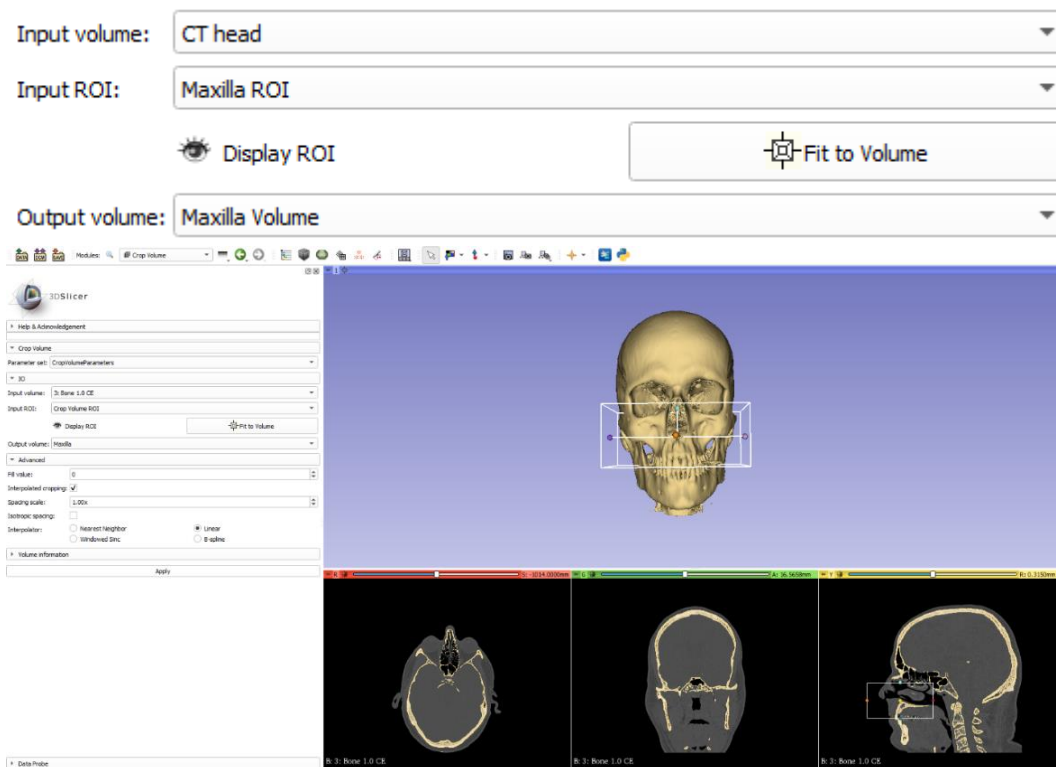


5. Press **Show 3D** to have a 3D visualization of the skull. Use the buttons  to center to the 3D view or to quickly adjust the direction of the view. If needed, remove scatter or small segment parts by combining with the other segment editor effects such as **Scissors & Islands**.



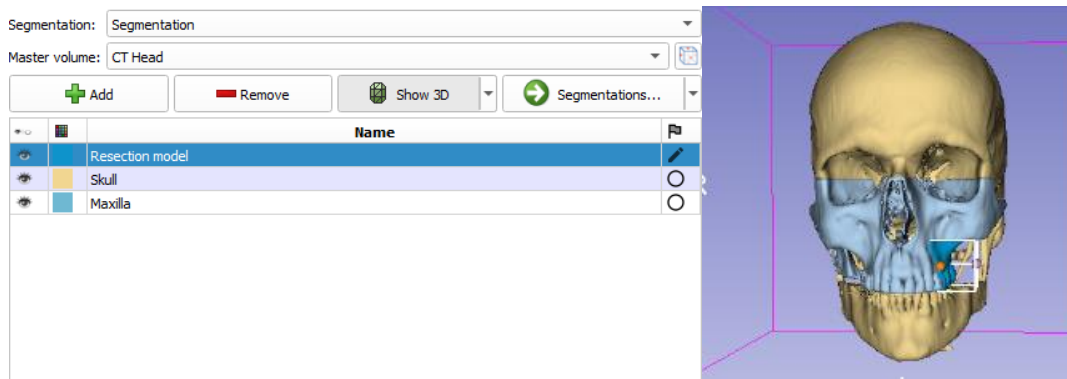
6. Go to Converters >  **Crop Volume**. Select as Input Volume the CT and create a new annotation ROI as Input ROI. Swipe the colored dots of the ROI to the range of the maxilla. Create a new Output Volume as 'Maxilla Volume'. Press Apply.

Example:

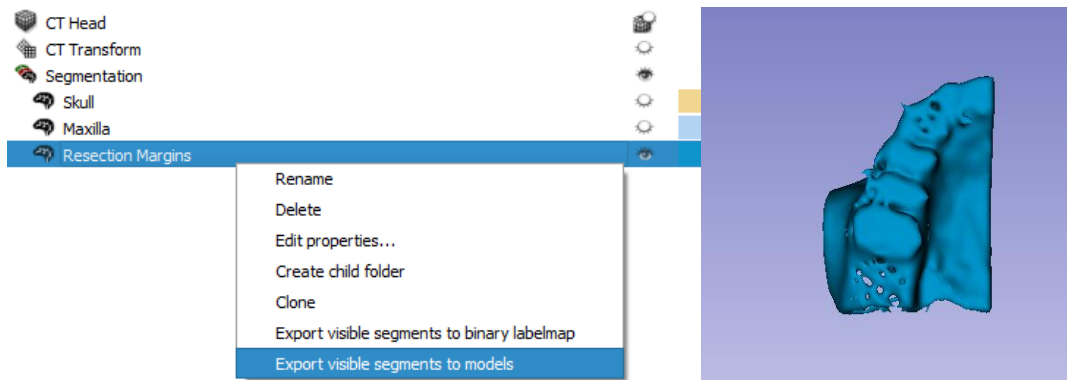


7. Go back to **Segment Editor** to segment the Maxilla. Select the Maxilla Volume as **Master Volume** > press **Add**. Go to **Threshold** and press **Apply**. Repeat step 5.

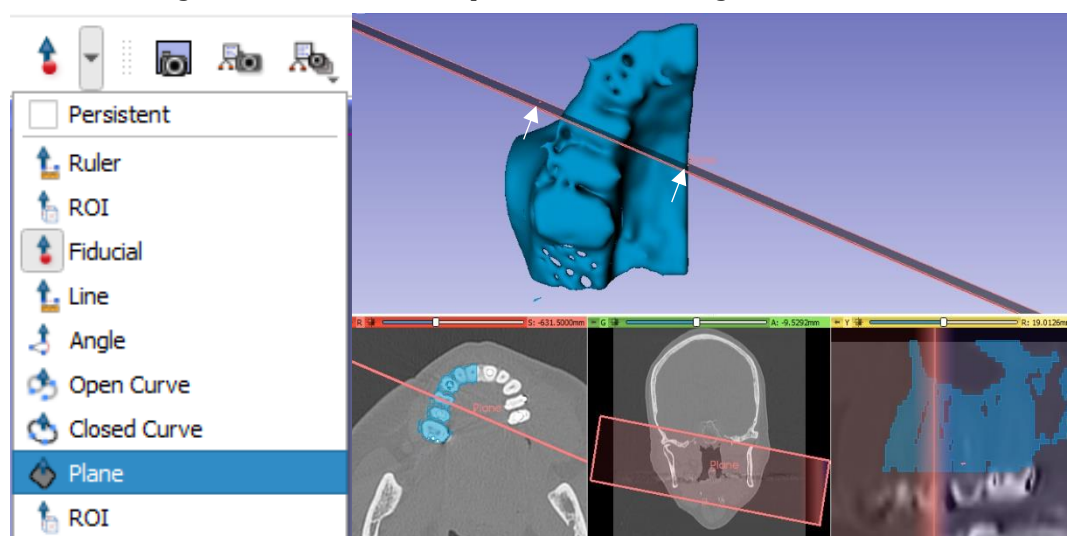
8. Repeat step 6 and 7 to create a new ROI for the resection margins. Discuss the range of the ROI with the head- and neck surgeon. This will be the horizontal and vertical resection margins. After the discussion, crop a new **Output Volume** as 'Resection Volume'. Next, repeat step 7 to segment the resection margins.



9. Go to Data. Make the resection segment visible and other segments non-visible. Right-click on the resection segment and click on Export visible segments to models. A model of the resection margin is created.



10. Go to the arrow next to **Fiducial** > select **Plane**. Create a plane in the oblique resection direction by selecting three points. The first two points (highlighted with a white arrow in the image below), are set in the oblique direction that is discussed together with the surgeon. The final point is used to determine the height of the plane. Use the one-dimensional views below your model to determine the height and create a vertical plane in the same angle as the CT.



11. Go to **Surface Models** >  and select **Plane Cut** . Select your resection model as **Model node**, your oblique plane as **Plane Node**, and create new models as **Clipped output models**. Press **Apply**. Check in your data which side (positive or negative) is the correct output model.

▼ Input nodes

Model node:

Plane node [1]:

Plane node [2]:

▼ Parameters

Cap surface:

Operation type:

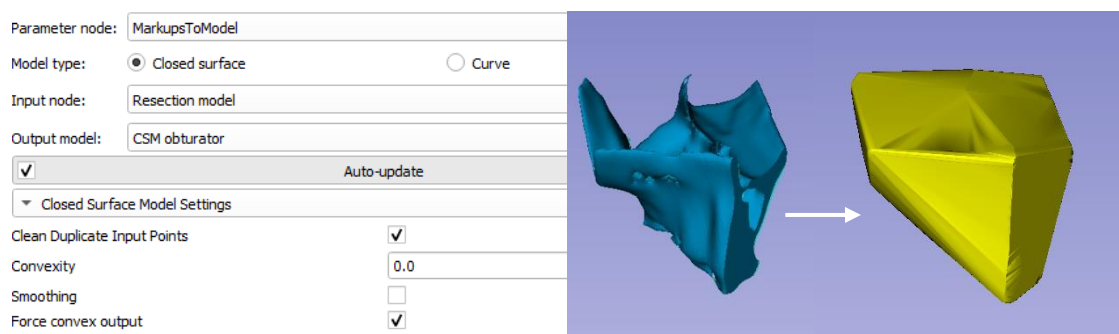
▼ Output nodes

Clipped output model (positive side):

Clipped output model (negative side):

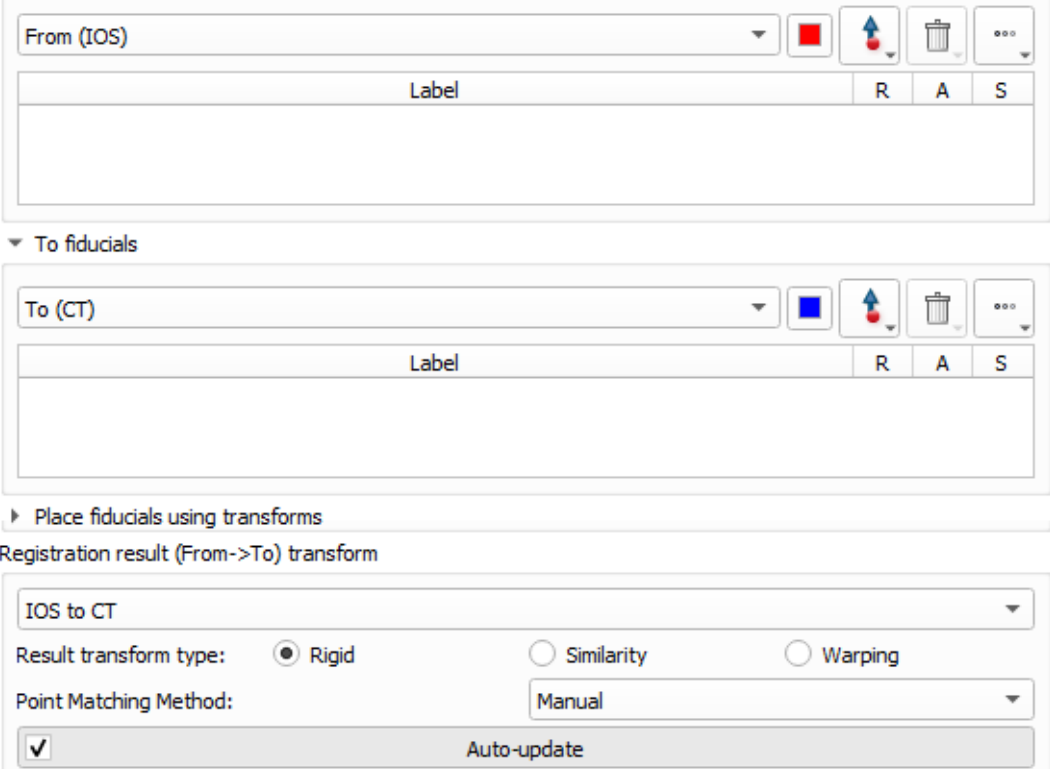
12. Your resection bone model is now completed. If alterations are needed, or navigation will be used, go to **Data** > right click on the model > **Convert model to segmentation node**.
13. For the final step, make sure that you downloaded the 'Slicer IGT' and 'MarksupToModel' extension.

Go to **IGT** >  and select your finished resection model as **Input node**. As **Output model**, create a new model. After a few seconds, a CSM design appears, set the smoothing off for a more precise shape.



14. Now it is time to register the baseplate. Load the intraoral scan in Slicer.

Go to **IGT** >  and create new 'From' and 'To' fiducial registration points, rename them if desired. Create a new linear transform as 'IOS to CT', for example.



From (IOS)

Label	R	A	S

To fiducials

To (CT)

Label	R	A	S

Place fiducials using transforms

Registration result (From->To) transform

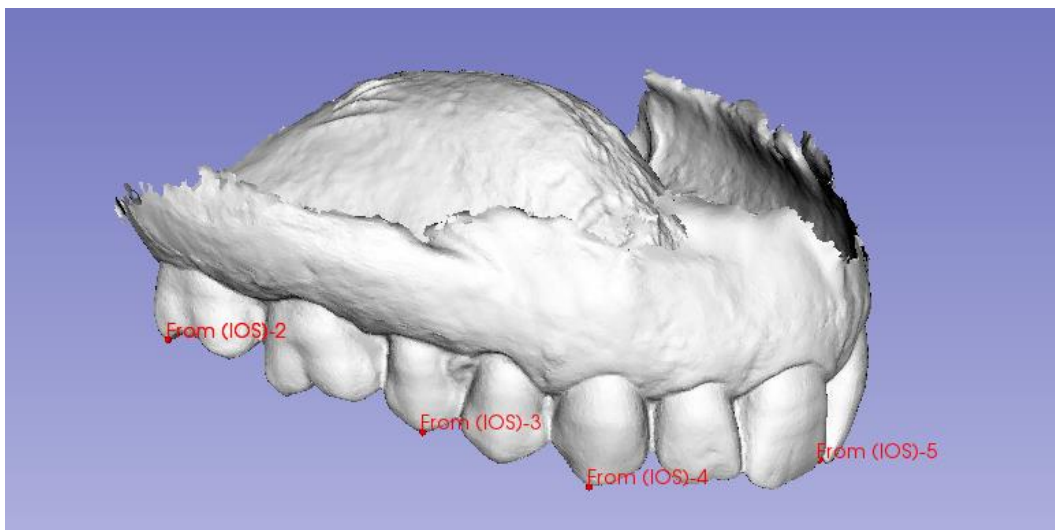
IOS to CT

Result transform type: Rigid Similarity Warping

Point Matching Method: Manual

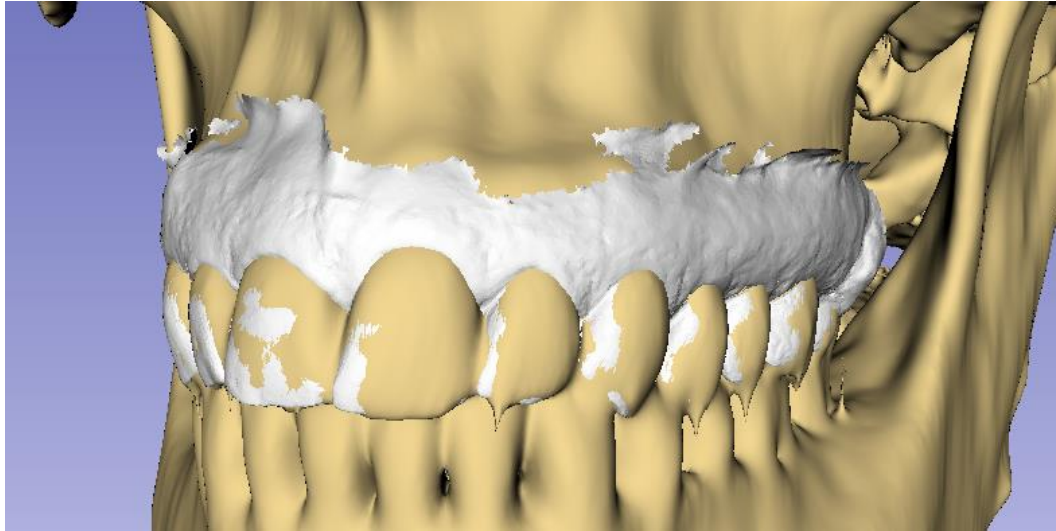
Auto-update

15. Set the fiducial points at the identical locations on the segmented CT skull and IOS. Chose notable features at different areas on the teeth, for example at the most posterior locations as seen in the image below:



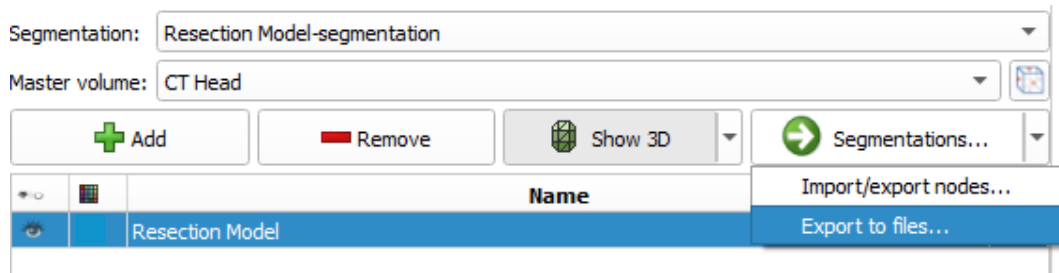
The Fiducial Registration Wizard extension automatically calculates the RMS if all the points are set, the error should be <math><1\text{mm}</math>.

16. Repeat step 3: Go back to **Data**. Right click on the  next to the intraoral scan and transform. To harden the transform, select **Harden transform**. The intraoral scan is now registered, which should look like the image below for example:

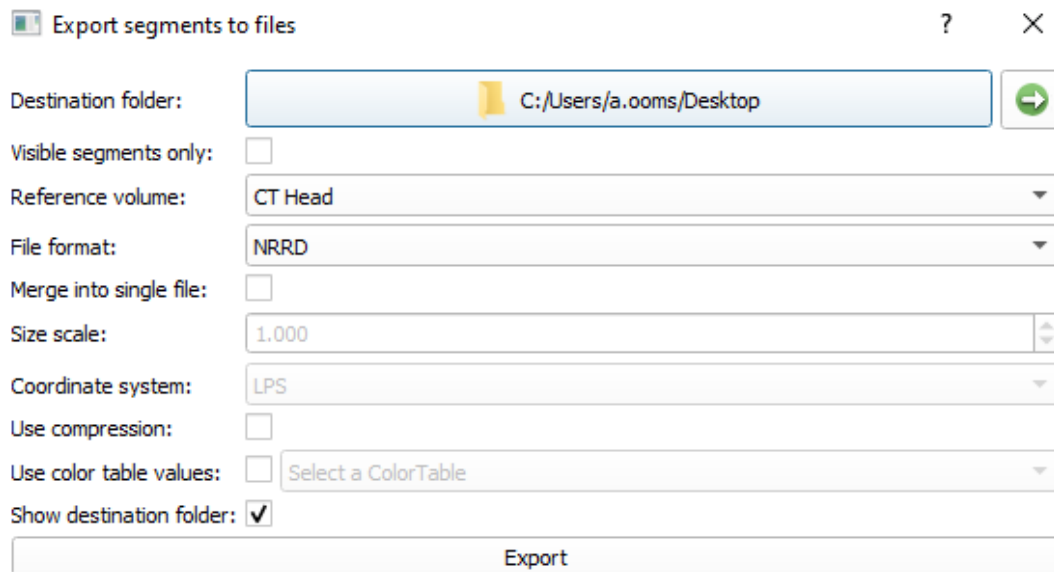


A2: Protocol Metronics navigation preparation steps in Slicer

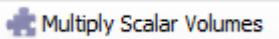
1. Go to **Data** > Select your final 'Resection Model. STL' > right click on the model > **Convert model to segmentation node**.
2. Go to  > select the correct **Segmentation** > select the resection bone segment > click right next to **Segmentations** > press '**Export to files..**'

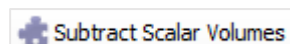


3. The '**Export segments to files**' pop-up appears, select your **Destination folder**, set the CT as **Reference Volume** and select NRRD as **File Format**. Press **Export**.



4. Import the exported resection NRRD in your Slicer.

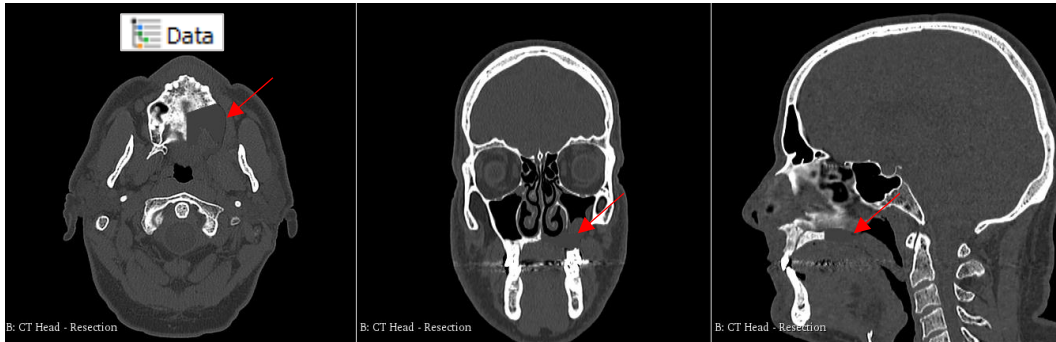
Go to **Filtering** > **Arithmetic** >  and select your CT as '**Input Volume 1**' and your resection volume as '**Input Volume 2**'. Create a new output file as '**Output Volume**', for example: Multiplied Volume. Press **Apply**.



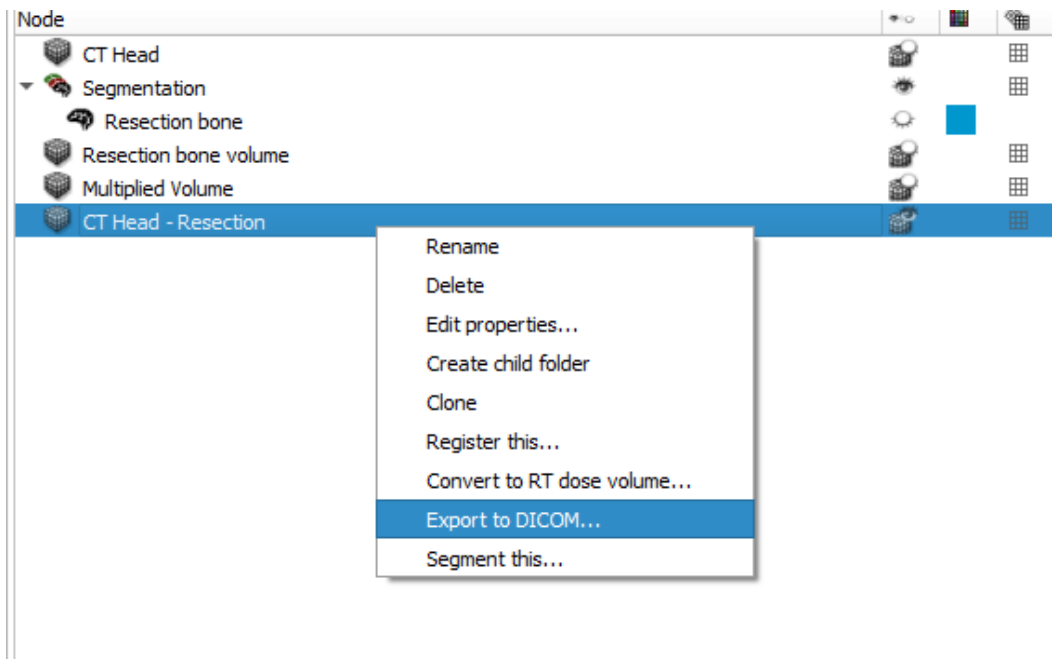
- Go to **Filtering > Arithmetic >** and select your CT as **Input Volume 1** and your multiplied volume as **Input Volume 2**. Create a new output file as **Output Volume**, for example: **CT Head - Resection**. Press **Apply**.

Input Volume 1	CT Head
Input Volume 2	Multiplied Volume
Output Volume	CT Head - Resection

- The output volume contains the original CT with the resection margins subtracted from the CT in grey. Repeat step 4 if you desire the resection area to be more darker.



- Go to > right click on the output volume > press **Export to DICOM** and select the desired folder. The DICOM file can be exported and loaded into the Medtronic with an USB flash drive.



B1: Python scripted resection segmentation steps in Slicer

- Load in the CT data.
- Go to View > Python Interactor (ctrl + 3)
- Copy (ctrl + c) - paste (ctrl + v) the code lines displayed **per block** into the Python interactor

Step 1: Transform (if needed)

```
#Create transform
# Create transform
masterVolumeNode = getNode("CT Head") #fill in name of CT scan #fill in name of CT scan
transformNode = slicer.mrmlScene.AddNode(slicer.vtkMRMLTransformNode())
transformNode.CreateDefaultDisplayNodes()
slicer.util.selectModule("Transforms")
transform = vtk.vtkTransform()
print('rotate or transform')

# Transform CT
transformNode.ApplyTransform(transform)
masterVolumeNode.SetAndObserveTransformNodeID(transformNode.GetID())
```

Step 2: Segment skull

```
#Create segmentation node
masterVolumeNode = getNode("CT Head") #fill in name of CT scan
segmentationNode = slicer.mrmlScene.AddNewNodeByClass("vtkMRMLSegmentationNode")
segmentationNode.CreateDefaultDisplayNodes()
segmentationNode.SetReferenceImageGeometryParameterFromVolumeNode(masterVolumeNode)
addedSegmentID = segmentationNode.GetSegmentation().AddEmptySegment("Skull")
segmentation = getNode('Segmentation')
segmentID = 'Skull' #name of segmentation

# Segment color
segment = segmentation.GetSegmentation().GetSegment(segmentID)
segment.SetColor(241/255, 214/255, 145/255) # bone color
slicer.util.selectModule("SegmentEditor")

# Create segment editor to get access to effects
segmentEditorWidget = slicer.qMRMLSegmentEditorWidget()
segmentEditorWidget.setMRMLScene(slicer.mrmlScene)
segmentEditorNode = slicer.mrmlScene.AddNewNodeByClass("vtkMRMLSegmentEditorNode")
segmentEditorWidget.setMRMLSegmentEditorNode(segmentEditorNode)
segmentEditorWidget.setSegmentationNode(segmentationNode)
segmentEditorWidget.setMasterVolumeNode(masterVolumeNode)

# Thresholding
segmentEditorWidget.setActiveEffectByName("Threshold")
effect = segmentEditorWidget.activeEffect()
effect.setParameter("MinimumThreshold", "400") #Change if needed
effect.setParameter("MaximumThreshold", "3000")
effect.self().onApply()

#Keep largest island to remove noise
segmentEditorWidget.setActiveEffectByName("Islands")
effect = segmentEditorWidget.activeEffect()
effect.setParameter("Operation", "KEEP_LARGEST_ISLAND")
effect.self().onApply()
segmentEditorWidget.setActiveEffectByName("None")
```

#2 Segmentation skull: Visualize in 3D

```
print ('Please be patient, the segmentation is loading and will appear when it is finished')
segmentationNode.CreateClosedSurfaceRepresentation()

#set orientation on segmentation
layoutManager = slicer.app.layoutManager()
threeDWidget = layoutManager.threeDWidget(0)
threeDView = threeDWidget.threeDView()
threeDView.resetFocalPoint()
```

Step 3: Segment Maxilla**#Create ROI**

```
segmentationNode = getNode("Segmentation")
```

Compute bounding boxes

```
import SegmentStatistics
segStatLogic = SegmentStatistics.SegmentStatisticsLogic()
segStatLogic.getParameterNode().SetParameter("Segmentation", segmentationNode.GetID())
segStatLogic.getParameterNode().SetParameter("LabelmapSegmentStatisticsPlugin.obb_origin_ras.enabled",str(True))
segStatLogic.getParameterNode().SetParameter("LabelmapSegmentStatisticsPlugin.obb_diameter_mm.enabled",str(True))
segStatLogic.getParameterNode().SetParameter("LabelmapSegmentStatisticsPlugin.obb_direction_ras_x.enabled",str(True))
segStatLogic.getParameterNode().SetParameter("LabelmapSegmentStatisticsPlugin.obb_direction_ras_y.enabled",str(True))
segStatLogic.getParameterNode().SetParameter("LabelmapSegmentStatisticsPlugin.obb_direction_ras_z.enabled",str(True))
segStatLogic.computeStatistics()
stats = segStatLogic.getStatistics()
```

Draw ROI for each oriented bounding box

```
import numpy as np
for segmentId in stats["SegmentIDs"]:
    # Get bounding box
    obb_origin_ras = np.array(stats[segmentId,"LabelmapSegmentStatisticsPlugin.obb_origin_ras"])
    obb_diameter_mm = np.array(stats[segmentId,"LabelmapSegmentStatisticsPlugin.obb_diameter_mm"])
    obb_direction_ras_x = np.array(stats[segmentId,"LabelmapSegmentStatisticsPlugin.obb_direction_ras_x"])
    obb_direction_ras_y = np.array(stats[segmentId,"LabelmapSegmentStatisticsPlugin.obb_direction_ras_y"])
    obb_direction_ras_z = np.array(stats[segmentId,"LabelmapSegmentStatisticsPlugin.obb_direction_ras_z"])
    # Create ROI
    segment = segmentationNode.GetSegmentation().GetSegment(segmentId)
    roi=slicer.mrmlScene.AddNewNodeByClass("vtkMRMLAnnotationROINode")
    roi.SetName("MaxillaROI")
    roi.SetXYZ(0.0, 0.0, 0.0)
    roi.SetRadiusXYZ(*(0.5*obb_diameter_mm))
    # Position and orient ROI using a transform
    obb_center_ras = obb_origin_ras+0.5*(obb_diameter_mm[0] * obb_direction_ras_x +
    obb_diameter_mm[1] * obb_direction_ras_y + obb_diameter_mm[2] * obb_direction_ras_z)
    boundingBoxToRasTransform = np.row_stack((np.column_stack((obb_direction_ras_x,
    obb_direction_ras_y, obb_direction_ras_z, obb_center_ras)), (0, 0, 0, 1)))
    boundingBoxToRasTransformMatrix = slicer.util.vtkMatrixFromArray(boundingBoxToRasTransform)
    transformNode = slicer.mrmlScene.AddNewNodeByClass("vtkMRMLTransformNode")
    transformNode.SetAndObserveMatrixTransformToParent(boundingBoxToRasTransformMatrix)
```

<pre>roi.SetAndObserveTransformNodeID(transformNode.GetID()) Set ROI on the maxilla before continuing with the next step.. #Cropp Volume to Maxilla masterVolumeNode = getNode("CT Head") #fill in name of CT scan ROINode = roi ROINode.SetName('MaxillaROI') #This cell crops the volume by the selected maxilla ROI MaxillaVolumeNode = slicer.vtkMRMLScalarVolumeNode() MaxillaVolumeNode.SetName('MaxillaVolume') slicer.mrmlScene.AddNode(MaxillaVolumeNode) cropVolumeLogic = slicer.modules.cropvolume.logic() cropVolumeParameterNode = slicer.vtkMRMLCropVolumeParametersNode() cropVolumeParameterNode.SetROINodeID(roi.GetID()) cropVolumeParameterNode.SetInputVolumeNodeID(masterVolumeNode.GetID()) cropVolumeParameterNode.SetOutputVolumeNodeID(MaxillaVolumeNode.GetID()) cropVolumeParameterNode.SetVoxelBased(True) cropVolumeLogic.Apply(cropVolumeParameterNode) croppedVolume = slicer.mrmlScene.GetNodeByID(.GetOutputVolumeNodeID())</pre>
<pre># Segment Maxilla # Create segmentation maxilla slicer.util.selectModule("SegmentEditor") segmentationNode.SetReferenceImageGeometryParameterFromVolumeNode(MaxillaVolumeNode) addedSegmentID = segmentationNode.GetSegmentation().AddEmptySegment("Maxilla") segmentation = getNode('Segmentation') segmentID = 'Maxilla' # Segment color (blue) segment = segmentation.GetSegmentation().GetSegment(segmentID) segment.SetColor(111/255 , 184/225, 210/225) # blue color #select maxilla segment with the maxillaROI segmentEditorNode.SetSelectedSegmentID(addedSegmentID) segmentEditorWidget.setMasterVolumeNode(MaxillaVolumeNode) #Threshold Maxilla segmentation slicer.util.selectModule("SegmentEditor") segmentEditorWidget.setActiveEffectByName("Threshold") effect = segmentEditorWidget.activeEffect() effect.setParameter("MinimumThreshold","400") #Change if needed effect.setParameter("MaximumThreshold","3000") effect.self().onApply() #Keep largest island to remove noise + mandibula segmentEditorWidget.setActiveEffectByName("Islands") effect = segmentEditorWidget.activeEffect() effect.setParameter("Operation","KEEP_LARGEST_ISLAND") effect.self().onApply() segmentEditorWidget.setActiveEffectByName("None") #set orientation on segmentation layoutManager = slicer.app.layoutManager() threeDWidget = layoutManager.threeDWidget(0) threeDView = threeDWidget.threeDView() threeDView.resetFocalPoint()</pre>

Discuss and set ROI on the resection margin together with head-neck surgeon before continuing with the next step.

Step 3: Segment Resection

```

ROINode = roi
ROINode.SetName('ResectionROI')

#Cropp Volume to Resection
ResectionVolumeNode = slicer.vtkMRMLScalarVolumeNode()
ResectionVolumeNode.SetName('ResectionVolume')
slicer.mrmlScene.AddNode(ResectionVolumeNode)
cropVolumeLogic = slicer.modules.cropvolume.logic()
cropVolumeParameterNode = slicer.vtkMRMLCropVolumeParametersNode()
cropVolumeParameterNode.SetROINodeId(roi.GetID())
cropVolumeParameterNode.SetInputVolumeNodeId(masterVolumeNode.GetID())
cropVolumeParameterNode.SetOutputVolumeNodeId(ResectionVolumeNode.GetID())
cropVolumeParameterNode.SetVoxelBased(True)
cropVolumeLogic.Apply(cropVolumeParameterNode)
croppedVolume = slicer.mrmlScene.GetNodeByID(cropVolumeParameterNode.GetOutputVolumeNodeId())

# Create resection segment
slicer.util.selectModule("SegmentEditor")
segmentationNode.SetReferenceImageGeometryParameterFromVolumeNode(ResectionVolumeNode)
addedSegmentID = segmentationNode.GetSegmentation().AddEmptySegment("Resectionbone")
segmentation = getNode('Segmentation')
segmentID = 'Resectionbone'

# Segment color (dark blue)
segment = segmentation.GetSegmentation().GetSegment(segmentID)
segment.SetColor(0/255 , 151/225, 206/225) # dark blue color

#select resection segment with the resectionROI
segmentEditorNode.SetSelectedSegmentID(addedSegmentID)
segmentEditorWidget.setMasterVolumeNode(ResectionVolumeNode)

#Threshold resection
print ('Please wait, the segmentation is loading and will appear when it is finished')
slicer.util.selectModule("SegmentEditor")
segmentEditorWidget.setActiveEffectByName("Threshold")
effect = segmentEditorWidget.activeEffect()
effect.setParameter("MinimumThreshold","400") #Change if needed
effect.setParameter("MaximumThreshold","3000")
effect.self().onApply()

#Keep largest island to remove noise + mandibula
segmentEditorWidget.setActiveEffectByName("Islands")
effect = segmentEditorWidget.activeEffect()
effect.setParameter("Operation","KEEP_LARGEST_ISLAND")
effect.self().onApply()
segmentEditorWidget.setActiveEffectByName("None")

#set orientation on segmentation

```

```

layoutManager = slicer.app.layoutManager()
threeDWidget = layoutManager.threeDWidget(0)
threeDView = threeDWidget.threeDView()
threeDView.resetFocalPoint()

roiNode = roi
roiNode.SetDisplayVisibility(0)

```

Step 4: Plane cut resection model

```

#Hide all segments except resection
displayNode = segmentationNode.GetDisplayNode()
displayNode.SetAllSegmentsVisibility(False) # Hide all segments
displayNode.SetSegmentVisibility('Resectionbone', True) # Show specific segment

#Set Markuppoints
w=slicer.qSlicerMarkupsPlaceWidget()
w.setMRMLScene(slicer.mrmlScene)
markupsNodeID = slicer.modules.markups.logic().AddNewFiducialNode()
w.setCurrentNode(slicer.mrmlScene.GetNodeByID(markupsNodeID))

# Show buttons
w.buttonsVisible=True
w.placeButton().show()
w.show()

#Create markupsplane
pointListNode = slicer.util.getNode("F")
planeNode = slicer.mrmlScene.AddNewNodeByClass('vtkMRMLMarkupsPlaneNode', 'Plane')
for cpIdx in range(3):
    pos = vtk.vtkVector3d()
    pointListNode.GetNthControlPointPositionWorld(cpIdx, pos)
    planeNode.AddControlPointWorld(pos)

planeNode.SetDisplayVisibility(1)

#export segments to models
segmentationNode = getNode("Segmentation")
shNode = slicer.mrmlScene.GetSubjectHierarchyNode()
exportFolderItemId = shNode.CreateFolderItem(shNode.GetSceneItemId(),
"Segment_models")
slicer.modules.segmentations.logic().ExportAllSegmentsToModels(segmentationNode,
exportFolderItemId)

#Remove additional models
slicer.mrmlScene.RemoveNode(inputmodelNode)
Skull = getNode('Skull'); slicer.mrmlScene.RemoveNode(Skull)
Maxilla = getNode('Maxilla'); slicer.mrmlScene.RemoveNode(Maxilla)

#Define models
inputmodelNode=slicer.util.getNode("Resectionbone")
inputPlaneNode=slicer.util.getNode("Plane")
OutputPositiveModel= slicer.mrmlScene.AddNewNodeByClass("vtkMRMLModelNode")
OutputPositiveModel.SetName('Resectionbone_green')
OutputNegativeModel= slicer.mrmlScene.AddNewNodeByClass("vtkMRMLModelNode")
OutputNegativeModel.SetName('Resectionbone_blue')

```

#Plane cut using dynamic modeler

```

dynamicModelerNode
slicer.mrmlScene.AddNewNodeByClass("vtkMRMLDynamicModelerNode")
dynamicModelerNode.SetToolName("Plane cut")
dynamicModelerNode.SetNodeReferenceID("PlaneCut.InputModel", inputmodelNode.GetID())
dynamicModelerNode.SetNodeReferenceID("PlaneCut.InputPlane", inputPlaneNode.GetID())
dynamicModelerNode.SetNodeReferenceID("PlaneCut.OutputPositiveModel",
OutputPositiveModel.GetID())
dynamicModelerNode.SetNodeReferenceID("PlaneCut.OutputNegativeModel",
OutputNegativeModel.GetID())
slicer.modules.dynamicmodeler.logic().RunDynamicModelerTool(dynamicModelerNode)

```

#Set color of new models

```

Green = getNode('Resectionbone_green')
Green.GetDisplayNode().SetColor(15/255, 233/225, 149/225) # green color
Blue = getNode('Resectionbone_blue')
Blue.GetDisplayNode().SetColor(0/255, 151/225, 206/225) # dark blue color

```

B2: Python scripted Metronics navigation steps for 3D Slicer

- Load in the CT data with the resection bone segmentation
- Go to View > Python Interactor (ctrl + 3)
- Copy (ctrl + c) - paste (ctrl + v) the code lines displayed **per block** into the Python interactor.

#Navigation step 1: Create labelmap of resection bone

```
#Skip this step if you already have a .nrrd volume of the segment
segmentNames = ["Resectionbone"]

segmentationNode = getNode('Segmentation')
labelmapVolumeNode = slicer.mrmlScene.AddNewNodeByClass('vtkMRMLLabelMapVolumeNode')
labelmapVolumeNode.SetName("Resection_LabelMap")
referenceVolumeNode = slicer.mrmlScene.GetFirstNodeByClass('vtkMRMLScalarVolumeNode')
for segmentName in segmentNames:
    segmentIds = vtk.vtkStringArray()
    segmentId = segmentationNode.GetSegmentation().GetSegmentIdBySegmentName(segmentName)
    segmentIds.InsertNextValue(segmentId)

slicer.vtkSlicerSegmentationsModuleLogic.ExportSegmentsToLabelmapNode(segmentationNode,
segmentIds, labelmapVolumeNode, referenceVolumeNode)
```

#Navigation step 2: Multiply scalar volumes

```
vol_1=slicer.util.getNode('bones') #fill in name of CT scan
vol_2=slicer.util.getNode('Resection_LabelMap') #or fill in name of nrrd volume of the segment
a = slicer.util.arrayFromVolume(vol_1)
b = slicer.util.arrayFromVolume(vol_2)
c = a * b

volumeNode_result = slicer.modules.volumes.logic().CloneVolume(vol_1, 'Multiply_volume')
slicer.util.updateVolumeFromArray(volumeNode_result, c)
setSliceViewerLayers(background=volumeNode_result)
```

#Navigation step 3: Subtract scalar volumes

```
vol_1=slicer.util.getNode('bones') #fill in name of CT scan
vol_2=slicer.util.getNode('Multiply_volume')
a = slicer.util.arrayFromVolume(vol_1)
b = slicer.util.arrayFromVolume(vol_2)
c = a - (1.5*b) #1.5 to get a dark grey subtraction, you can in- or decrease the amount of subtraction.
volumeNode_result = slicer.modules.volumes.logic().CloneVolume(vol_1, 'Substract_volume')
slicer.util.updateVolumeFromArray(volumeNode_result, c)
setSliceViewerLayers(background=volumeNode_result)
```

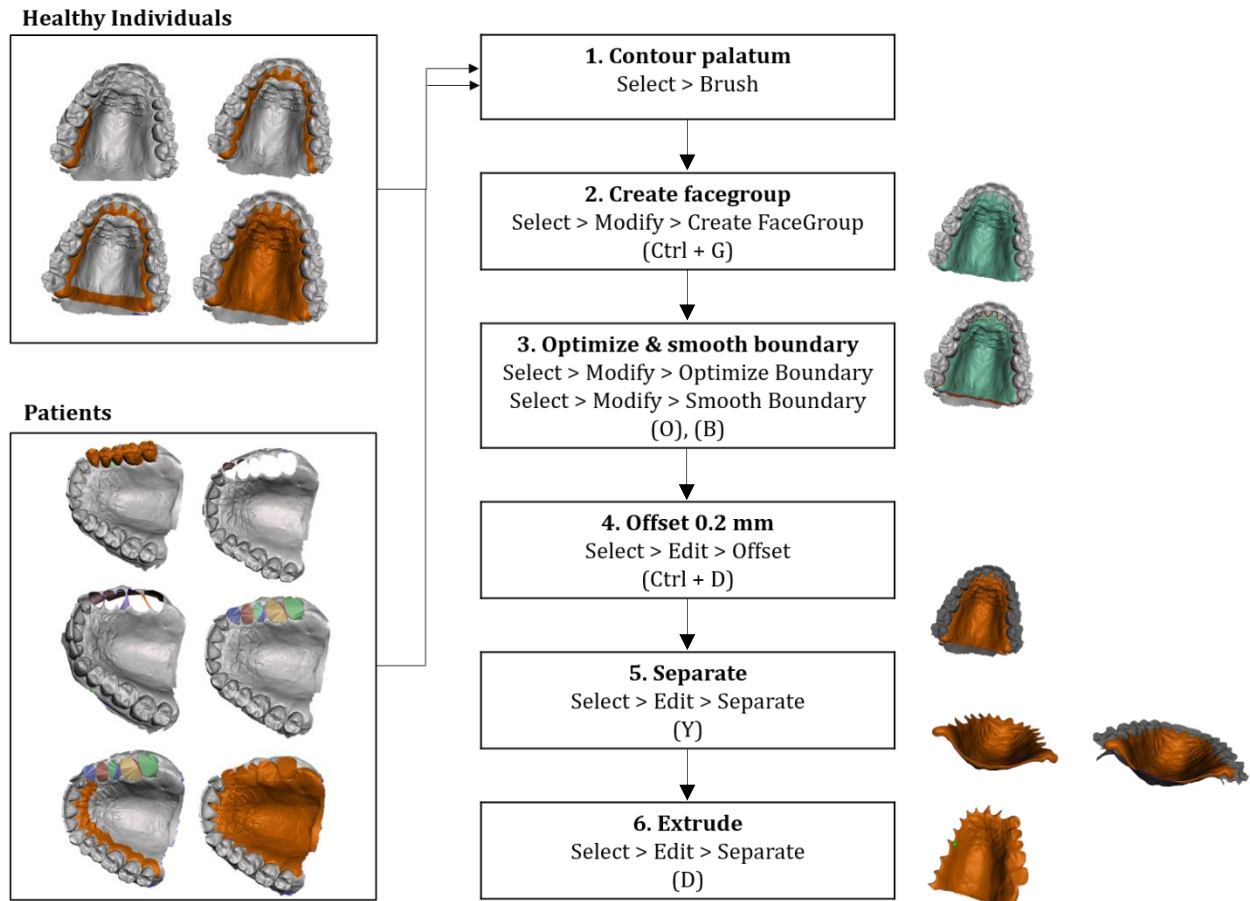
#Navigation step 4: Eport volume as dicom

```
volumeNode = getNode("Substracted_volume")
outputFolder = '.' # fill in output folder

# Create patient and study and put the volume under the study
shNode = slicer.vtkMRMLSubjectHierarchyNode.GetSubjectHierarchyNode(slicer.mrmlScene)
volumeShItemID = shNode.GetItemByDataNode(volumeNode)
shNode.SetItemParent(volumeShItemID, studyItemID)
```

```
import DICOMScalarVolumePlugin
exporter = DICOMScalarVolumePlugin.DICOMScalarVolumePluginClass()
exportables = exporter.examineForExport(volumeShItemID)
for exp in exportables:
    exp.directory = outputFolder
exporter.export(exportables)
```

C: Protocol baseplate design in Autodesk Meshmixer



D: Final designs in Autodesk Meshmixer

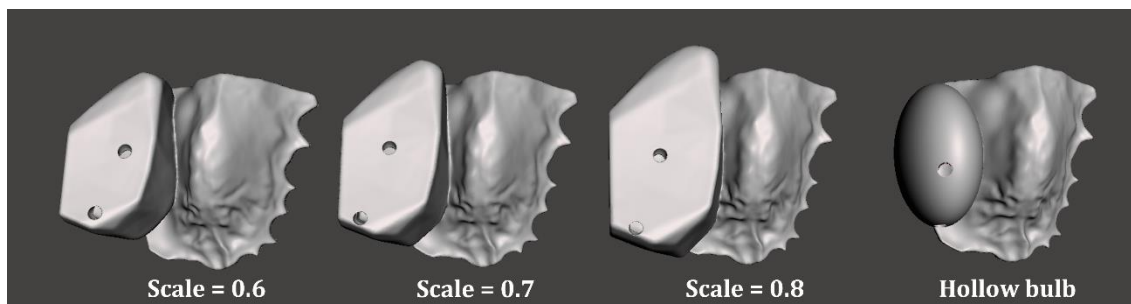


Figure D.1. Different scaled closed surface model (CSM) obturator designs (1-3), and the hollow bulb design (4) in Autodesk Meshmixer.

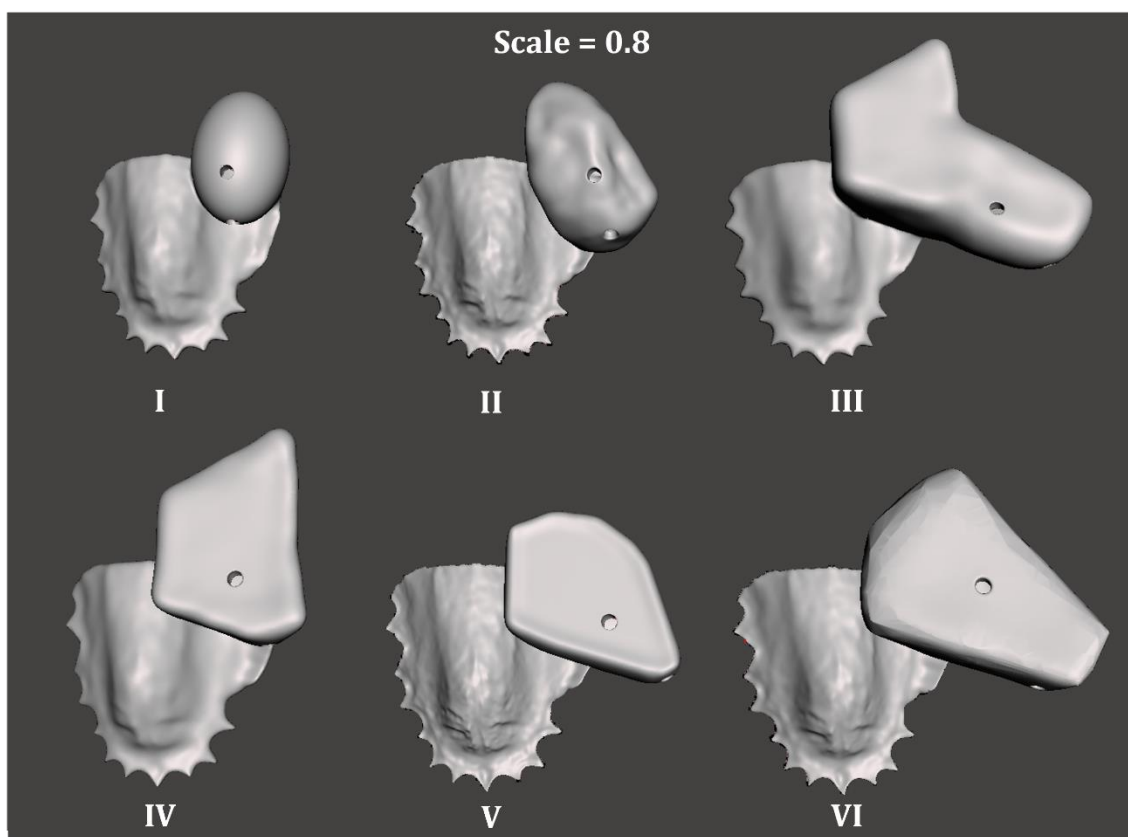


Figure D.3. Different types of digital immediate surgical obturator designs in Autodesk Meshmixer. I: Hollow bulb. II: Intraoral scanned obturator. III: Two separated bone- and soft tissue closed surface model (CSM). IV: Bone CSM. V: Manual shaped CSM. VI: Bone- and soft tissue CSM.

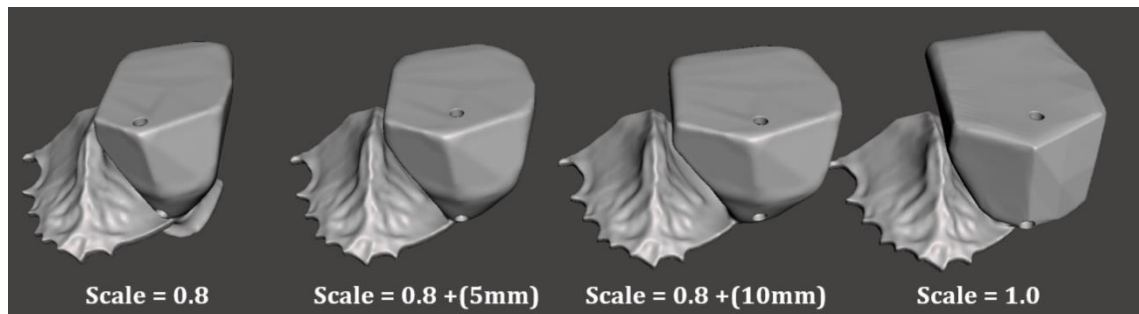


Figure D.5. Closed surface model (CSM) obturator designs scaled to 0.8 (1-3) and 1.0 (4) in Autodesk Meshmixer. The first obturator contains an additional zygoma-wiring boulder. The lateral width of the second and third obturator is extended with 5 and 10 mm respectively. The fourth obturator is extended with 5 and 10 mm respectively.

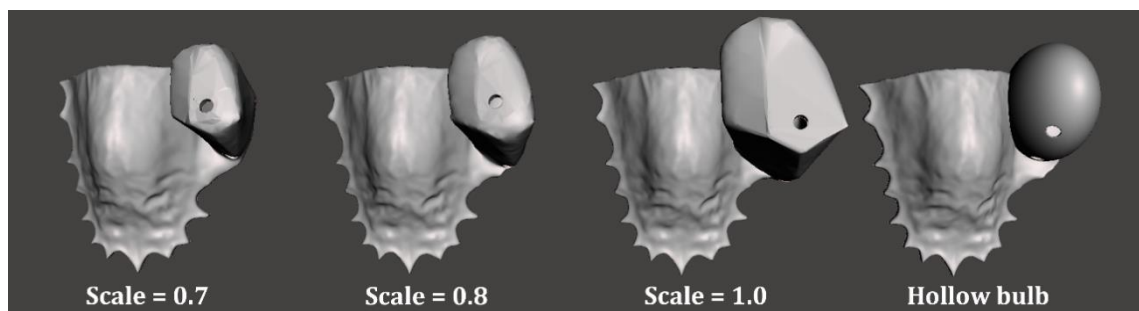


Figure D.4. Different scaled closed surface model (CSM) obturator designs (1-3), and the hollow bulb design (4) in Autodesk Meshmixer.

E: Conventional surgical obturators, classified by the Ooms' classification system.

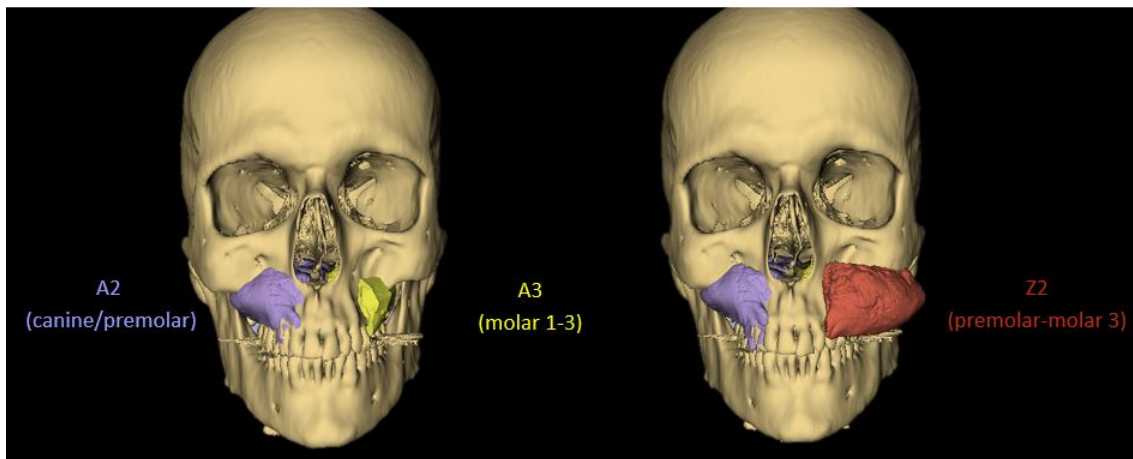


Figure E.1. Examples of intraoral scanned immediate surgical obturators, classified according to the Ooms' ISO classification system.

F: Closed surface model obturators based on the Ooms' obturator classification system

Table F.1. Closed surface model designed immediate surgical obturators (ISO's) for class A1 – A4 of the Ooms' ISO classification system in 3D Slicer.

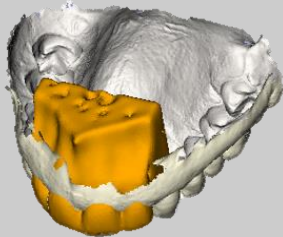
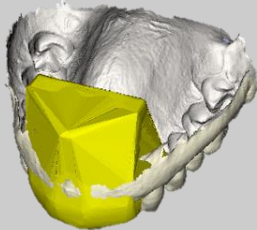
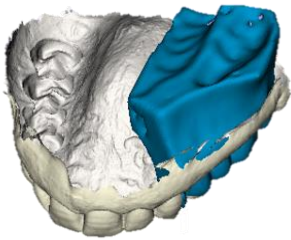
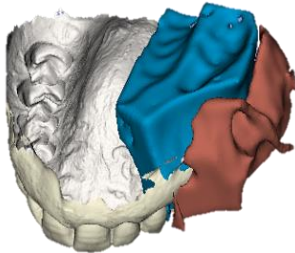
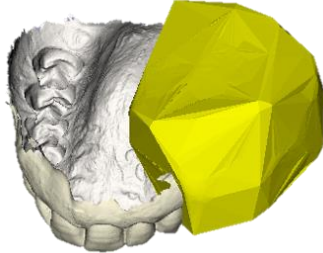
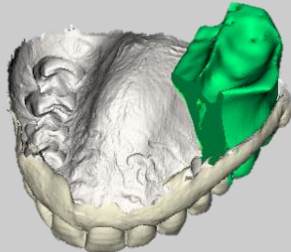
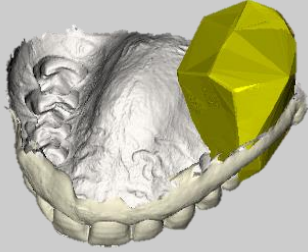
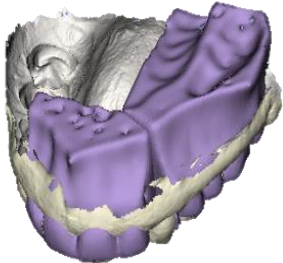
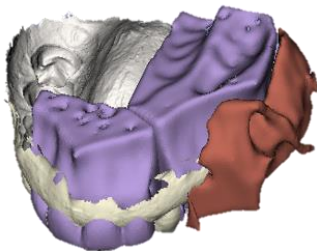
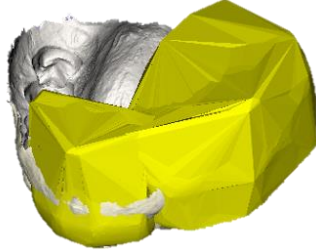
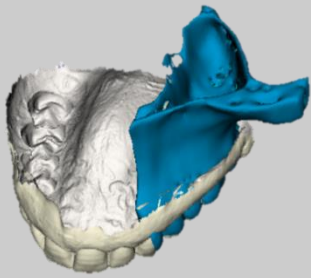
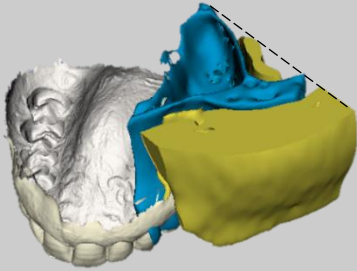
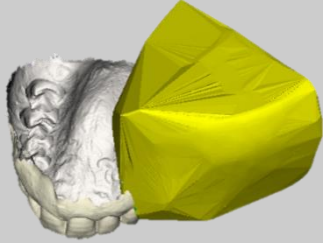
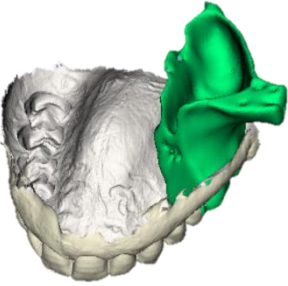
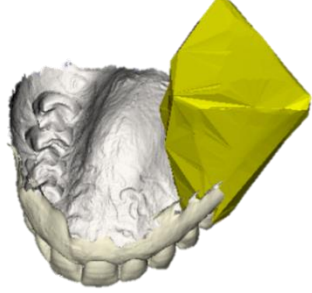
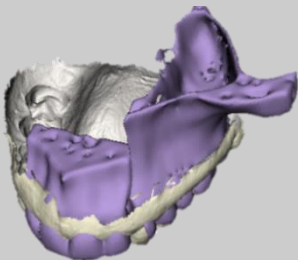
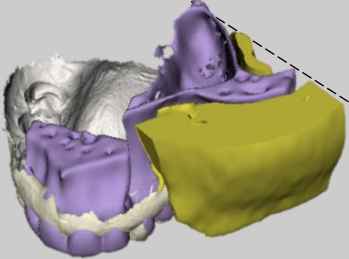
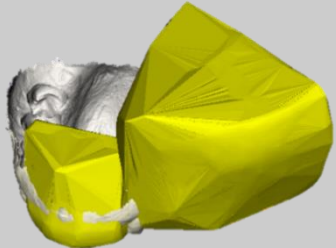
Class	Resection bone	Resection bone + soft tissue	Closed surface model
A1			
A2			
A3			
A4			

Table F.2. Closed surface model designed immediate surgical obturators (ISO's) for class Z2 – Z4 of the Ooms' ISO classification system in 3D Slicer.

Class	Resection bone	Resection bone + Soft tissue	Closed surface model
Z2			
Z3			
Z4			

G: Direct comparison results of the weight reduction, volumes, and Hausdorff Distances

Table G.1. Direct comparison of the weight-reduction values for n=17.

Patient No.	Class	Theoretical Maximal Reference		Theoretical Clinical Reference		CAD/CAM (Bone-CSM 0.8)	
		Weight reduction (g)	Weight reduction (%)	Weight reduction (g)	Weight reduction (%)	Weight reduction (g)	Weight reduction (%)
1	Z3	41.73	69.66	27.99	46.72	26.80	44.73
2	Z4	87.35	75.27	58.21	50.16	52.12	44.92
3	A3	40.20	68.80	27.19	46.54	27.41	46.91
4	Z2	55.93	55.47	37.36	37.06	40.67	40.34
5	Z4	28.84	68.82	19.43	46.35	21.32	-50.86
6	Z4	58.82	56.69	39.65	38.22	59.90	57.74
7	A3	29.53	70.82	19.88	47.66	18.23	43.71
8	Z2	44.32	69.12	29.86	46.57	29.71	46.33
9	Z2	29.72	59.13	19.38	38.56	26.77	53.25
10	Z4	34.42	74.62	23.04	49.94	20.84	45.17
11	A4	41.10	73.16	27.28	48.56	24.23	43.14
12	Z4	52.96	69.66	35.80	47.09	38.89	51.16
13	Z4	80.27	72.71	52.76	47.80	56.83	51.48
14	Z4	69.49	75.97	46.43	50.76	54.77	59.88
15	A4	93.85	72.48	62.90	48.58	59.38	45.86
16	Z4	207.16	82.34	137.43	54.63	99.20	39.43
17	A2	31.71	69.70	21.31	46.83	15.71	34.53

HD: Hausdorff Distance; CSM = Closed Surface Model.

Table G.2. Direct comparison of the volumes and Hausdorff Distances for the bone-CSM designs, for n=17.

Patient No.	Class	Obturator volumes (cm ³)		Conventional vs. CSM 0.8 (mm)		
		Conventional	Bone CSM	HD Maximum	HD Average	HD 95th percentile
1	Z3	41.89	16.09	3.15	0.07	0.68
2	Z4	81.15	29.70	3.37	0.02	0.00
3	A3	40.86	17.59	6.20	0.43	3.00
4	Z2	70.5	18.78	0.00	0.00	0.00
5	Z4	29.31	18.78	8.01	0.71	3.62
6	Z4	72.55	45.18	14.79	1.77	8.25
7	A3	29.16	11.66	4.88	0.41	2.79
8	Z2	44.84	18.59	10.37	0.34	2.88
9	Z2	35.15	20.34	5.42	0.25	1.86
10	Z4	32.26	14.45	6.07	0.47	3.65
11	A4	39.28	14.86	10.77	0.23	1.77
12	Z4	53.16	27.23	16.16	1.31	8.74
13	Z4	77.2	37.78	13.03	0.93	5.30
14	Z4	63.96	42.92	9.25	1.09	5.61
15	A4	90.54	37.48	7.13	0.35	2.66
16	Z4	175.93	43.18	10.35	0.64	5.05
17	A2	31.81	5.54	6.58	0.68	4.16

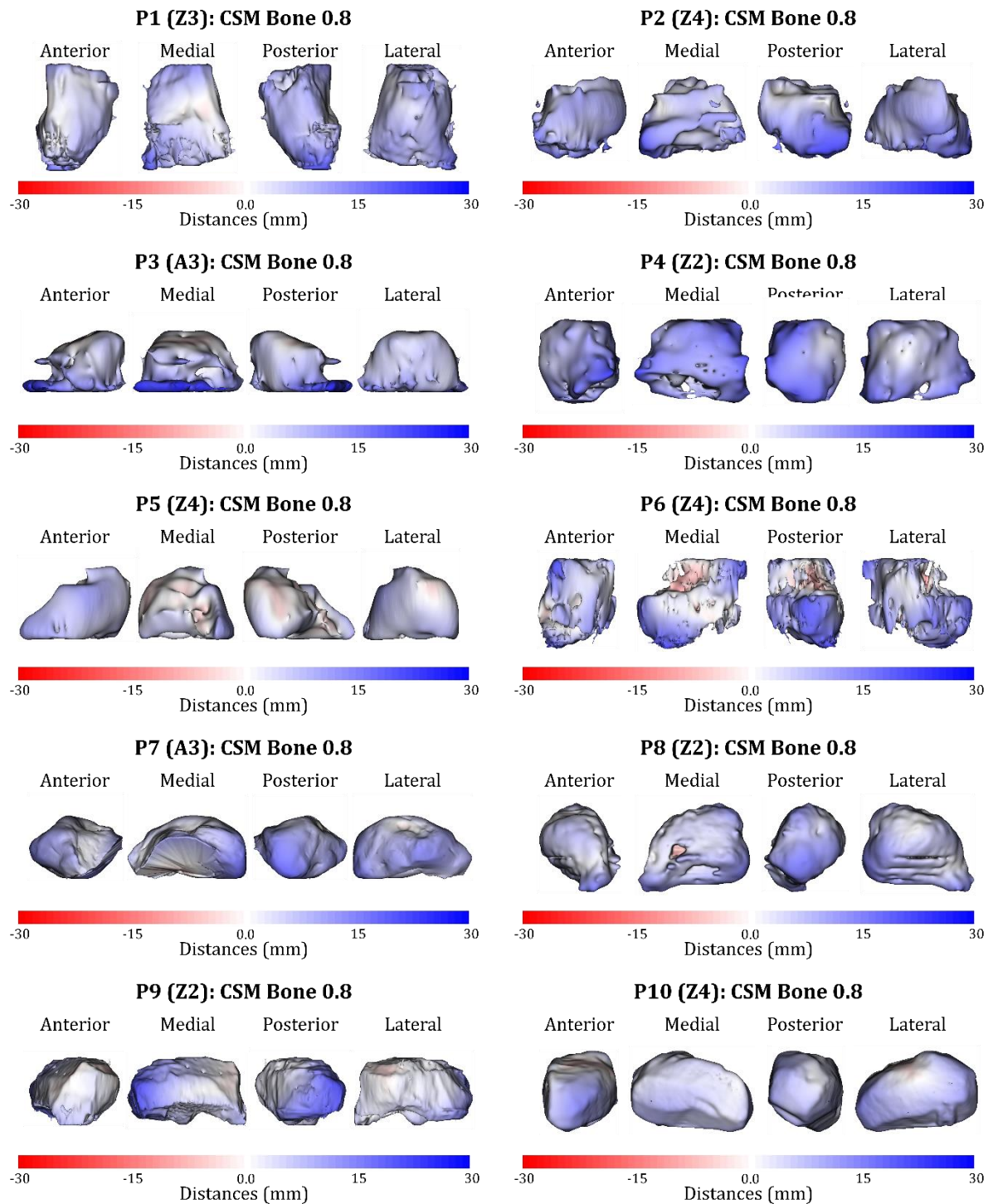
HD: Hausdorff Distance; CSM = Closed Surface Model.

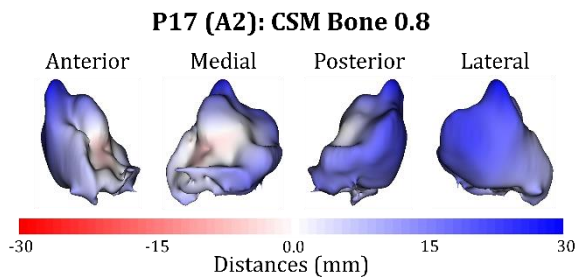
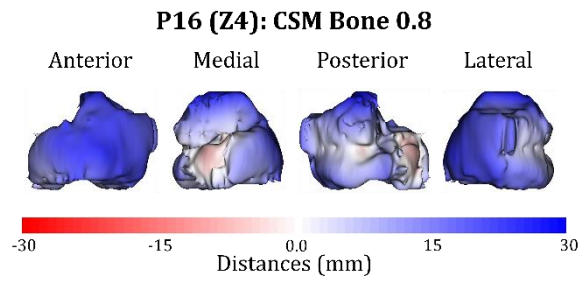
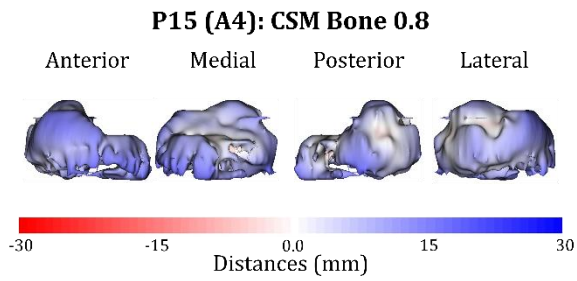
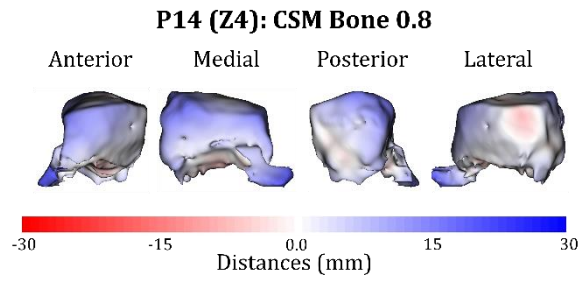
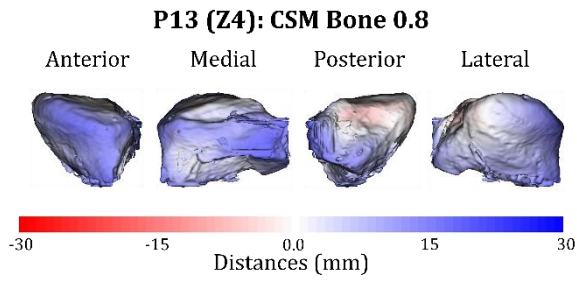
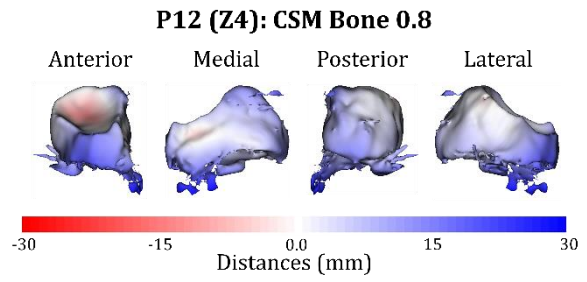
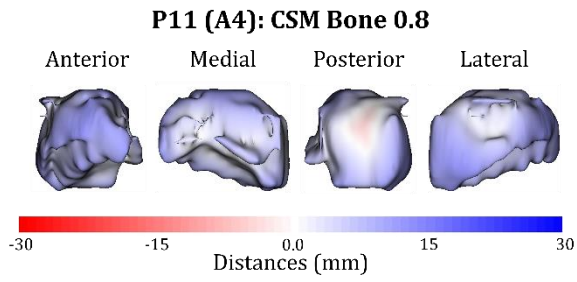
Table G.3. Direct comparison of the volumes and Hausdorff Distances for the bone and soft-tissue CSM designs, for n=11.

Patient No.	Class	Obturator volumes (cm ³)		Conventional vs. CSM 0.8 (mm)		
		Conventional	Bone & soft tissue CSM	HD Maximum	HD Average	HD 95th percentile
2	Z4	81.15	53.45	15.88	1.59	9.92
4	Z2	70.5	44.27	15.57	2.03	7.63
5	Z4	29.31	31.40	14.22	1.84	8.10
6	Z4	72.55	61.04	16.65	2.43	8.74
8	Z2	44.84	28.94	12.88	1.54	6.88
10	Z4	32.26	22.03	14.28	1.29	7.04
12	Z4	53.16	36.24	16.16	1.89	9.83
13	Z4	77.2	42.06	12.00	0.88	5.12
14	Z4	63.96	59.88	17.45	2.84	9.98
15	A4	90.54	65.45	6.80	0.36	2.79
16	Z4	175.93	70.22	10.33	0.60	5.01

HD: Hausdorff Distance; CSM = Closed Surface Model.

H1: Distance maps Bone-CSM designs





H2: Distance maps bone & soft tissue CSM

